ELECTROKINETICALLY ENHANCED SAMPLING AND DETECTION OF BIOPARTICLES WITH SURFACE BASED BIOSENSORS

by

Matthew Robert Tomkins

A thesis submitted to the Graduate Program in the Department of Chemical Engineering

in conformity with the requirements for the

Degree of Doctor of Philosophy

Queen's University

Kingston, Ontario, Canada

January, 2012

Abstract

Established techniques for the detection of pathogens, such as bacteria and viruses, require long timeframes for culturing. State of the art biosensors rely on the diffusion of the target analyte to the sensor surface. AC electric fields can be exploited to enhance the sampling of pathogens and concentrate them at specific locations on the sensor surface, thus overcoming these bottlenecks. AC electrokinetic effects like the dielectrophoretic force and electrothermal flows apply forces on the particle and the bulk fluid, respectively. While dielectrophoresis forces pathogens towards a target location, electrothermal flows circulates the fluid, thus replenishing the local concentration. Numerical simulations and experimental proof of principle demonstrate how AC electrokinetics can be used to collect model bioparticles on an antibody functionalized selective surface from a heterogeneous solution having physiologically relevant conductivity. The presence of parallel channels in a quadrupolar microelectrode design is identified as detrimental during the negative dielectrophoretic collection of bioparticles at the centre of the design while simultaneously providing secondary concentration points. These microelectrodes were incorporated onto the surface of a novel cantilever design for the rapid positive dielectrophoretic collection of *Escherichia coli* bacteria and enabled the subsequent detection of the bacteria by measuring the shift in the resonance frequency of the cantilever. Finally, a proof of principle setup for a Raman coupled, AC electrokinetically enhanced sampling and detection of viruses is shown where the presence of M13 phages are identified on a selective antibody functionalized surface using Raman spectroscopy.

Dedication

I would like to dedicate this to my close friends and family, without whom, the ability for me to accomplish my dreams, would have been less than idle fantasy.

Lina, the love of my life,

Jeanne and David, Andrew, Suzhen, Grace and Bernard, Paula, and Rinee

Our beings are shaped not only by who we are, but who we are surrounded by.

Thank you

Acknowledgements

The work in this thesis was not accomplished in a vacuum and the contributions of a multitude of individuals must be acknowledged. The research inspiration and guidance for this work originated from my supervisor, Prof. Aristides Docoslis. Individuals from my research group who have been involved with different aspects of this project include Jeff Wood (COMSOL), Jie Ning, Mark Hoidas, Ian Swyer, Dr. Protiva Rani Roy and Eric Potter. Collaborative works involving the cantilever beam research could not have been done without the support of both Prof. Yongjun Lai, for providing the cantilever beams and lessons about MEMS, and his graduate student, Jacky Chow. Biological materials, training and expertise without which this work would not have proceeded as quickly as it has are thanks to Dorothy Agnew. Further biological materials as well as training and access to equipment include Prof. Andrew Daugulis and his graduate student Julian Dafoe. Photolithography training and equipment which enabled part of this work are due in part to Prof. Michael Watt, Prof. Rob Knobel, Prof. Rob Lockwood, Jennifer Campbell and Eric Simpson. Technical staff are part of every project and know all ins and outs when help is really needed and include Steven Hodgson, Kelly Sedore and Charlie Cooney (SEM). Similarly the administrative staff keep the wheels greased like Maureen Plunkett, Laurie Phillips, Lynn O'Malley and Barb Lawson. Valuable advice which is freely given must also be acknowledged to Dr. Shelagh Mirski (biohazard safety), Dr. Juliana Ramsey (biological growth and samples), Prof. Leeda Raptis (virus and antibody information), Prof. Martin Guay (experiment planning) and my comprehensive committee, Prof. Kunal Karan and Prof. Tim McKenna. Finally, the generous funding, without which none of this would be possible was provided by NSERC and Queen's University.

Table of Contents

Nomenclature

A	particle cross section	m^2
C_t	interelectrode capacitance	C/V
C_p	heat capacity of the medium	J/mol ŀK
C_v	lift coefficient	-
D	diffusion coefficient	m^2/s
$\vec{E}$	electric field intensity	V/m
$\vec{F}_{DEP}$	dielectrophoretic force	N
F_S	Saffman list force	N
F_M	Magnus list force	N
f	frequency	Hz
f	friction factor	kg/s
f_c	resonance frequency	Hz
$\vec{f}_{elec}$	electric field force on medium	N
G_t	interelectrode conductance	S
I	identity matrix	1
k	thermal conductivity	W/m ŀK
k_B	Boltzmann's constant	J/K
k_S	spring constant	N/m
$\tilde{K}_e$	Clausius-Mossotti factor	-
l, l_0	characteristic length	m
m	mass	kg
p	pressure	Pa
Pe	Peclet number	-
Pr	Prandtl number	-
r, r_p	radius of particle	m
R[]	Real portion of number in the square brackets	-
Re	Reynolds number	-
t	time	s
T	temperature	K
u	fluid velocity	m/s
V, V_0	electrical potential / applied voltage	V
V_R	Relative velocity	m/s

Greek Symbols

α	gradient of permittivity as a function of temperature	F/m K
β	gradient of conductivity as a function of temperature	S/m K
$\dot{\gamma}$	shear rate	s^{-1}
ε	permittivity	F/m
η	fluid viscosity	Pa s
κ	reciprocal Debye length	m^{-1}
ν	kinematic viscosity	m^2/s
ρ	density	kg/m^3
ρ_e	charge density	C/m^3
σ	electrical conductivity	S/m
σ_{q0}	surface charge density	C/m^2
τ_{CR}	charge relaxation time	s
ω	angular frequency	rad/s

Subscripts

i	phase in system; used for series of equations
M	medium
P	particle
PP	peak-to-peak
RMS	root mean square
t	tangential direction
x	x-axis

Acronyms

cfu	colony forming units
DEP	dielectrophoresis
pfu	plaque forming units

List of Figures

List of Tables

Chapter 1 Introduction

The detection of pathogenic particles on the micron and sub-micrometer scale, such as bacteria and viruses, often require extended periods of time for sample culturing until detectable concentration levels of the pathogen are reached, a process that can take up to several days. There remains a need for the rapid detection of pathogens, for example, the quick identification of a disease prior to an outbreak, or the need to monitor bacteria levels in the local water supply. Portable microfluidic biosensors would enable detection in a variety of settings with the capability to differentiate between bacterial or viral strains. However, most sensors require that the pathogen diffuse to the location where sensing occurs and must then be detected via signal transduction or via the labeling of the compound or through enzymatic identification. This diffusion limitation remains a major bottleneck in the operation of these devices, especially for the detection of pathogens from dilute samples.

One promising approach to achieve rapid sampling is through the use of microelectrodes integrated on a biosensor's surface in order to exploit alternating current (AC) electrokinetic effects. Through the generation of spatially non-uniform electric field effects diffusion limitations can be overcome. AC electrokinetic forces which generate electrothermal flows and dielectrophoretic forces can, respectively, provide the means for fast convective transport to, and concentration amplification of a pathogen at a target detection surface.

The research presented will explore how the use of AC electrokinetics influences micron and sub-micron sized pathogenic particle sampling. The results of that research will then be used to explore how AC electrokinetics can be integrated into a surface based biosensor. Firstly, a literature review is provided to establish the context of the state of the art. Secondly, promising

quadrupolar microelectrode designs are analyzed with respect to their ability to enhance sampling at target locations. The microelectrode designs are then integrated with a cantilever for the detection of bacteria. Finally, these surface based microelectrodes are coupled with a Raman spectroscope in order to explore one avenue that can lead to the label free detection of viruses.

1.1 Motivation

In 2007, Docoslis *et al.*, demonstrated how quadrupolar microelectrodes could be used to capture the *vesicular stomatitis* virus particles from a sample onto a surface in a range of medium conductivities. At the time, research was limited to capture using non-specific surfaces and sampling from homogeneous populations without a coupled or inherent detection method. However, the quadrupolar design employed was identified as one that held potential for application with other biosensor designs (Docoslis *et al.*, 2007).

The designs employed in the previous work were not optimized for collection and the synergism between the electrothermal flows and dielectrophoresis that caused rapid particle transport and trapping on the surface of planar quadrupolar microelectrodes, respectively, were not well understood (Docoslis *et al.*, 2007). Features, like the presence of electrode channels were incorporated; however, their impact on sampling was unknown. Numerical simulations were created to examine the relationship between these microelectrode designs and the AC electrokinetic collection and flow patterns along with experimental evidence to validate the models. Furthermore, the microelectrodes used in the previous work employed a non-specific layer and examined collection from homogeneous populations (Docoslis *et al.*, 2007). In order to address the issue of selectivity, the quadrupolar microelectrode biosensors were used in proof of principle experiments with functionalized surfaces.

Target applications for the quadrupolar microelectrode designs were identified, for example, the AC electrokinetic sampling of viruses in high conductivity biological samples, like saliva, or sampling bacteria from heterogeneous populations in low conductivity environments, like lake water. Yet, for samples with low conductivity, positive dielectrophoresis would occur and the need remains for an integrated or at least coupled detection methodology. A collaborative work was setup with Dr. Yongjun Lai from the Mechanical and Materials Engineering department at Queen's University whose expertise included micro-electromechanical systems, such as cantilevers. From this collaboration, a cantilever / quadrupolar microelectrode biosensor prototype was made to test the concept of on-chip sampling and detection. However, the presence of a cantilever would influence the nature and direction of the fluid flows and forces on the suspended particles. In particular, the development of this prototype is concerned with how the placement of the electrodes in relation to the cantilever will affect collection and sampling. Numerical simulations were used to address these questions while proof of principle experiments demonstrated how the cantilever based detection of *Escherichia coli* could be enhanced with AC electrokinetics.

The motivation for this work seeks to use AC electrokinetics to accelerate the sampling of pathogens, like viruses, onto a specific surface. A further motivation is to demonstrate how AC electrokinetics can be integrated with a detection method. Raman spectroscopy was also identified as a desired detection method since it would potentially allow for the "fingerprinting" of molecules for pathogen detection and identification. While Raman has been used to identify viruses, studies have been limited to samples with high concentrations. An AC electrokinetically enhanced biosensor couple with Raman spectroscopy would potentially allow for the one step concentration and identification of viruses from dilute samples.

1.2 Publications

The work in this thesis has generated the following list of publications.

M. Tomkins, J. Chow, Y.J. Lai, and A. Docoslis. Coupled cantilever-microelectrode biosensor for enhanced pathogen detection, *Sensors and Actuators*, (Accepted pending minor revision Sept 2011)

R. Roy, M. Tomkins, and A, Docoslis. "Enhancing the Performance of Surface-based Biosensors by AC Electrokinetic Effects - a Review". *Biosensors - Emerging Materials and Applications*. Ed: Pier Andrea Serra. Intech (July, 2011)

MR Tomkins, JA Wood, A Docoslis. Observations and analysis of electrokinetically driven particle trapping in planar microelectrode arrays. *Canadian Journal of Chemical Engineering*, (4) 609-621, (2008)

J.A. Wood, B. Zhang, M.R. Tomkins and A. Docoslis. Numerical Investigation of AC electrokinetic virus trapping inside high ionic strength media. *Microfuidics and Nanofluidics.* 3(5) 547-560, (2007)

A. Docoslis, B. Zhang, J.A. Wood, and M.R. Tomkins. Numerical Simulations of Electrokinetically-Driven Capture of Viral Particles inside Media of High Ionic Strength. *2006 AIChE Annual Meeting*, San Francisco, California, USA (2006)

1.3 Presentations

The work in this thesis has generated the following list of presentations.

M.R. Tomkins, and A. Docoslis. Detection of Micron and Submicron Sized Pathogens in Water by Combining Electrokinetic Sampling and Raman Spectroscopy. *61st Canadian Chemical Engineering Conf.*, Ottawa, ON (2011)

M.R. Tomkins, and A. Docoslis. Improving sampling for biosensors by using electric fields. *11th Annual CSChE Biotech Meeting*, Waterloo, ON. Awarded 3rd Place (2009)

M.R. Tomkins, and A. Docoslis. Electric Field Enhanced Sampling from Heterogeneous Suspensions of Bioparticles in Fluids. *58th Canadian Chemical Engineering Conf.*, Ottawa, ON (2008)

Chapter 2 Literature Review

Miniaturized surface based biosensors are a cost effective and portable means for the sensing of biologically active compounds. With advents in micro- and nanotechnology, the design of surface based biosensors can be adapted for various detection goals and for integration with multiple detection techniques. In particular, the issue of pathogen detection is an important challenge with applications in defence, health care, food safety, diagnostics and clinical research (Velusamy *et al.*, 2010). The research of micro-fluidic analytical systems, such as surface based biosensors or "lab-on-a-chip" designs, have gained increasing popularity, not only due to the enhancement of the analytical performance at small scales, but also due to their reduced size, decreased consumption of reagents, the ability to integrate multiple technologies within a single device and potential for remote sensing (Pejcic *et al.*, 2006; Popovtzer *et al.*, 2006; Weigl *et al.*, 2003). Although conventional pathogen detection methods are well established, they are greatly restricted by the assay time. For pathogens that typically occur at low concentrations, the mass transfer required for detection is diffusion limited and incubation is often needed in order to enhance the concentration of the target analyte (Yang and Bashir, 2008). AC electrokinetic effects provide a means for biosensors to detect pathogens quickly and at lower concentrations, thus potentially overcoming these bottlenecks.

2.1 AC Electrokinetics

AC electrokinetics deals with the effects of an electric field on the electrical double layer. These forces can influence the movement of particles and/or the fluid and has received considerable attention for improving the capture of analytes. An example of an AC electrokinetic

force is particle dielectrophoresis (DEP) where a non-uniform electric field acts on a polarizable particle. When acting on a fluid, an AC electric field can cause deterministic motion by producing an AC electrokinetic force, AC electroosmosis, at low frequencies and an electrohydrodynamic force, electrothermal flow, at high frequencies. These forces can create non-uniform streamlines to convex and mix (Li, 2004), or even to separate a mixture of particle sizes (Green and Morgan, 1998). Most bioparticles, such as cells and viruses, behave as dielectrically polarized particles in the presence of an external electric field. Using AC electric fields for particle manipulation offers several advantages, such as allowing operation at low voltages, which is important for portable devices and minimizing electrolysis and chemical reactions. The following will provide a brief overview of AC electrokinetic forces with applications for use in biosensors.

2.1.1 Dielectrophoresis

DEP is a force acting on the induced dipole of a polarizable particle in a suspending fluid due to the presence of a non-uniform electric field (Pohl, 1951). It was first used to remove suspended particles from a polymer solution and named by Pohl. In brief, if a particle, such as a bacterium or virus, is more polarizable than the surrounding medium, the particle undergoes positive DEP (pDEP) and tends towards areas of high electric field gradients (Figure 1 - Left). If a particle is less polarizable than the surrounding medium, it undergoes negative DEP (nDEP) and tends towards areas of electric field gradient minima (Figure 1 - Right).

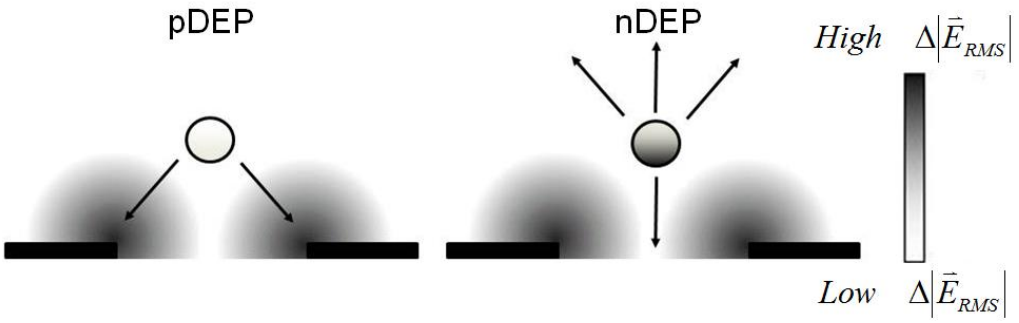

Figure 1: A schematic representation of a particle undergoing pDEP (left) and nDEP (right) in a non-uniform electric field. Horizontal black bars indicate the electrodes.

The time averaged dielectrophoretic force for a spherical particle in an electric field with a constant phase is presented in equation 1 (Morgan and Green, 2003).

$$< \vec{F}_{DEP} >= 2\pi\varepsilon_M r_p^3 R\left[\tilde{K}_e^*\right]\nabla\left|\vec{E}\right|^2 \quad (1)$$

$$R\left[\tilde{K}_e^*\right] = \frac{\varepsilon_P^* - \varepsilon_M^*}{\varepsilon_P^* + 2\varepsilon_M^*} \quad (2)$$

The equation shows that the DEP force (F_{DEP}) is a function of a particle's size (r_P), and the real part of the Clausius-Mossotti factor (equation 2) which is a function of the medium's complex permittivities (ε^*_P and ε^*_M) as well as the gradient of the applied electric field ($(\nabla|\vec{E}|^2$).

Since the force of DEP varies with particle size and the electric field gradient, it allows for separation between different sized cells. Alternatively, by measuring the velocities of single cells as a function of distance and voltage, DEP can be used to characterize their electrical properties (Pohl and Pethig, 1977; Burt *et al.*, 1990; Humberto *et al.*, 2008). Furthermore, DEP can be integrated within a biosensor by using an array of electrodes in order to amplify a pathogen's concentration at a sensor surface. The use of DEP causes the deterministic motion of particles; yet, it is a short range force. The same electric field for applied DEP can have an effect

on the medium as well through electrothermal or electroosmotic effects. An applied electric field would thereby overcome the limitations due to diffusion by having both a short range force near the electrodes and a mid range force by causing desirable fluid flows from the bulk to the local area of the sensor (Sigurdson *et al.*, 2005).

2.1.2 AC Electroosmosis

AC electroosmotic flow is typically produced from the interaction of the nonuniform electric field and the diffuse electrical double layer formed by the polarization of the electrode by the counter ions in an electrolyte solution (Figure 2).

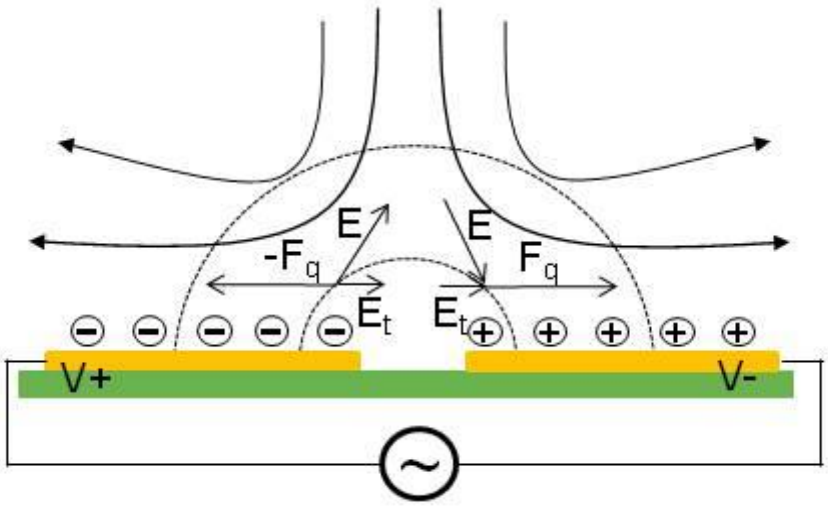

Figure 2: The reported mechanism for AC-electroosmosis where the arrows indicate fluid flow driven down towards the electrode gap and out along the surface of the electrode (horizontal gold bars) due to the force of the tangential component of the electric field on the ions in solution. Adapted from Morgan and Green (2003).

The tangential component of the electric field (E_t) at the electrode surface applies a force (F) on the ions present, pushing them out across the surface of the electrode and thus dragging

fluid down into the center of the gap. The time averaged fluid velocity due to AC electroosmosis is presented in equation 3 (Castellanos *et al.*, 2003).

$$< u >= \frac{1}{2} R\left[\frac{\sigma_{qo} E_t^*}{\eta \kappa} \right] \tag{3}$$

AC electroosmosis is a function of the surface charge density (σ_{qo}), fluid viscosity (η), the Debye length (κ^{-1}) and the tangential component of the electric field (E_t). The circuit formed across the medium can be represented in a simplified manner. The electrical double layer at each of the electrodes is represented by a capacitor while the medium acts as a resistor. Therefore, the circuit can be described as a capacitor in series with a resistor follow by another capacitor.

AC electroosmosis dominates at frequencies between 100 and 100,000 Hz while above 100,000 Hz, AC electrothermal flow is predominant (Morgan and Green, 2003). At low frequencies, due to the presence of counter-ions near the electrode surface, the majority of the potential drops across the double layer near the electrodes. Therefore, the remaining voltage drop across the medium is small in comparison. The capacitance of the double layer is inversely proportional to frequency and at high frequencies the capacitance becomes negligible resulting in a small voltage drop across the double layer. For an irrotational electric field, the tangential component must be constant between the two electrodes. If the potential drop across either the medium or the electrical double layer is negligible, the tangential component of the electric field will be weak. Therefore, the resulting velocity due to AC electroosmosis is negligible.

2.1.3 Electrothermal Flows

AC electroosmosis and electrothermal effects produce similar flow patterns in some cases, but they are of different origin. Electrothermal flow arises by uneven Joule heating of the

fluid, which gives rise to nonuniformities in conductivity and permittivity. These non-uniformities are affected by the electric field which in turn generates flow, often in circulating patterns (Feng *et al.*, 2007). The time averaged body force on the medium responsible for the generation of Electrothermal fluid flow for a constant phase electric field is presented in equation 4 (Castellanos *et al.*, 2003).

$$< \vec{f}_e >= \frac{1}{2}\frac{\varepsilon_m(\alpha-\beta)}{\sigma_m^2+(\omega\tau_{CR})^2}(\nabla T\cdot\vec{E})\vec{E}-\frac{1}{4}\varepsilon_m\alpha\left|\vec{E}\right|^2\nabla T \qquad (4)$$

Electrothermal fluid flow is a function of: α and β the effects of temperature on the gradients of permittivity and conductivity respectively; and τ_{CR}, the charge relaxation time of the medium defined as the ratio of a medium's permittivity (ε_m) to its conductivity (σ_m). The first term on the right hand side of equation 4 is the Coulombic contribution while the second term is the dielectric contribution to the total force. The Columbic term dominates at low frequencies while the dielectric term dominates at higher frequencies and the cross over frequency is the same order as σ/ ε, the inverse of the charge relaxation time (Ramos *et al.*, 1998).

2.2 Manipulation of Bioparticles by AC Electrokinetics

The concentration of bioparticles in a target sample can range from less than 10 particles per 100 mL to more than 10^8 particles per mL (Velusamy *et al.*, 2010). Due to the range of effective frequencies, voltages and ease of application, a number of researchers have proposed techniques to enhance the activity of microfluidic sensors by using electrohydrodynamic flows (Sigurdson *et al.*, 2005; Hoettges *et al.*, 2003; Gagnon and Chang, 2005; Wu *et al.*, 2005a; Sauli *et al.*, 2005; Hou *et al.*, 2007; Wu *et al.*, 2005b; Miller *et al.*, 2011). Before surface based biosensors can identify a target bioparticle, that bioparticle must first move from the bulk sample

towards the sensing element and then become captured or detected. The four most prevalent designs for surface based biosensors are presented in Figure 3 and include pair electrodes, polynomial electrodes, castellated electrodes and interdigitated electrodes. Pair electrode designs include setups of two electrode tips arranged opposite to each other to induce positive DEP or for the sorting of various sized particles or agglomerates (Suehiro *et al.*, 2003a; 2003b). Alternatively, the pair of electrodes can be widened to form parallel plates which provide a uniform electrode field along the parallel section and can be used to investigate particle velocity and electrothermal flows (Green *et al.*, 2000). Polynomial electrodes are composed of an even number of four or more equally spaced electrodes centered around a point. This arrangement creates an electric field null at the centre of the design and allows for negative DEP to occur (Huang and Pethig, 1991). Castellated electrodes are a series of slots and gaps that incorporates both electric field maxima and minima in its design and allows for the quick sorting or separation of particles. Furthermore, with the fine tuning of the electric field, the AC electrokinetic flows can also be used to accumulate particles in a variety of locations (Green *et al.*, 2000a). Interdigitated electrodes have comb like finger electrodes that extend into the adjacent electrode creating a series of parallel electrodes. This design maximizes surface area for taking advantage of particles being directed towards the electrode edges via positive DEP and because of the presence of adjacent, oppositely charged electrodes, strings of particles can align and connect across the gap. (Holzel and Bier, 2003).

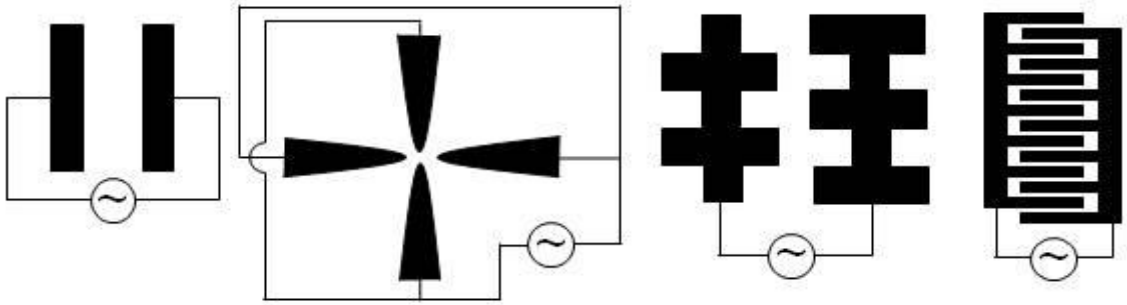

Figure 3: Examples of electrode designs with power source from left to right: parallel plate, polynomial, castellated, interdigitated.

Since the capture of particles via negative dielectrophoresis occurs at field nulls, three dimensional electrode structures can be created which allow for particle levitation and capture in space rather than on a surface. Some designs have created field nulls in space employing as few as two electrodes where one is a point and the other is a ring electrode (Li *et al.*, 2008). A typical design would use octapole electrodes which generally consist of two sets of quadrupolar electrodes where one is suspended above the other (Chen *et al.*, 2006). The field null would be generated halfway between the two gaps quadrupolar design. Three dimension designs, such as extruded or pillar electrodes have also been shown to be able to capture particles and hold them against external flows (Voldman *et al.*, 2002). One particular advantage of these designs is that the field null occurs far from the electrodes and the volume of the 'dielectrophoretic trap' can be manipulated by varying the field strength (Li *et al.*, 2008). However, their fabrication is complicated as it requires careful alignment and assembly of the substrates.

As demonstrated in section 2.1.3, AC electrokinetic effects can be used to affect the movement of bioparticles from the bulk. Through AC electroosmosis or Electrothermal flows bioparticles are continuously brought towards the sensing element overcoming any diffusion limitations. With DEP, the bioparticles are retained in proximity to the sensing element allowing

for more time for capturing or detection to take place. Without these driving forces, biosensors can suffer from poor detection limits because of the low number distribution of molecules in the detection region and limited physical sensitivity of the transducer. The literature presented will demonstrate how AC electrokinetics has been employed to manipulate cells, viruses and DNA for the performance enhancement of surface based biosensors.

2.2.1 Cells

Cells, such as bacteria and yeast, represent the largest sized bioparticles in the category of pathogens and are generally the most easily influenced by AC electrokinetic effects. One of the first reports dealing with the manipulation of cells was presented by Dimitrov and Zhelev (1987) where the manipulation, dielectrophoretic mobility, and permittivity of individual cells were examined under different conditions. The capability to move cells based on their dielectric properties allowed for DEP to be useful in the separation of mammalian cells (Gascoyne *et al.*, 1992), capture of living mammalian cells (Gray *et al.*, 2004), separation of viable and nonviable cells (Markx *et al.*, 1994; Oblak *et al.*, 2007; Li and Bashir, 2002; Talary *et al.*, 1996; Jen and Chen, 2009), microorganisms (Markx *et al.*, 1995) and human breast cancer cells from blood cells (Becker *et al.*, 1995). This cell sorting allows for the screening of cells prior to exposure to a biosensor's surface thus providing a means of rapid sample sorting.

Depending on the sensing location and the dielectric properties of the pathogen of interest, the electrode design can be an important consideration. Interdigitated castellated microelectrodes have been widely used for cell manipulation and separation (Betts, 1995; Oblak *et al.*, 20007; Pethig *et al.*, 1992; Pethig, 1996) as this design allows for the differential focusing and collection of cells at distinct electrodes areas under the influence of both positive and negative dielectrophoretic forces (Gascoyne *et al.*, 1992). In 1991 the first polynomial electrode

design was reported to produce a well defined non-uniform electric field for the study and application of nDEP (Huang and Pethig, 1991). An example of this is presented in Figure 4 where *E. coli* and *M. Lysodeikticus* are separated using a polynomial electrode setup. Recently, a simple and novel curved electrode design has been used for the separation of airborne microbes from beads or dust that are present in airborne environmental samples, an important task prior to the real-time detection of airborne microbes (Sungmoon *et al.*, 2009).

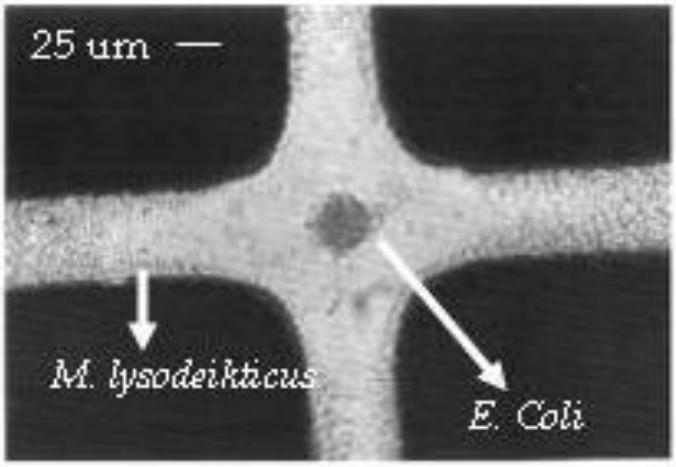

Figure 4: Separation of *E. coli* (experiencing nDEP) and *M. lysodeikticus* (experiencing pDEP) in a polynomial electrode after application of a 4 $V_{PP,}$ 100 kHz signal in a suspending medium of 280 mM mannitol with a conductivity of 550 μS cm^{-1} (Markx *et al.*, 1994).

In order for quantitative and qualitative studies to take place on a single cell or a small population of cells, the isolation and accurate positioning of the target must first be accomplished. Negative dielectrophoresis in particular has emerged as a powerful tool for this role. Under the influence of nDEP bioparticles are typically driven to regions away from the electrodes. The *E. coli* in Figure 4 are collected in a nDEP "trap" or "cage" at the center because the electric field at

that point is a local minimum. This concept can be expanded to arrays of microelectrodes, thus enabling the precise placement and retention of multiple pathogenic samples (Frenea *et al.*, 2003).

2.2.2 DNA

DNA offers a potential tool for the selective detection of pathogens by means of detecting the presence or absence of genetic sequences found in specific pathogens. A DNA molecule consists of two strands of deoxyribonucleotides held together by hydrogen bonding and takes a random conformation in water. Under slightly basic conditions the DNA molecule becomes negatively charged and a counter ion cloud surrounds the molecule. This counter ion cloud can be displaced in the presence of an electric field, increasing the ionic polarizability of the molecule (Hölzel and Bier, 2003). When an electrostatic field is applied, DNA polarizes, and every part of the DNA orients along the field lines, stretching it into an approximately straight shape. Due to the field non-uniformity, stretched DNA dielectrophoretically moves towards the electrode edge due to positive dielectrophoresis until one end comes into contact. On the basis of this behaviour many researchers have used AC electrokinetics to manipulate DNA (Walti *et al.*, 2007; Lapizco-Encinas and Palomares, 2007; Washizu *et al.*, 1995 and 2004; Dewarrat *et al.*, 2002; Asbury *et al.*, 2002; Washizu, 2005; Tuukkanen *et al.*, 2006; Chou *et al.*, 2002; Kawabata and Washizu, 2001; Yamamoto *et al.*, 2000; Wang *et al.*, 2005). For example, a modified interdigitated microelectrode array, termed "zipper electrode" by the authors, has been reported to concentrate a wide range of nanoparticles of biological interest, such as the influenza virus and DNA (Hübner *et al.*, 2007). Figure 5 shows the fluorescence microscopy recorded for the trapping of stained λ-phage DNA in a floating electrode device 10 sec after the application of an electric field (V = 200 V_{pp}, f = 30 Hz).

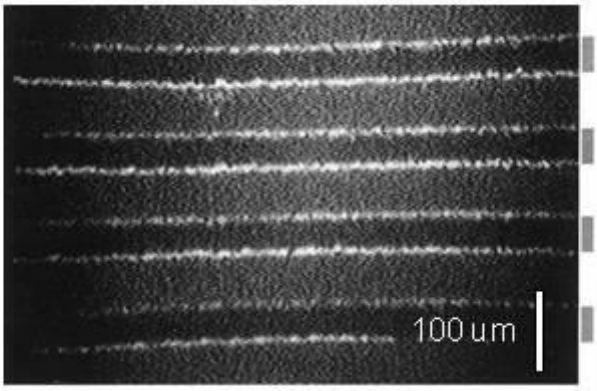

Figure 5: Dielectrophoretic trapping of YOYO stained λ-phage DNA molecules at electrode edges (strips of electrodes indicated by the gray line to the right of the figure) when a 30 Hz, 200 V_{pp} signal is applied *(*Asbury and van den Engh, 1998).

The manipulation of DNA by AC electrokinetic effects has been applied in the biological field and reviewed recently by Washizu (2005). The versatility of DNA allows for it to be used as a sensing, or analytical device and AC electrokinetic effects play an important role in the manipulation of this biological tool. AC Electrokinetics has been used to perform "molecular surgery" for the reproducible cutting of DNA at any desired position along the DNA molecule (Yamamoto *et al.*, 2000). Gene mapping has also found AC electrokinetics useful as a means for manipulating DNA to bring it into contact with enzymes in order to search for binding locations, and thus mapping the gene (Kurosawa *et al.*, 2000). Similarly manipulating and stretching DNA is useful for determining the order of the nucleotide bases for gene sequencing (Washizu *et al.*, 2005), and for measuring molecular sizes by counting base pairs (Washizu and Kurosawa, 1990). AC electrokinetically manipulated DNA can still undergo molecular interactions and has been used to achieve the selective binding of foreign single stranded DNA (Kawabata and Washizu, 2001). As a detection and sensing tool, once the DNA is brought close enough to touch an

electrode, if the electrode edge consists of an electrochemically active metal, such as aluminum, then the DNA becomes permanently anchored there (Washizu *et al.*, 2004). Alternatively, the DNA can be trapped dielectrophoretically and it has been demonstrated by a number of researchers that trapped DNA can be used as a selective bioreceptor towards the development of pathogen biosensors (Gagnon *et al.*, 2008; Lagally *et al.*, 2005; Cheng *et al.*, 1998a; Cheng *et al.*, 1998b).

2.2.3 Viruses

While all particles undergo Brownian motion, the root mean square of the displacement in relation to the size of the particle becomes significant for submicron sized particles, like viruses. To overcome the stochastic motion, the manipulation of submicron sized particles requires deterministic forces large enough to counteract this effect. Since DEP scales with a particle's volume, an electric field gradient of sufficient magnitude must be generated to provide a powerful enough force and necessitates the use of electrodes separated by only a few microns (Mullery *et al.*, 1996; Green and Morgan, 1997). Reducing the dimensions of the electrodes in a biosensor will decrease the voltage required to produce a given electrical field strength and, as a result, reduce both the power dissipated in the system and the temperature increment (Castellanos *et al.*, 2003). This is particularly beneficial for portable systems that run on low power.

A number of reports currently exist on the subject of AC electrokinetic manipulation of viruses (Park *et al.*, 2007; Akin *et al.*, 2004; Wu *et al.*, 2005a; de la Rica *et al.*, 2008; Müller *et al.*, 1996; Schnelle *et al.*, 1996). In many of these cases, successful virus collection results from a combination of DEP and electrohydrodynamic flows (Ramos *et al.*, 1999). In 1998, Green and Morgan reported the manipulation of a mammalian virus, herpes simplex virus type 1, both by positive and negative DEP over a frequency range of 10 kHz-20 MHz using a polynomial

microelectrode array with a gap of 2 μm. More recently, Docoslis *et al.* (2007) demonstrated the collection of *vesicular stomatitis* virus in buffered solutions of physiologically relevant conductivity using microelectrodes with a gap measuring 2 μm across (Figure 6).

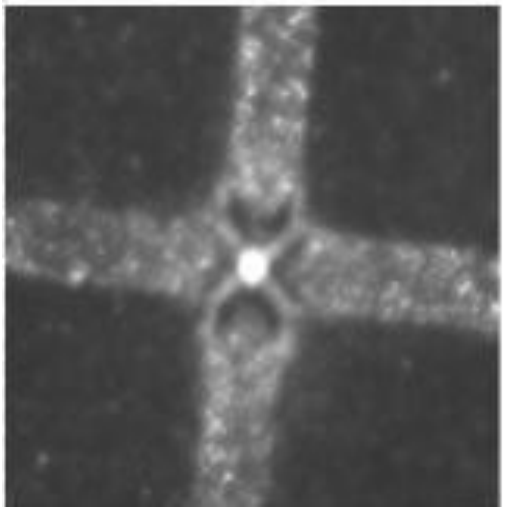

Figure 6: Fluorescence image of nDEP-collected *vesicular stomatitis virus* in TSE after fluorescent staining. The microelectrodes have a central gap measuring 2 μm across. (Docoslis *et al.*, 2007).

2.3 Detection of AC Electrokinetically Trapped Bioparticles

Research over the last decade has shown that there is no shortage of analytical methods that can be successfully interfaced with AC electrokinetically enhanced sampling in a surface-based biosensor. The most promising candidates include methods that rely on optical (absorbance measurement, Raman, confocal microscopy, fluorescent intensity, etc.), mass based (quartz crystal microbalance, surface acoustic wave, etc.), electrical, or electrochemical (potentiometric, amperometric, conductometric, coulometric, impedimetric) (Velusamy *et al.*, 2010) detection. Successful implementation of these methods requires that the concentration amplification effect

achieved by AC electrokinetics be combined with a selective target retention method. The latter can be accomplished with the immobilization of a target-specific molecule, such as a strand of DNA, an antibody, a protein, or an enzyme, or a more complex biological system such as a membrane, cell or tissue (Velusamy *et al.*, 2010). This type of molecular recognition ensures that the captured bioparticle will remain on the sensor surface even after the electric field is turned off. The sensitivity of a surface based biosensor is thus directly affected by the packing density of the sensing element bound to the surface. Methods for surface functionalization have included the use of thiol interactions (Park and Kim, 1998; Radke and Alocilja, 2005; Bhatia *et al.*, 1989), avidin-biotin interactions (Costanzo *et al.*, 2005), self-assembled monolayer coated electrodes (Wana *et al.*, 2009), polymer coated electrodes (Livache *et al.*, 1998) and size specific capillary flow trapping (Hamblin *et al.*, 2010). A number of proof-of-principle studies have demonstrated that a combination of AC electrokinetics with a molecular recognition method can substantially improve the sensitivity of a biosensor (Yang, 2009; Yang *et al.*, 2006; Yang *et al.*, 2008). In principle, decorating the surface of the biosensor with antibodies allows for easy substitution when targeting a multitude of pathogens. The ability to replace specific bioreceptors on demand for the particular screening of a target pathogen gives this method high flexibility.

2.3.1 Optical Detection

Optical and electrochemical sensors tend to be the most popular for pathogen analysis due to their selectivity and sensitivity. In general it is convenient to incorporate conventional optical or electrochemical devices with microfluidic detection systems.

2.3.1.1 Absorbance based measurements

An optical system was first described by Price *et al.*, (1988) to detect dielectrophoretically trapped bacterial cells by monitoring the changes in light absorbance

through the suspension as bacteria collected at an electrode array by pDEP. Later on, Pethig *et al.* (1992) reported a dual beam optical spectrometer with improved sensitivity for the detection of yeast cells collected by both nDEP and pDEP (Talary and Pethig, 1994). The mechanism of pathogen detection by absorbance measurements based on dielectrophoretic immuno-capture is illustrated in Figure 7. The immuno-capture of the bacterial cells under DEP after 15 and 30 min of sampling was found to be 82% and 74% more efficient than that achieved without DEP (Yang, 2009). The immuno-captured bacterial cells were detected by sandwich format ELISA on the chips. The absorbance signals by DEP assisted immuno-capture were reported to be enhanced by 64.7–105.2% for samples containing 10^3–10^6 cells/20 μL (Yang, 2009).

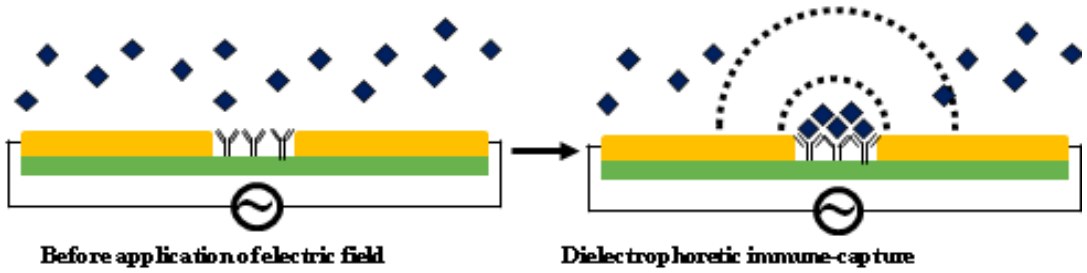

Figure 7: Mechanism of nDEP immuno-capture: The area of collection (inter-electrode gap) is functionalized with a target-specific reactive component, an antibody in this case. Application of a spatially non-uniform electric field (dashed lines) causes nearby antigens to undergo nDEP and collect midway between the electrodes. Once collected, the immobilized antigens can be reacted with an optically active component.

2.3.1.2 Fluorescence-based detection

Fluorescence is by far the most frequently used optical signalling method for the monitoring and detection of AC-electrokinetically trapped bioparticles due to its high level of sensitivity and low background noise (Hübner *et al.*, 2007; Wong *et al.*, 2004b; Cui *et al.*, 2002;

Yang *et al.*, 2008). Using fluorescent imaging, Docoslis *et al.* (2007) detected captured virus (*vesicular stomatitis* virus) and later explored numerical simulations of the system to better understand the processes involved (Wood *et al.*, 2007). The virus was captured from physiologically relevant ionic strength media (880 mS m^{-1}) at low concentrations ($<10^6$ pfu/mL – plaque forming units / mL). The numerical simulations revealed that with a quadrupolar microelectrode the capturing of the virus was achieved by both DEP for the short range capture and electrothermal fluid flow to overcome diffusion limitations. Others were also able to achieve virus capture at low ionic strengths (1-100 mS m^{-1}) and higher particle concentrations ($>10^6$ particles mL^{-1}) (Hughes *et al.*, 1998; Hughes *et al.*, 2001; Pethig *et al.*, 1992; Grom *et al.*, 2006; Morgan and Green, 1997). The dielectrophoretic capture and detection of a food borne pathogen, *Listeria monocytogenes*, was accomplished with the aid of the heat shock protein 60 (Hsp60) immobilized on a sensor's surface (Koo *et al.*, 2009). Hsp60 is a receptor for the Listeria adhesion protein (LAP), a house keeping enzyme of *Listeria monocytogenes* during the intestinal phase infection. Both fluorescent microscopy and ELISA were used to detect the binding of target cells with the receptor. The enhancement of binding with the aid of DEP was found to be 60% higher than without. As discussed in section 3.3, single stranded DNA can be used as a receptor to detect the specific sequence of a pathogen's genetics. Lagally *et al.* (2005) described an integrated system where bacterial cells were electrokinetically concentrated from a continuous-flow and detected via DNA-rRNA hybridization. After being trapped via positive dielectrophoresis, the bacterial cells were lysed by chaotropic salt and the released DNA was denatured by endonuclease. The *E. coli* cells were detected by fluorescent detection via the sequence specific hybridization of an rRNA-directed optical molecular beacon with the denatured DNA. This integrated microsystem is capable of the sequence specific genetic detection of 25

cells within 30 min. After hybridization, the percentage of the fluorescence was observed to increase with time and a linear relationship was found between the number of trapped cells and the percentage of maximum fluorescence. Others have reported the optical detection of cells (e.g., carcinoma cells, malarially-parasitized cells) where DEP was used to separate infected cells from healthy cells. Once lysed, the infected cells were identified with fluorescent probes on a bioelectronic chip (Gascoyne *et al.*, 2004; Cheng *et al.*, 1998a, 1998b).

2.3.1.3 Raman spectroscopy

Raman spectroscopy allows for analyte identification through the inspection of its "chemical fingerprint" on the basis of the vibrational, rotational and other low-frequency modes. Typically, for Raman detection, the signal provided by a low concentration surface based biosensor is not strong enough for detection. The use of surface enhanced Raman scattering (SERS) is often needed and can be achieved through the use of metal nanoparticles. The metal nanoparticles must be either chemically bonded to the bacteria or settle in the proximity of the bacteria in order to increase the scattering (Hou *et al.*, 2007; Cheng *et al.*, 2007). An on-chip detection of pathogens using surface enhanced Raman spectroscopy (SERS) has been reported recently by Hou *et al.* (2007), where the Raman signals of the pathogens were enhanced by the presence of ~80–100 nm silver nanoparticles. Combined with a discharge driven vortex for target concentration, SERS successfully detected cells at a concentration of 10^4 cfu/mL (cfu - colony forming units) (Hou *et al.*, 2007). A continuous flow system for bioparticle sorting was presented by Cheng *et al.* (2007) where, once sorted, the detection of the pathogen was accomplished via SERS. This integrated chip used DEP for a combination of filtering, focusing, sorting and trapping with a throughput of 500 particles/s (Cheng *et al.*, 2007). SERS was also demonstrated without the need for a metal particle suspension by means of a roughened metal surface (Cheng *et*

al., 2010). The presence of the roughened metal surface allowed for the SERS identification of *Staphylococcus aureus* or *Pseudomonas aeruginosa* in blood samples at concentrations as low as 10^6 cfu/mL (Cheng *et al.*, 2010).

2.3.2 Mass Detection

Pathogenic particles with length scales on the order of nanometers can individually weight as little as tens of picograms. In order for mass based detection to succeed, either very sensitive detection methods or significant pathogen amplification is necessary. The following sections will examine how AC electrokinetics has been used to improve the mass based detection sensitivity and sampling for quartz crystal microbalances and cantilever based detection methods.

2.3.2.1 Quartz Crystal Microbalance

A quartz crystal microbalance (QCM) utilizes a piezoelectric quartz crystal that has a fundamental resonance frequency which changes in accordance to the amount of mass attached to the crystal surface. Fatoyinbo *et al.* (2007) developed for the first time an integrated system where yeast cells were concentrated on an electrode surface by DEP and then quantified by a QCM system. The steady-state response predicted from the frequency shift analysis of nanoparticle-loaded DEP-QCM has shown significant improvements in rates of particle detection. The work was done at a concentration of 10^8 nano-spheres/mL and detection was achieved five times faster than other QCM surface loading techniques described in the literature.

2.3.2.2 Cantilever

Similar in concept to the QCM, a cantilever acts as a free-standing platform whose resonant frequency decreases with the addition of mass. Cantilever beams have been employed as sensors by detecting changes in mass via resonant frequency, or deflection (Alvarez and Lechuga,

2010). Cantilever beams which have been employed in two functional modes: detecting changes in mass via resonant frequency, or measuring deflection via changes in the beam's resistance. Ilic *et al.* (2000), first reported a linear relationship between the shift a cantilever's resonant frequency and the number of deposited bacteria. As more bioparticles become deposited on the surface, the shift becomes more pronounced. Alternatively, by measuring the change in resistance of a cantilever beam changes in strain for a cantilever beam can be detected. If the free end of the cantilever is immersed in a antibody containing polymer layer, the action of adsorbing the complimentary virus particles will result in a slight swelling of the polymer layer (Gunter *et al.*, 2003). However, this type of detection is only practical for multi-phase systems. In single phase fluidic systems, while cantilever detection of bioparticles is relatively new, much complimentary work has been done with atomic force microscope (AFM) tips. Specifically, studies relating the frequency response of AFM cantilever beams in solution are directly transferrable to using cantilever micro-electro-mechanical systems in fluidic environments (Sader, 1998; Chon *et al.*, 2000).

The combination of AC electrokinetics with a cantilever beam was recently achieved and allowed for the rapid collection of human cancer cells (Park *et al.*, 2008). Using two conductive cantilevers situated across from one another over a well, Park *et al.* used pDEP to direct the human cancer cells onto the cantilever surface. Figure 8 demonstrates the setup of a series of cantilevers where the change in resonant frequency is measured using a laser Doppler vibrometer. However, sensitivity remained an issue as culturing of up to 7 days was required in order for the cell mass to be detected.

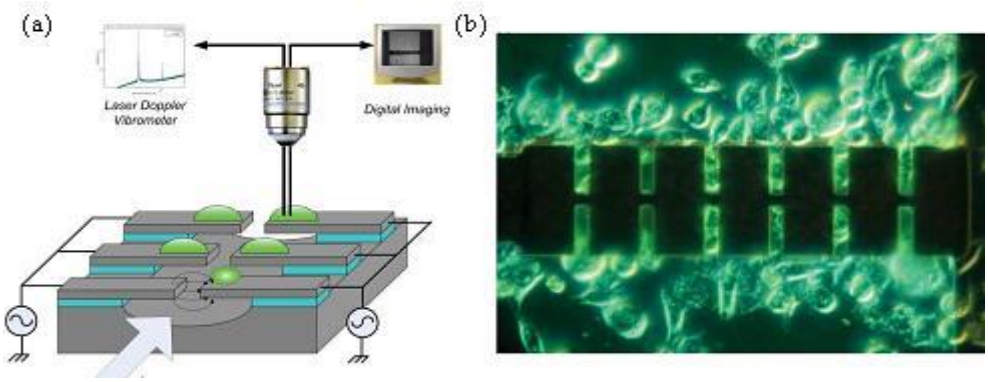

Figure 8: (a) A schematic diagram of pairs of cantilevers. Each opposing cantilever acted as one half of an electrode pair when inducing pDEP. The arrow indicates the direction of flow. (b) A 'living' cantilever with human cervical cancer cells (Park *et al.*, 2008).

The dielectrophoretic assisted capture of human cancer cells was demonstrated using cantilever beams where the cantilever beams acted as the electrodes (Park *et al.*, 2008). Two cantilever beams were needed to create the electric field and required up to 7 days of culturing before detection was realized. The nDEP collection of *E. coli* was achieved by Tomkins *et al.* (2011) through the use of quadrupolar electrodes on a cantilever surface. By using a poly-L-lysine layer on the cantilever to act as a non-specific layer for the electrostatic retention of bacteria, a shift in frequency was detected after 30 minutes of collection from a concentration of 10^8 particles /mL. In order to maximize the sensitivity of a cantilever beam, the most desirable location for collection is at the cantilever tip, furthest away from the anchor. However, Islam *et al.* (2007) successfully applied AC electroosmotic flow to drive polystyrene particles to a point near the anchor and detected a mass change after drying. In more recent work, higher fundamental mode resonant frequencies were used to maximize sensitivity (Gupta *et al.*, 2004).

2.3.3 Detection via Electrical Methods

When biosensors employ an electrical or electrochemical sensing element, many of the features needed for AC electrokinetics are already present. These methods are easier to interface with miniaturized devices than optical methods because they employ electrical signals and do not need an often bulky optical measurement system. Microelectrodes for applied AC electrokinetics can be easily added into a microfluidic channel using standard photolithographic techniques and their integration with an electrical diagnostic chip allows for the sharing of features or power sources. Moreover, some electrical sensing methods do not require a labelling step for sensing target pathogens which makes the on-chip enhanced sampling provided by AC electrokinetics an attractive asset. Electrical sensing methods can be separated into 4 subclasses depending on the type of signal being measured: amperometric (changes in current), conductometric (changes in conductance or resistance), impedimetric (changes in resistance to an AC current), and coulometric (changes in capacitance / permittivity). This section will focus on recent electrical or electrochemical sensing methods that have used AC electrokinetics.

2.3.3.1 Amperometric detection

By measuring the change in current as pathogens pass between a pair of sensing electrodes, it is possible to detect single cells in solution. AC electrokinetics can be used to position or manipulate these single cells into the proper location to achieve sensing. Utilizing the Coulter-counter principle Pandey and White (2004) used dielectrophoresis to detect a single cell (Chinese hamster ovary, CHO) as it was driven to pass through a micro-aperture (10-25μm in diameter, comparable to the size of the cells being tested) in a silicon nitride membrane. Detection of a cell was achieved by recording the decrease in the ionic current caused from the passage of a single cell as it passed through the micro-aperture. Live bacteria were also detected

amperometrically by first using pDEP to trap the bacteria and then using AC induced fluid flow to move the cells until they formed a bridge across micron-sized electrode gaps (Beck *et al.*, 2005). The cells were first captured at the electrode edges by applying an electric field (1.5 V_{pp}, 1MHz). The cells were then transported along the length of the electrode into the gap by exploiting an electric field induced flow at a lower voltage (0.5 V). The two electrodes tapered to a point small enough that a single bacterium would completely bridge the electrodes and detection could be achieved.

2.3.3.2 Conductometric detection

Direct measurement of the conductance between two electrodes with a nano-sized gap can be a highly sensitive technique for detecting bioparticles. A series of reports have been published by Suehiro *et al.* to detect dielectrophoretically trapped bacteria by measuring changes in conductance (1999; 2003a; 2003b; 2003c; 2005; 2006). The bacteria were collected within a small gap (5μm) between the microelectrode arrays by trapping the cells at the electrode edge with pDEP. After collection, an improved detection method was described by this group using electropermeabilization (Suehiro *et al.*, 2003b; 2005). While cells can be destroyed using AC electric fields within a specific frequency window (Menachery and Pethig, 2005), electropermeabilization causes the cell membrane to become permeable in order to increase the apparent conductivity of the trapped bacteria. Once applied, the bacterial cell wall leaks intracellular ions into the surrounding medium and transiently increases the conductance (Figure 9). Using this method, the detection time of yeast cells and *E. coli* cells was observed to shorten by two orders of magnitude to 15 min and 3 hr, respectively and the sensitivity was improved to 10^2 cfu/mL.

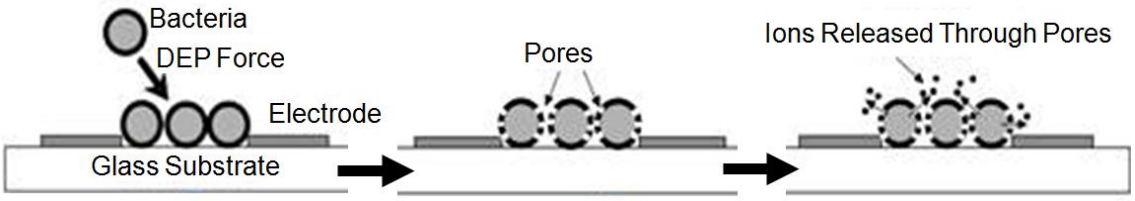

Figure 9: A schematic diagram of electropermeabilization. The cells are first trapped, and then ruptured via an increased electric field followed by the subsequent release of intercellular ions to the surrounding area (Suehiro *et al.*, 2003b).

Selectivity for these detection methods was demonstrated by exploiting the different dielectric properties of cell mixtures. Selective detection of viable cells from a mixture of viable and non-viable cells was achieved using DEP collection at two different electric field frequencies. At 100 kHz the viable and nonviable bacteria were trapped near an electrode corner due to positive DEP and their conductances changed proportionally with time. At 1 MHz only viable bacterial cells were trapped by positive DEP as the conductance change over time was less remarkable (Suehiro *et al.*, 2003c). The increase in conductance indicated that certain areas of the electrode gap had been bridged by trapped bacteria.

To enhance the detection of dielectrophoretically collected particles, metal nanoparticles have been used to transform nonconductive trapped particles into conductive interparticle-connected entities through metal deposition. For example, silver particles attached to DEP trapped bioparticles bridged the gap between two microelectrodes by silver nucleation (Velev and Kaler, 1999). Latex particles coated with protein A were dielectrophoretically trapped between micron-sized gold electrodes and stabilized by a non-ionic surfactant. Adsorption of protein A onto the latex surface yielded a sensing interface for the specific association of the human immunoglobulin (IgG) antigen. The association of the human immunoglobulin on the surface was

probed by the binding of secondary gold labelled anti-human IgG antibodies, followed by the catalytic deposition of a silver layer on the gold nanoparticles. The silver layer bridged the gap between the two microelectrodes, resulting in a resistance of 50-70 Ω, whereas the negative control gave a resistance of 10^3 Ω. The lower detection limit for this model sensor for IgG antibodies was calculated at 2×10^{-13}- 2×10^{-14} M.

2.3.3.3 Impedimetric detection

Impedimetric detection is one of the most promising techniques for developing label-free, real time, and non-invasive methods for bioparticle detection. Milner *et al.* (1998) first proposed a differential impedance method for the quantitative detection of DEP captured bacteria and opened the door for biosensors where non-visible sub-micrometer bioparticles, such as viruses and DNA fragments, could be quantitatively investigated. This is not to suggest that impedimetric detection can only be used in isolation. In conjunction with optical monitoring, impedance has been used for the characterization of prohibitively small bioparticles (Guan *et al.*, 2004).

Dielectrophoretic impedance measurement (DEPIM), a new method reported by Suehiro *et al.*, occurs when there is an impedance change as interdigitated microelectrodes are connected due to the trapping and pearl-chain formation of cells by DEP (Suehiro *et al.*, 1999). A 'pearl-chain' occurs during capture when bioparticles with induced dipoles become dielectrophoretically attracted towards one another due to dipole-dipole attraction and form strings of particles resembling a chain of pearls. This pearl chain can enhance sensing by being electrically connected in parallel within the electrode gap, thus increasing the conductance and capacitance between the electrodes. The conductance, G_t and capacitances, C_t between the electrodes are found to increase proportionally with the increase in cell concentration. By fitting the measured G_t and C_t values, a linear calibration chart was derived that enables the absolute measurements of

cell concentration. This method accurately assayed *E. coli* cells suspended in solution at a concentration of 10^5 cfu/mL within 10 min. Dielectrophoretic capture and subsequent impedance detection has been used to concentrate bacterial cells (*L. monocytogenes)* from dilute solutions (10^5 cfu/mL) in order to detect the metabolic activity of the bacteria and provide enhanced sensitivity for the biosensor (Sjöberg *et al.*, 2005). After trapping the cell on the sensor surface, impedance sensing arose from the differences in the physical properties, *i.e.*, differences in conductivity and permittivity, between the particles and the suspending medium as well as the changes in the geometric form of the collected particle on the electrode array. Other studies found that the changes in the permittivity of the dielectric between the electrodes are proportional to the total volume of the suspending medium replaced by the DEP collected particles (Allsopp *et al.*, 1999). Thus, a linear relationship between the capacitance change and cell concentration was found.

The DEPIM method was further developed with improved selectivity and sensitivity by applying electropermeabilization (Suehiro *et al.*, 2003b), antibody-antigen interactions (Suehiro *et al.*, 2003a; Suehiro *et al.*, 2006; Suehiro *et al.*, 2005) and different DEP forces (Suehiro *et al.*, 2003c). In a series of publications, this group reported the detection of cells with high selectivity by using antigen-antibody reactions (Suehiro *et al.*, 2006). This phenomenon was employed with DEPIM measurement via agglutination and immobilization and is illustrated in Figure 10. An antibody specific to the target bacteria was added to the cell suspension to cause agglutination. pDEP was employed to attract particles to an electrode tip. At the electrode tips, the antibody was in a region of high concentration of the target bacteria, thereby increasing the amount of agglutination. After washing, a second round of DEP collection was used where the conditions of the DEP force and the drag forces were adjusted by varying the strength of the electric field so

that only agglutinated products of the target bacteria were selectively trapped. A second method was proposed where immobilization for DEPIM relied on an electrode coated with immobilized antibodies prior to the experiment. The DEP force was then adjusted to be strong enough to bring bacteria to the chip surface, but not enough to overcome the drag force exerted by the flowing liquid. This allowed for simultaneously trapping the target bacteria by the antibody-antigen and suppressed non-specific bacteria binding.

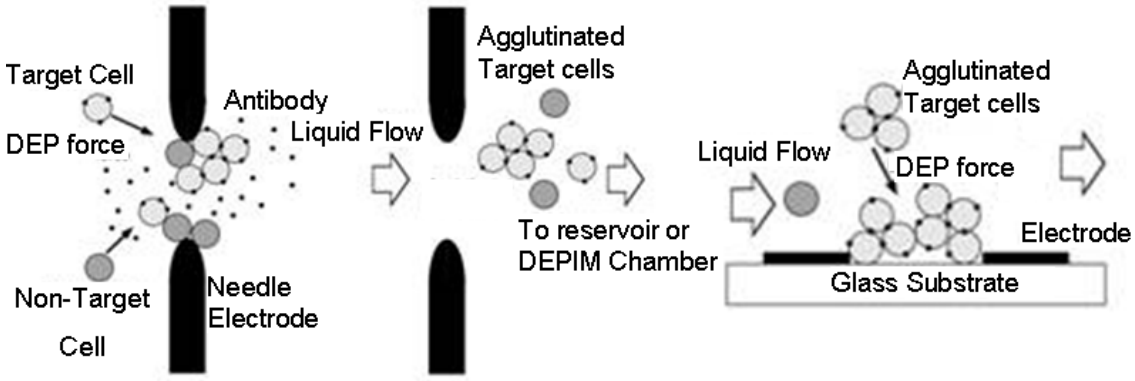

Figure 10: A schematic diagram of DEPIM for agglutinated bacteria. The top schematic demonstrates trapping between electrode tips assisted with pDEP. The target bacteria become agglutinated at the tips and are then washed away to the reservoir. The agglomerates can then be collected more easily as shown in the bottom schematic (Suehiro *et al.*, 2003a; 2003b).

To miniaturize the analytical procedures for microorganism detection, a lab-on-a-chip device integrated with DEP based moving cages was demonstrated where the movement of the cages was achieved through actuation. Coupled with impedance based detection this lab-on-a-chip had no need for fluid flow or external optical components (Medoro *et al.*, 2003). The cells are trapped in a stable levitation under the influence of an electric field and were then moved to a

target location. The DEP cages were observed to shift and merge, consequently increasing the particle concentration within the cage. Impedance detection of *E. coli* in tap water has also been achieved with the AC electroosmotic trapping of bacteria using 1 V_{RMS} at 100 Hz (Wu *et al.*, 2005b). Detection was possible for *E. coli* suspended in tap water at a concentration of 5×10^3 cfu/ml after trapping by AC electroosmosis. From the impedance results it was concluded that the system could detect pathogenic cells at a concentration of 10^4 cell/mL.

Single wall carbon nanotubes (SWCNTs) polarize in the presence of an electric field and can undergo self-assembled aggregation due to dipole-dipole interactions. Furthermore, they are good conductors and can change the conductance between the two microelectrodes by forming a bridge across the electrode gap. The strong dipoles of SWCNTs allow them to absorb onto the bioparticles and in a mixture of SWCNTs with bacteria, the impedimetric detection of bacteria was enhanced. Without CNT under the conditions applied, no bacteria were collected, however, with CNT enhanced DEP capture bacteria were collected and detected, as shown in Figure 11 (Zhou *et al.*, 2006). The authors suggested that the enhanced DEP trapping of bacteria was probably due to the stronger electric fields, and hence stronger DEP forces, generated near the dispersed SWCNTs. The transport time between the bioparticles and the sensor was shown to be greatly reduced and that the bacteria were concentrated and detected in less than 10 min at a concentration of 10^4 particles/mL. Dielectrophoretic collection, impedance detection and characterization of DNA have also been reported by a number of researchers (Hölzel and Bier, 2004; Linko *et al.*, 2009).

Figure 11: CNT (0.2 mg/mL) enhanced collection of *E. coli* bacteria (10^5 cfu/mL) (Zhou *et al.*, 2006).

2.3.3.4 Coulometric detection

In capacitance cytometry, a change in the total capacitance (or permittivity) across a pair of microelectrodes is measured as the individual cell is allowed to pass through a microfluidic channel. As previously mentioned in section 2.2.2, DNA polarizes in an applied low frequency AC electric field. Capacitance measurement is employed by means of detecting and quantifying the polarization response of DNA as the cell passed through a 1 kHz electric field. Capacitance detection of DNA in solution has been applied by measuring the capacitance change between the planar microelectrodes (Henning *et al.*, 2008). Total DNA content of a cell has also been quantified by using capacitance cytometry, a termed coined by the authors to describe the linear relationship between the AC-capacitance and the DNA content (Sohn *et al.*, 2000). A new method was recently published where the capacitive detection of viruses was achieved with an extremely low detection limit by using peptide nanotubes, a concept similar to the enhancement provided by CNT for bacteria that was discussed earlier (de la Rica *et al.*, 2008). Self assembled peptide nanotubes coated with a virus specific antibody were trapped between a pair of electrodes by pDEP. Binding of the virus to the antibody caused a decrease in the permittivity as well as the capacitance between the electrodes due to the lower dielectric constant of the virus than that of

the medium. Compared to other label free optical based transducers, this peptide nanotube based electrical transducer demonstrates a better detection limit for the herpes simplex virus type 2 with a detection limit of 10^2 pfu/mL (plaque forming units) achieved within 1 hr.

Chapter 3 Numerical Simulations and Analysis of AC Electrokinetic trapping with Planar Microelectrode Arrays

In situ observations of sub-micron fluorescent tracers suspended in high ionic strength media sealed in a confined geometry are combined with 3-D simulations in order to provide a better understanding of the synergism between electrothermal flows and dielectrophoresis that cause rapid particle transport and trapping on the surface of planar quadrupolar microelectrodes, respectively. Model particles, in this case protein coated and fluorescent dye impregnated polystyrene spheres, are used because pathogenic particles require biohazard certification, and have stricter restrictions on their use and handling. These model particles are visualized through commonly available equipment like UV light and can be imaged without sample preparation using a scanning electron microscope. Furthermore, these model particles are still characteristic of pathogens in terms of their relative size, density and dielectric properties in the range of frequency being studied. Particle collection is examined using two electrode designs. The comparison of these two designs will provide insight when choosing an appropriate microelectrode design for biosensors setups which exploit AC electrokinetics. This chapter will examine how the use of non-uniform AC electric fields can be used to enhance the sampling of model bioparticles, discuss the various AC electrokinetic forces and electrohydrodynamic flows which affect bioparticles sampling, and compare the effect of temperature during surface functionalization with respect to the collection efficiency of an antibody selective surface.

3.1 Materials and Methods

All chemicals, unless otherwise mentioned, were obtained from Sigma Aldrich, MO.

3.1.1 Numerical Simulations

Simulations were conducted on a Dell Precision 690 dual-core xeon processor with a speed of 3.73 GHz and 16GB of SDRAM. The model equations, along with the appropriate initial and boundary conditions, were solved using the finite element method with the software package Comsol Multiphysics, version 3.3a (Burlington, MA). Experimental observations noted that during steady state collection the motions of the fluorescent tracers in each quadrant of the device were comparable. Therefore, due to the geometrical symmetry, the equations were solved only for one quarter of the total system. A Cartesian coordinate system was employed and is illustrated in Figure 12 . The resulting model was meshed with increasing fineness, with the meshes consisting of approximately 50 to 120 thousand elements (~300-740 thousand degrees of freedom), until no further changes in solution resolution was observed. The solution time was under 2 hours for all mesh resolutions considered. An isometric projection of the T10 wire-frame model used in the simulations is shown as an example in Figure 12b. The model presented in Figure 12b shows one quarter of the microelectrode setup. From top to bottom, the domains include a fluid droplet, the gold electrodes, a silicon dioxide substrate and a silicon substrate. A top down view of the model is presented in Figure 13c. A summary of the model's domains, subdomain expressions, boundary conditions and assumptions are presented in Appendix A.

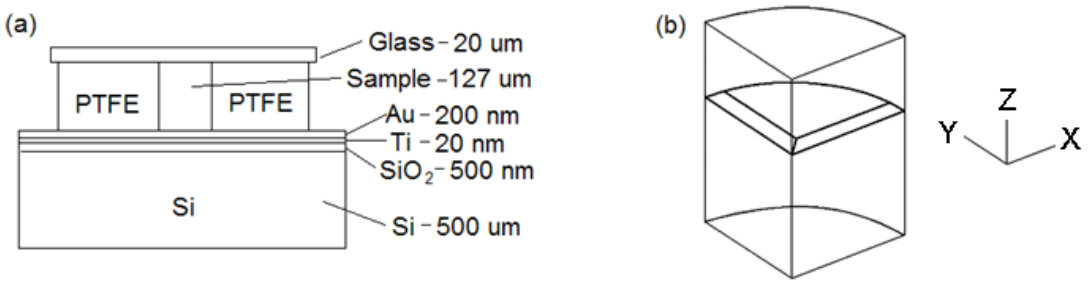

Figure 12: Views illustrating (a) the cross-sectional cut away of the chip including dimensions for thickness and substrate composition and (b) an isometric projection of the 3-D wire-frame model used for simulations.

3.1.1.1 Electromagnetic Equations

For the fluid phase and the substrate materials the frequency of the field was such that an electrostatic approximation was employed to solve for the electrical potential (*i.e.* voltage is not a function of time). The medium permittivity was taken as a function of temperature; the substrate and cantilever permittivities were taken from COMSOL library values (Borosilicate or single-crystal Si, respectively) and assumed constant. Gauss' law which relates the electric field (E) to the charge density (ρ_e) and permittivity (ε_i), is shown in equation 5. The charge density throughout the system was assumed to be negligible.

$$\left(\varepsilon_i \nabla \vec{E}\right) = \rho_e \tag{5}$$

The electrodes were modeled as perfectly conducting materials (gold), with no current source or external charge density applied. The electrical conductivity of the electrodes was taken as constant with respect to temperature. The Laplace equation in equation 6 was used for the electrodes to determine voltage (V).

$$\nabla^2 V = 0 \tag{6}$$

3.1.1.2 Energy Equations

A steady-state approximation was used due to the high frequency of the electric field and, due to order of magnitude considerations; the convective heat flux was neglected in the final equation. This can be justified from the small fluid Peclet number in (equation 7)

$$Pe = Re \cdot Pr = \frac{C_P l_0 u_m \rho}{k} \cong 10^{-4} \quad (7)$$

(l_0 = 10 μm, u_M = 0.1 mm/s, while heat capacity (c_P) and density (ρ) were taken as physical values of water at 21 ℃). Thermal conductivity (k) was taken as a function of temperature for the medium and as constant for the substrates and electrodes. A time-averaged value of the temperature is then calculated from equation 8 with the heat source being the time-averaged value of Joule heating in the system due to the presence of an electric field (E) (Morgan and Green, 2003). The electrical conductivity (σ) is taken as a function of temperature (T) for the fluid and as a constant for the substrates and electrodes. The full energy balance is shown in equation 8 with the simplified version used presented in Appendix A (density – ρ, heat capacity - c_p, time – t).

$$\nabla \cdot (k_i \nabla T) + \sigma \langle \left| \vec{E}_{RMS} \right|^2 \rangle = \rho c_p u \nabla T + \rho c_p \frac{\delta T}{\delta t} \quad (8)$$

3.1.1.3 Momentum Equation

The momentum equation used in the numerical simulation is detailed in Appendix A. It is a simplification of the Navier-Stokes equation with an electrical body force (electrothermal force - f_e / equation 4 on the fluid as shown in equation 9 (density – ρ, fluid velocity – u, time – t, fluid viscosity – μ, pressure – p).

$$\rho\left(\frac{\delta u}{\delta t} + u\nabla u\right) = -\nabla p + \mu\nabla^2 u + \langle\vec{f_e}\rangle \quad (9)$$

A steady-state approximation was used. A time-averaged value of the electric field force on the fluid was used, shown in equation 9, in order to provide a time-averaged steady state approximation of the fluid velocity. From order of magnitude considerations, the inertial term was neglected from the final momentum balance resulting in the Stokes-flow equation. Due to the magnitude of the Grashof number, as shown in equation 10, the effects of fluid buoyancy are negligible (characteristic length – l = 200 nm , gravity – g, temperature – $\Delta T \cong 2K$, volumetric thermal expansion coefficient – $\beta \cong 207$, kinematic viscosity – $\nu \cong 10^{-6}$ m^2/s).

$$Gr = \frac{l^3\beta_T g\Delta T}{\nu^2} \cong 10^{-5} \quad (10)$$

As the density of water varies insignificantly with small temperature rises the continuity equation which solved for fluid velocity (u) is simplified to equation 11.

$$(\nabla \cdot \vec{u}) = 0 \quad (11)$$

The viscosity was treated as a function of temperature, as it has a greater dependence on temperature than density.

3.1.1.4 Particle Motion

The motion of a single particle (dilute case) was modeled ignoring the effects of Brownian motion and fluid buoyancy, with the resulting particle velocity defined in equation 12 (particle mass – m, particle velocity – u_p, time – t, fluid velocity – u_m, friction factor – f, dielectrophoretic force – F_{DEP}).

$$m\frac{d\vec{u}_P}{dt} = f(\vec{u}_M - \vec{u}_P) + \vec{F}_{DEP} \quad (12)$$

Since the ratio of the particle mass to the Stokes factor is negligible (~10^{-9} for 210 nm diameter particles), the particle can be assumed to be at its steady-state velocity at all points. Solving for the particle velocity using equation 12 provides equation 13.

$$\vec{u}_P = \vec{u}_M + \frac{\vec{F}_{DEP}}{f} \quad (13)$$

The particle Peclet number and diffusion coefficient can be calculated from equations 14 and 15, respectively (Boltzman`s constant – k_b, temperature – T, friction factor – f).

$$Pe = \frac{ul_0}{D} \cong 50 \quad (14)$$

$$D = \frac{k_B T}{f} \quad (15)$$

Based on order of magnitude analysis (u_P = 0.1 mm/s, l_0 = r_p, T = 298 K), the Peclet number for 210 nm diameter particles is approximately 50, meaning that the effects of Brownian motion can be neglected. The Archimedes number, relating buoyancy forces to viscous forces, is shown in equation 16 (characteristic length – l = 200 nm , gravity – g, fluid density - ρ_m, particle density - ρ_p, viscosity – $\eta \cong 10^{-3}$ kg /m s).

$$Ar = \frac{l^3 g \rho_m (\rho_m - \rho_p)}{\eta^2} \cong 10^{-9} \quad (16)$$

In the presence of electrical forces and due to the magnitude of the Archimedes number, the effect of buoyancy is negligible compared to the viscous forces (Ramos *et al.*, 1998).

3.1.1.4.1 Particle Lift

Another force that requires attention is the lift forces that act on bodies suspended in a moving fluid. In the presence of a velocity gradient or due to the spinning of the suspended body, particles can experience lift forces. Due to the small Reynolds number and the submicron size of the particles being investigated, the particle is assumed to move at terminal velocities at all times and have virtually no velocity gradient across its diameter, nor would they be expected to spin. However, there are certain situations when these assumptions may not be valid. First, near the dielectrophoretic trap, the dominant force on the particle is expected to be the dielectrophoretic force and the particle may experience a fluid velocity gradient as it moves through or against the bulk flow. Second, near the substrate surface, the particle may experience a large velocity gradient. Finally, particle rotation can occur as particles attempt to align to the electric field. The two lift forces which must be considered are the Saffman force (for non-rotating bodies) and the Magnus force (for rotating bodies).

The Saffman force, presented in equation 17, is a function of the medium viscosity (μ), the relative velocity of the particle ($V=u_m-u_p$), the particle radius (r_p), the shear rate ($\dot{\gamma}$) and the dynamic viscosity (ν).

$$F_S = 81.2\mu V r_p^2 \left(\frac{\dot{\gamma}}{\nu}\right)^{1/2} \tag{17}$$

The Magnus force, presented in equation 18, is a function of the fluid density (ρ), the particle velocity (u_p), the cross section of the particle (A) and a lift coefficient (C_v) which is typically in the range of 0.45 to 0.5 for a sphere.

$$F_M = \frac{1}{2}\rho u_p^2 A C_v \tag{18}$$

Zheng and Silber-Li (2009) examine the effects of the Saffman force close to a wall for 200 nm polystyrene particles. They concluded that in areas close to the wall electrostatic forces would dominate while the effects of lift are negligible far from the wall. The region where lift forces become influential can be determined as a function of the channel height. Based on the numerical simulation and the experimental setup, lift forces have the potential to influence particle movement from 1 um to 3 um from the microelectrode surface. However, this region is also where dielectrophoretic forces would tend to dominate. When using the fluid velocities determined from the numerical simulation an analysis of the ratio of forces reveals that the Saffman force is expected to be 10^{-12} times smaller than the dielectrophoretic force while the Magnus force is expected to be at least 10^{-6} time smaller than the dielectrophoretic force. Therefore, the effect of lift can be considered negligible.

3.1.2 Microelectrodes

Non-uniform AC electric fields were generated by sets of gold microelectrodes fabricated on the surface of oxidized silicon substrates, as shown in Figure 13a and b (SiO_2 thickness: 500 nm). The overall dimensions of each microelectrode chip were 1.5 cm x 1.5 cm. The chips were fabricated using photolithography and metal evaporation (gold deposition) at Queen's University QFAB lab with access granted by Dr. Rob Knobel. The adhesion of the gold electrodes (thickness ~200 nm) to the substrate was facilitated by the deposition of a thin layer (20 nm) of titanium between the gold and silicon oxide. The tip-to-tip separation between opposite electrodes (l) was 10 μm for both electrode designs examined. Prior to each experiment, a PTFE sheet (thickness: 127 μm) having a 1 mm diameter hole was centred on the electrode gap and adhered to the surface of the microelectrode using silicone rubber. Power to the microelectrodes was supplied by

a signal generator (BK Precision 4040A). The microelectrodes were connected to the source in an alternating fashion (180 ° phase difference between adjacent electrodes). The value of the applied voltage (V = 8 Volts, peak-to-peak) and applied frequency (f = 1 MHz), were monitored by an oscilloscope (Tektronix 465). A top-down view of the electrodes is provided in Figure 13, along with references to various planes (A, B and C) used for visualizing the simulation results.

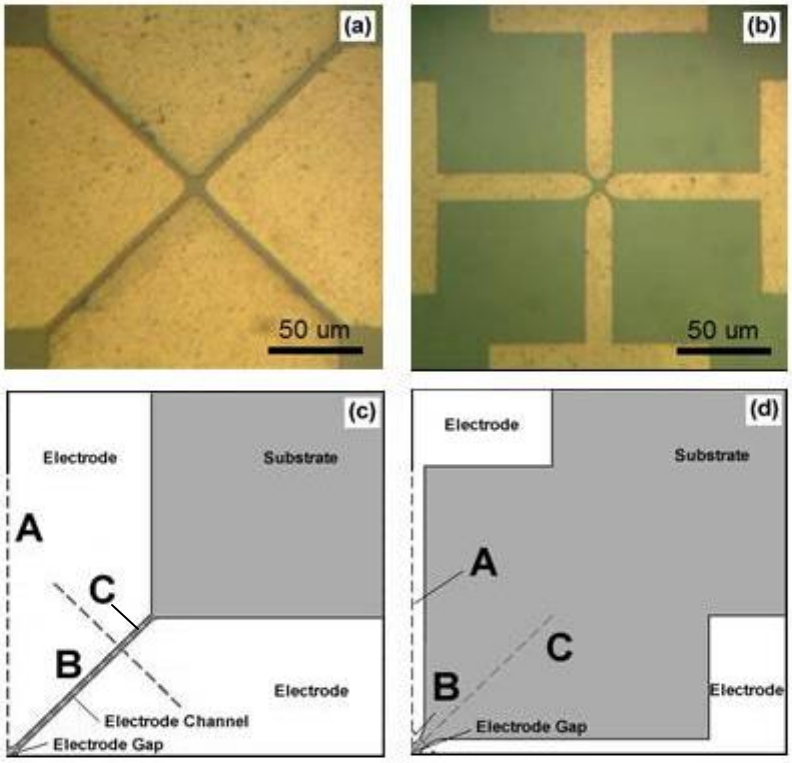

Figure 13: Images of the (a) triangular and (b) circular electrodes at a magnification of 100x where the electrodes are presented as the lighter colour (gold) while the substrate is the darker colour (green). Due to planes of symmetry, simulations were performed for one-quarter of the system. Representations of the one-quarter models in the XY plane for the (c) triangular and (d) circular electrodes are presented with the accompanying visualization planes, A, B and C, as indicated in the figure. Shaded and lighter areas represent the substrate and the electrodes, respectively. All planes extend outward in the positive Z axis from the XY plane. Plane A is taken along the electrode surface along the YZ plane. Plane B is representative of the smallest distance between each pair of electrodes and is perpendicular to the Y=X plane. Plane C is taken at 45 ° to Plane A and is parallel to the Y=X plane. For the triangular electrodes, plane C is parallel to the electrode channel. Plane D (not shown) is parallel to the electrode surface, or the XY plane, and represents a top down view 500 nm above the electrodes. Planes A, B and C extend in the z-direction while plane D is suspended 500 nm in the z-direction above the electrode surface.

3.1.3 Functionalized Microelectrodes

Antibody-functionalized microelectrodes were created by using a procedure adapted from Bhatia *et al.* (1989). In brief, the microelectrodes were rinsed with acetone, ethanol, and deionised water and subsequently cleaned for 30 minutes in solutions of firstly, 50/50 v/v methanol/hydrochloric acid (4.0M), then, 30 wt.% sulphuric acid, and finally boiling deionised water. The microelectrodes were then allowed to dry overnight before transferring to a DRI-LAB dry box (Vacuum Atmospheres Co., CA) and immersed in a 3% by volume solution of (3-mercaptopropyl)trimethoxysilane (MTS) in toluene and allowed to react for two hours. The electrodes were then washed with toluene and allowed to react for 2 hours with the crosslinking agent, N-γ-maleimidobutyryloxy succinimide (GMBS) (MD Biosciences, CA), which was dissolved in a minimum amount of dimethylformamide (DMF) and diluted with ethanol to a final concentration of 5 mM. Finally, the microelectrodes were washed with phosphate buffered saline (PBS) and were allowed to react overnight with a 0.6 mg/mL of anti-avidin (IgG fraction, produced in rabbit, obtained from Polysciences, PA) in PBS solution, after which the substrate was rinsed with PBS. The functionalized microelectrodes were kept immersed in PBS buffer until used. XPS experiments were conducted with a Thermo Instruments 310-F Microlab (Fischer), using a Mg anode gun at an angle of 90 ºdegrees.

3.1.4 Particles and Suspending Media

All experiments were conducted with fluorescently loaded polystyrene microspheres with their respective properties summarized in Table 1. Particles termed 1510TB were obtained from Bangs Laboratories Inc. (Fishers, IN) while particles NAVDY and COOHR were obtained from Invitrogen (Carlsbad, CA). An aqueous solution of KCl having a conductivity of 0.88 S/m, pH of

7.4 (both measured at 21 ℃) and salt concentration of 74 mmol/L was used as the suspending medium.

Table 1: Polystyrene microspheres used for flow visualization and collection

Code	Diameter (nm)	Fluorescent Dye	Surface Modification	Absorption (nm)	Emission (nm)
1510TB	1510	Twilight Blue	-	425	480
NAVDY	210	Yellow-Green	NeutrAvidin®	505	515
COOHR	210	Red	Carboxylate	580	605

3.1.5 Sample Handling and Imaging

All experiments were carried out at room temperature (21 ℃). The particle suspensions were used immediately after dilution and sonicated by means of a sonicating tip with a power output between 7-10 W at 22.5 kHz for as long as necessary to break up any aggregates in solution (typically 0.5-6 hrs). The experiments were performed on a custom-designed stage that supported the microelectrodes and provided connections to the electrical source. Suspensions of particles (10 μL) were dispensed directly into the PTFE well using a micropipette and sealed with a glass cover slip. A cross-sectional cut away of the chip, PTFE and glass cover slip are presented in Figure 12a. Observations of the particle collection patterns on the microelectrodes were conducted with a microscope (Olympus, BX-41) illuminated by means of a mercury short arc fluorescent lamp (OSRAM) coupled to a CCD camera (Lumera, Infinity 3).

3.2 Results and Discussion

3.2.1 Particle Trapping

Observations of particle trapping were performed with carboxyl-modified particles ("COOHR", Table 1) having a diameter of 210 nm and at a concentration of 10^{10} particles/mL. Accumulation of fluorescent tracers in the area between the microelectrode tips was observed to occur in both studied micro-electrode designs (Figure 14). Within less than 20 s after the activation of the electric field, tracers were trapped at a high enough concentration for visual confirmation for both designs. The fluorescence intensity of the particles collected in the electrode gap continued to increase for approximately 10 minutes for the triangular electrodes and for about 4 minutes for the circular electrodes, after which, the size and intensity remained approximately constant. Qualitative observations made during numerous repetitions of the above experiments indicated that particle trapping is detectable earlier with the circular electrodes; however, the triangular electrodes could stably trap larger amounts of particles at steady state (as attested by the higher intensity of the emitted fluorescence signal). The origin of the captured particles, as well as their trajectories into the fluid could not be deduced from experimental observations.

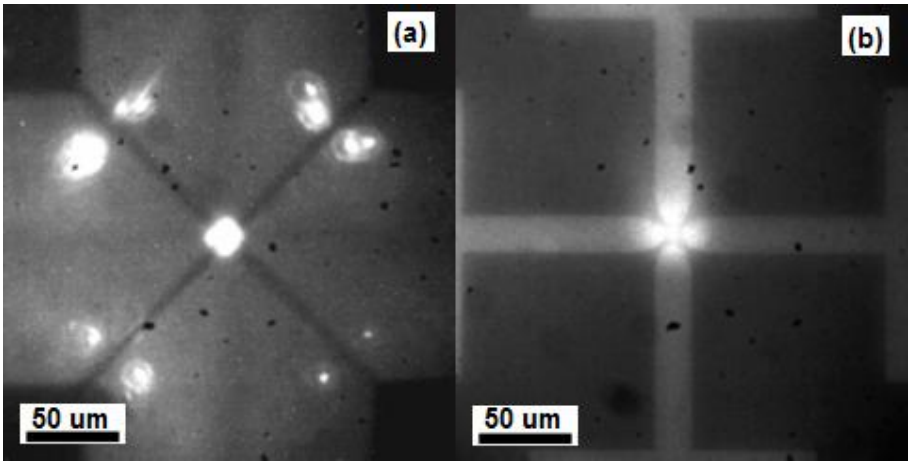

Figure 14: Experimental evidence of particle trapping using 210 nm fluorescently labelled PS spheres. The darkest areas are the substrate, the lighter areas are the electrodes and the bright areas represent localised concentrations of fluorescent particles. Image (a) shows the triangular electrode, (20x magnification) with evidence of collection in the centre and with representative rolls all occurring at the same time. Image (b) shows the circular electrode (20x magnification) with evidence of collection at the centre. The experimental conditions are the same for both types of electrodes (V_{pp} = 8 V, f = 1 MHz, σ_M=880 mS/m, l = 10 μm, particle concentration: 10^{10} particles/mL).

Although the centre of the microelectrode array is the location of stable particle trapping for both electrode designs, additional locations of particle entrapment appear to exist for the triangular electrodes. Specifically, observations with a UV illumination source showed the existence of rolls occurring at locations adjacent to the electrode channel. Observable rolls with high enough concentrations of fluorescent tracers formed in less than thirty seconds, and throughout the entire experiment, all observable rolls (Figure 14a) were sustainable for an average of 5 min. These rolls were observed on both sides of the electrode channels and, although the location that they first appeared was variable, the majority moved over time along the inter-electrode channel until they reached a relatively stable position at a distance approximately 70 μm

from the electrode centre. A maximum number of 8 rolls were found to occur with a pair located on either side of each electrode channel and once the 8 rolls had formed, they existed continually for a period of approximately 15 minutes at which time the experiment was terminated. Morgan and Green (2003) also showed the existence of intense fluid rolls above planar parallel microelectrode strips inside a microfluidic chamber with a height of 200 μm.

3.2.2 Numerical Simulation Results

A better understanding of the forces that caused the observed convective transport and trapping of particles was attempted with the aid of numerical simulations that replicated the above experimental conditions. The real part of the Clausius-Mossotti factor ($R[K_e]$) was calculated from equation 2 by using properties from Docoslis and Alexandridis (2002) and was found to be approximately equal to -0.45. Since convective heat transfer can be neglected in the energy balance, the electromagnetic and energy balance equations were solved independently of the momentum balance. The total effective velocity of a single particle (radius: 105 nm) at any position was calculated from equation 13. The buoyancy force was found to be several orders of magnitude smaller and was not taken into account. The results are presented below in the form of colour plots, indicating particle velocity, and arrow plots, showing the direction of the net force on the particle, along planes A, B, C and D (Figure 15 and Figure 17).

3.2.3 Triangular Tipped Microelectrodes

Figure 15a depicts plane A, which runs normal to the electrode surface and extends from the gap along the axis of symmetry of the electrode. From this viewing angle, a net downward force impelling particles towards the centre of the electrode gap can be observed. Moreover, a flow stagnation zone develops in the area surrounded by the four electrode tips, inside which the dielectrophoretic forces on the particles are stronger than the viscous drag forces.

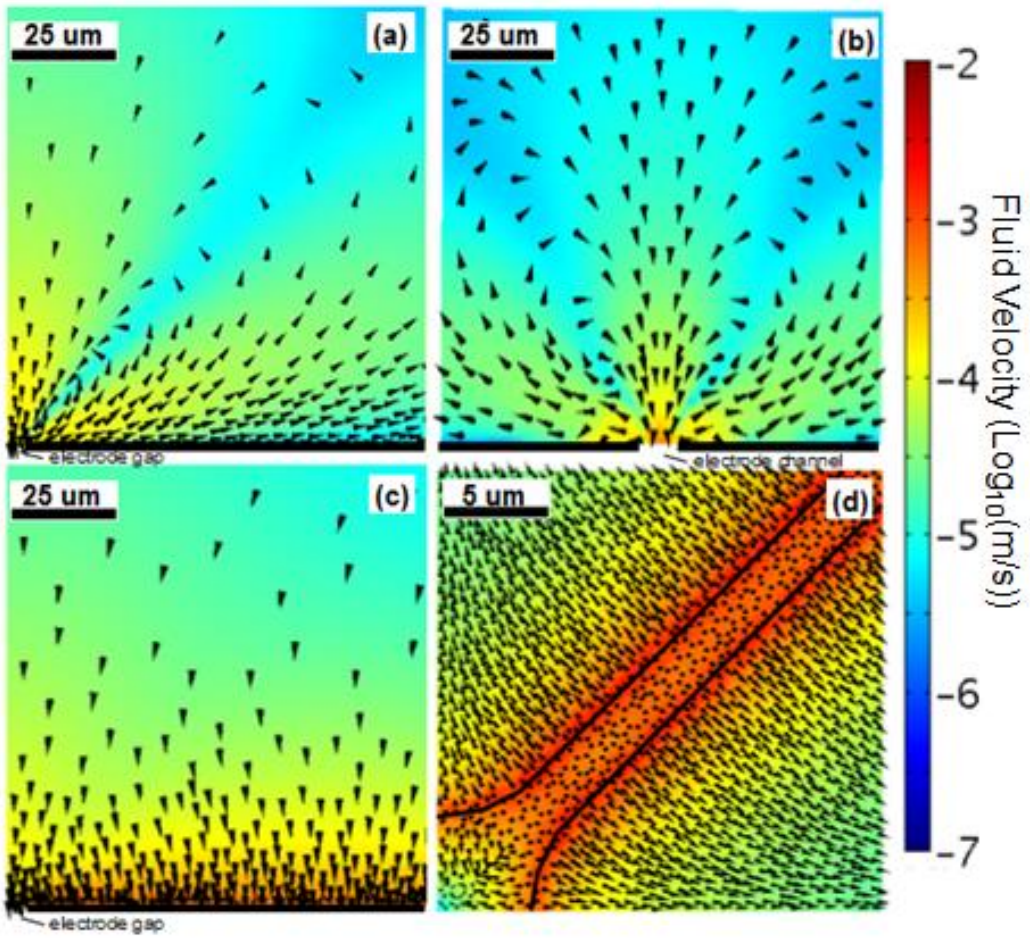

Figure 15: Normalized arrow plots of the triangular electrode indicating the direction of the net forces acting on a particle. Background colour intensity indicates the magnitude of the effective particle velocity having a scale bar in log10(m/s). Visualization planes represent: (a) Plane A: along the electrode surface (YZ plane), 100 μm square with the electrode centre located in the bottom left; (b) Plane B: perpendicular to the electrode channel (perpendicular to the Y=X plane), 100 μm square, centered along the electrode channel with the electrode centre located to the front (coming out of the page); (c) Plane C: parallel to the electrode channel (parallel to the Y=X plane), 107 μm wide and a height of 100 μm with the electrode centre located at the bottom left, and; (d) Plane D: top down view (XY Plane), 20 μm square, with the electrode centre located in the bottom left.

This location acts as a "dielectrophoretic trap", *i.e.*, a collection area for particles undergoing n-DEP (Green *et al.* 1997; Grom *et al.* 2006). Outside this area, particles conveyed to the microelectrode surface are being returned to the bulk of the suspension. Both force and particle velocity are maximal at the electrode tips and decay exponentially with distance. The arrow plot also indicates that the area where this downward force predominates expands upwards in a conical shape, acting to funnel particles towards the electrode gap.

Another interesting flow regime is presented in plane B (Figure 15b), which is normal to the electrode surface and cuts across the inter-electrode gap at a right angle. Immediately to the left and right of the electrode channel, one can observe a pair of rolling patterns with maximum particle velocities occurring at the electrode edges and forces directed along the electrode surface. These currents are driven by gradients in conductivity caused by the temperature profile that develops in the medium. Due to Joule heating, by integrating over the volume of the droplet, the numerical simulations predict a power output of 10 mW which will result in a temperature increase of 1.6 K. Coulombic forces act on the resulting conductivity gradient driving the fluid from low to high areas of conductivity (low to high temperature areas) (Ramos *et al.* 1998) with maximum particle velocities occurring above the electrode edges at speeds reaching 2 mm/s. This fluid motion is responsible for the particle rolls that have been observed experimentally to occur at different locations along the inter-electrode channels (cf. Figure 14a). In Figure 15b, while not readily visible, from the electrode surface to a height of approximately 30 μm the force on a suspended particle is directed away from the electrode centre (into the page), while from 30 μm to a height of 100 μm, the force is directed towards the electrode centre (out of the page). It has been found, however, that the direction of these arrows is subject to the distance of plane B from the electrode centre. This variation can be better visualized in plane C (Figure 15c), which gives an

arrow plot along the centre of the inter-electrode channel. Plane C confirms the downward force experienced by the rolls and the high particle velocities experienced near the electrode channel. If plane B were portrayed within 10 μm of the electrode centre, no rolls would be observable and all forces would point towards the electrode gap. If plane B were drawn approximately 10 μm to 70 μm from the electrode centre, the situation as described above occurs, where the force on the particles at the top of the roll would point towards the electrode gap and at the bottom of the roll would point away from the electrode gap. At a distance greater than 70 μm to the end of the electrode channel, both the top and bottom of the roll point towards the electrode centre. Plane C suggests that there exists an equilibrium distance at approximately 70 μm from the electrode centre where the particles on the bottom feel no driving force either to or away from the electrode centre, yet, these particles are still subjected to a rolling pattern. Figure 15c is presented without the Z component of the net force acting on a suspended particle in Figure 16. The direction of forces acting on a suspended particle in the bottom half converge at an equilibrium location approximately 70 μm from the electrode centre.

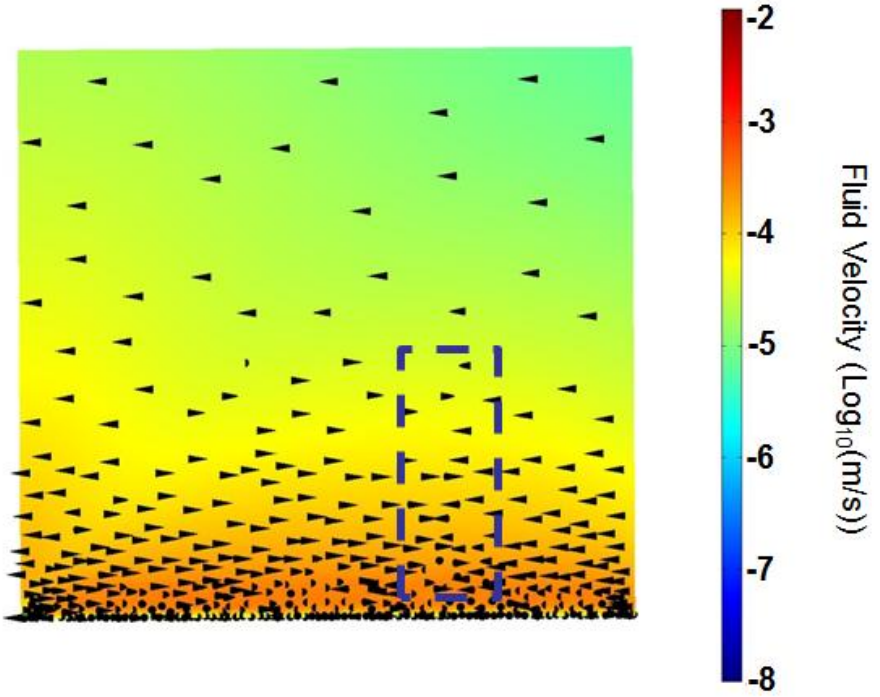

Figure 16: Figure 15c with the z component of the net forces set equal to 0. A dashed box is placed around the area where the equilibrium point is expected to occur.

These observations complement the experimental results since roll formation for 200 nm particles seem particularly stable, and are not prone to move, except when subjected to local and/or random disturbances in the fluid and the majority of rolls are formed, or eventually end up 60 to 70 μm from the electrode centre. Therefore, it appears that rolls created along the inter-electrode channel can cause both particle entrapment and particle focusing into an equilibrium location, which in the present case, was estimated to be approximately 70 μm away from the electrode centre.

Experimental results indicate that, despite the increased concentration of particles present in the fluid rolls, neither discrete particles nor small aggregates were observed to feed into the

electrode gap. Simulations just above the electrode surface (Plane D, Figure 15d) suggest that if a particle were to travel along the electrode surface and begin to drop towards the electrode gap in order to enter the dielectrophoretic trap, the force and fluid flows would deflect this particle away from the centre and back along the electrode surface. Plane D demonstrates that any particle found immediately above the electrode edge would be pushed away and towards areas of decreasing field strength, which, in this case would be passing over and deflected away from the electrode surface. An exception to these observations occurred when particles reached a critical concentration and began acting collectively. When local particle concentration in the rolls increased past a certain point, the pairs of rolls on either side of the electrode channel became disrupted and formed a single vortex while continuing to increase in particle concentration. These clouds of particles periodically fed in bursts into the electrode gap area which subsequently became trapped. This phenomenon, which cannot be explained at the present time, is most likely due to higher-order interactions between the electric field and dense particle formations.

3.2.4 Circular Tipped Microelectrodes

These microelectrodes have the same 10 μm tip-to-tip distance as the triangular electrodes; however, they lack an electrode channel. Plane A, Figure 17a, demonstrates that, similar to the electrodes with triangular tips, particles are funnelled towards the electrode centre from directly above in a conical feature. As was predicted in simulations for the triangular electrodes, a counter-clockwise rolling pattern occurs above the electrode surface. However, there appears to exist a saddle point 13 μm above the electrode surface, approximately 13 μm away from the center of the electrode gap.

Important differences between the two designs can be observed with respect to the microfluidic flows and trapping forces exhibited by the particles. A comparison between Figure

15 and Figure 17 shows that, overall, the circular electrodes cause less intense particle velocities in the bulk of the fluid (reaching a maximum of 1.3 mm/s at the electrode edges), owing to the larger separation between neighbouring electrodes, resulting in smaller temperature increases (thermal increase due to Joule heating would result in a power output of approximately 8 mW resulting in a temperature increase of approximately 0.7K). The comparable reduction in bulk fluid flow for the circular electrodes allows for applications where high fluid velocity is disruptive or undesirable. Moreover, as Figure 17b reveals, this electrode configuration does not cause trapping of particles in rolls at the gaps between adjacent electrodes. Indeed, such rolls of particles were not observed experimentally (cf. Figure 14b).

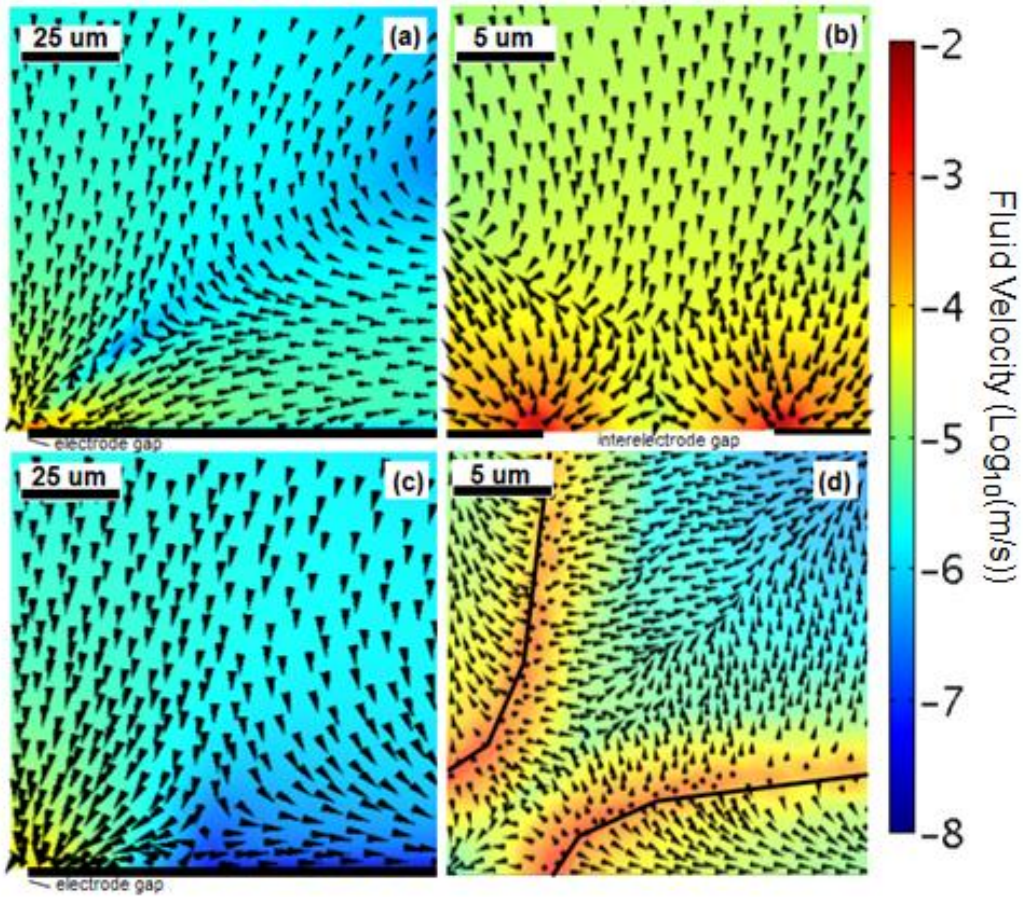

Figure 17: Normalized arrow plots of the circular electrode indicating the direction of the net forces acting on a particle. Background colour intensity indicates the magnitude of the effective particle velocity having a scale bar in $\log_{10}$(m/s). Visualization planes represent: (a) Plane A: along the electrode surface (YZ Plane), 100 μm square with the electrode centre located in the bottom left; (b) Plane B: perpendicular to Plane C (perpendicular to the Y=X plane), 9.9 μm square, centred at the closest distance between the two semicircular electrodes with the electrode centre located to the front (coming out of the page); (c) Plane C: oriented at a 45 ° angle from Plane A (parallel to the Y=X plane), 107 μm wide and a height of 100 μm with the electrode centre located at the bottom left, and; (d) Plane D: top down view (XY plane), 20 μm square, with the electrode centre located in the bottom left.

Another difference between the two electrode designs lies in the areas through which particles can reach the trapping location. In the case of triangular electrodes, discrete particles can reach the microelectrode centre only from directly above, a limitation which is caused by the presence of an electrode channel. As Figure 17c reveals for the circular electrode design, particles found originally near the substrate surface can still pass in between adjacent electrode edges and enter the dielectrophoretic trap. However, if a particle is more than approximately 30 μm from the electrode centre, it will be directed away.

The flows immediately surrounding the electrode centre are best visualized in plane D (Figure 17d), which presents the force profile at a distance equal to 500 nm above the electrode surface. It can be observed that at the point of minimum distance between the two electrodes, the force will either draw the particles into the dielectrophoretic trap, or deflect them away from the electrode centre. Examination of force profiles drawn on the planes at various distances from the surface reveals that the opening through which particles approach the centre becomes wider with distance from the surface and reaches a radius up to 50 μm. Therefore, when comparing the two designs, on the one hand, a larger surface area electrode, such as the triangular electrode, causes more intense particle flows. Conversely, the circular electrodes generate less intense particle flows, while allowing particles to enter the dielectrophoretic trap from directly above the central electrode area, but also via the interelectrode gaps.

In Figure 18, the magnitude of the electric field is presented for each electrode design. The electric field for the triangular electrodes reaches a maximum value of 2.9×10^6 V/m while the maximum value for the circular electrodes is approximately 7.9×10^5 V/m. For each design, the maximum recorded electric field in Plane A occurs at the tip of the electrode. The reason for this difference in the magnitude of the electric field is due to design of the electrode. The electric

field is proportional to the inverse cube of the distance. The cube of ratio of the shortest distance from the tip of the circular electrode to the nearest oppositely charged electrode to that of the shortest distance from the tip of the triangular electrode to the nearest oppositely charged electrode is approximately 3.5. Since the strength of the negative dielectrophoretic trap is a function of the magnitude of the electric field, it is expected that the triangular electrode would have a stronger trap. This is supported by the more intense fluorescent signal observed during collection, as show in Figure 14.

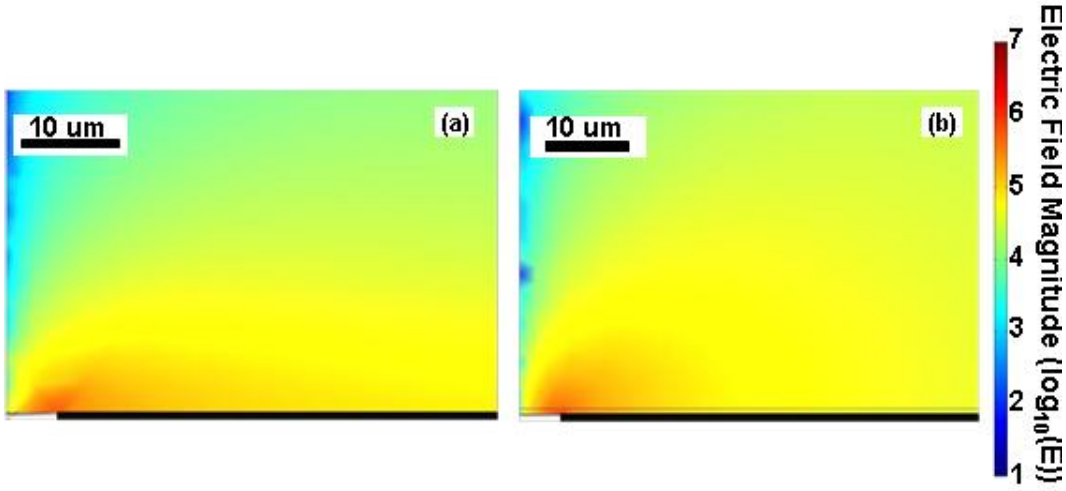

Figure 18: Plot of the magnitude of the electric field across Plane A (YZ Plane) The location of the electrodes is shown in the graphs. The electrodes are represented by the black bar in the bottom left of each graph.

In Figure 19, the ratio of the DEP force divided by the viscous drag force experienced by the particle due to fluid flow is presented for both electrode designs. The DEP force is stronger than the Stokes force only in the proximity to the electrode gap whereas for the remainder of the medium volume, the Stokes force dominates. Since the drag force is much stronger than the DEP

force for nearly the entire effective volume of the medium, particle velocity can be taken as being equal to fluid velocity for dilute concentrations.

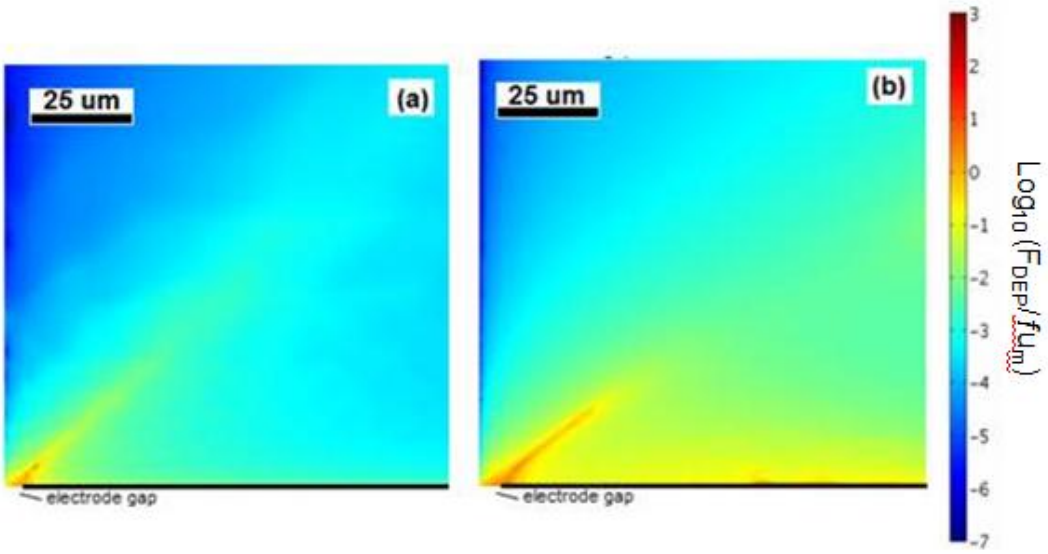

Figure 19: Plot of $\log_{10}(F_{DEP}/f u_m)$ (dielectrophoretic force – F_{DEP}, friction factor – f, fluid velocity – u_m) across Plane A (YZ Plane) provides a comparison between the magnitudes of the forces (dielectrophoretic *vs.* viscous drag force) acting on a single particle in (a) triangular electrodes, and (b) circular electrodes. The electrodes are represented by the black bar in the bottom left of each graph.

Furthermore, by manipulating the electrothermal fluid flow through electrode design, one can similarly alter the size and shape of the effective DEP trapping volume without changing the electric field intensity or the characteristic dimension of the electrode. For both electrode designs in the area directly above the electrode gap, evidenced in Figure 15a and Figure 17a, the fluid force propels particles towards the DEP trap allowing both forces to work in tandem to transfer particles from the bulk to the centre of the electrode for detection and concentration. This supports the experimental observations where the DEP trapping of latex particles occurred in the

interelectrode gap. With the triangular electrode design, Figure 19a, the force on a particle due to fluid flow dominates in the majority of the medium's volume outside of the immediate vicinity of the electrode gap. Conversely, the circular electrodes, Figure 19b, cause less intense fluid flows, which translates into a larger area where the dielectrophoretic force is a significant contribution to particle trajectories.

3.2.5 Experimentally Observed Particle Trajectories

Simulation data predicting fluid flows were compared against experimental observations employing *in situ* fluorescence microscopy of 1510TB particles having a diameter of 1.51 μm and bulk concentration of 2.5 x 10^8 particles/mL. When using small diameter latex particles, fluorescent signals were observable only at the point of particle capture and detection of particle motion was not possible in the fluid. Particles with a larger diameter enable visualization of individual particle trajectories in the area surrounding the electrode gap. In spite of the fact that these particles are larger (hence, the ratio of DEP to fluid forces is higher) than those considered previously (210 nm), the flow patterns predicted are similar for both cases, thus allowing us to extrapolate the conclusions drawn from our experimental observations made on large fluorescence particles to small ones.

The results of these experiments are shown in Figure 20 where the particles are subjected to the same experimental conditions as previously mentioned with an applied voltage of 8 V_{pp} and a frequency of 1 MHz. After a sufficient number of particles were collected from the suspension on the microelectrode surface (Figure 20a and Figure 20b), the field was terminated and the particles were allowed to disperse for several minutes. This dispersion created a highly concentrated area of particles in the vicinity of the electrode gap as shown in Figure 20c and Figure 20d. The electric field was subsequently reapplied with the results shown in Figure 20e

and Figure 20f. At the onset of an electric field, the area immediately surrounding the electrode gap is cleared of particles, either towards the electrode gap, or away from the electrode edges. For the triangular electrodes, particles found directly above an electrode are pushed towards the centre of the electrode and away from the electrode gap. This type of collection produces a pattern reminiscent of a '+' sign. In comparison, when using the circular electrodes, particles experience a different type of four-way dispersion away from the electrode centre. Four of these paths are visible in Figure 20f and form a design in an 'x' shape with particles being directed away from the centre. Based on experimental observations from the accompanying videos to Figure 20a-f, the radius of the funnel above both the circular and triangular electrode gaps can be estimated (videos can be accessed using the links provided with the Tomkins *et al.*, 2008 reference). The triangular electrodes develop a roughly conical funnel which, near the surface, has a radius slightly over 5 μm which is due to the geometry of the electrode gap which similarly has a radius of 5 um. After allowing collected particles to sufficiently disperse, observations above the surface suggest that the cone has a radius approaching 30 ± 3 μm during subsequent collection. Since the microscope being employed is a confocal microscope, only particles within the volume being observed could be traced from the bulk until capture. Based on the numerical simulations (c.f. Figure 15a), this would correspond with in focus observation height from 0 μm to 34 μm.

The funnel above the circular electrode is more irregular in shape. Just above the surface, a roughly circular area centred above the electrode gap having a radius of 10 μm will immediately draw particles downward. Immediately after dispersion, particles above the electrode surface have been collected from as far away as 38 μm. From Figure 17a, the numerical simulation predicts that at a height of 34 μm above the electrode surface, particle collection would occur

from as far away as 32.6 μm. Particles above the substrate where observed to be drawn in at a distance of approximately 23 μm. However, after the initial collection period, the electric field produced with the circular electrode design will visibly draw particles from as far away as 50 μm from the electrode centre. Applying a similar observation height of 34 um, the numerical simulations accurately predict these distances for particles collected above the substrate. From Figure 17c, at a height of 34 μm, the most intense fluid flows (indicated in yellow near the electrode gap) occur within a 23.8 um radius of the centre. However, at the same 20 μm height, the numerical simulation predicts that particles as far away as 50.5 μm would still be subjected to forces directing them into the electrode gap, albeit at fluid velocities 2 magnitudes smaller. This decreased fluid velocity would explain why particles farther from the centre are not immediately drawn into the dielectrophoretic trap. The distance from which a particle can be drawn into the microelectrode gap is a function of the electrothermal flows. Therefore, these distances can be manipulated by the careful design of the microelectrode geometries.

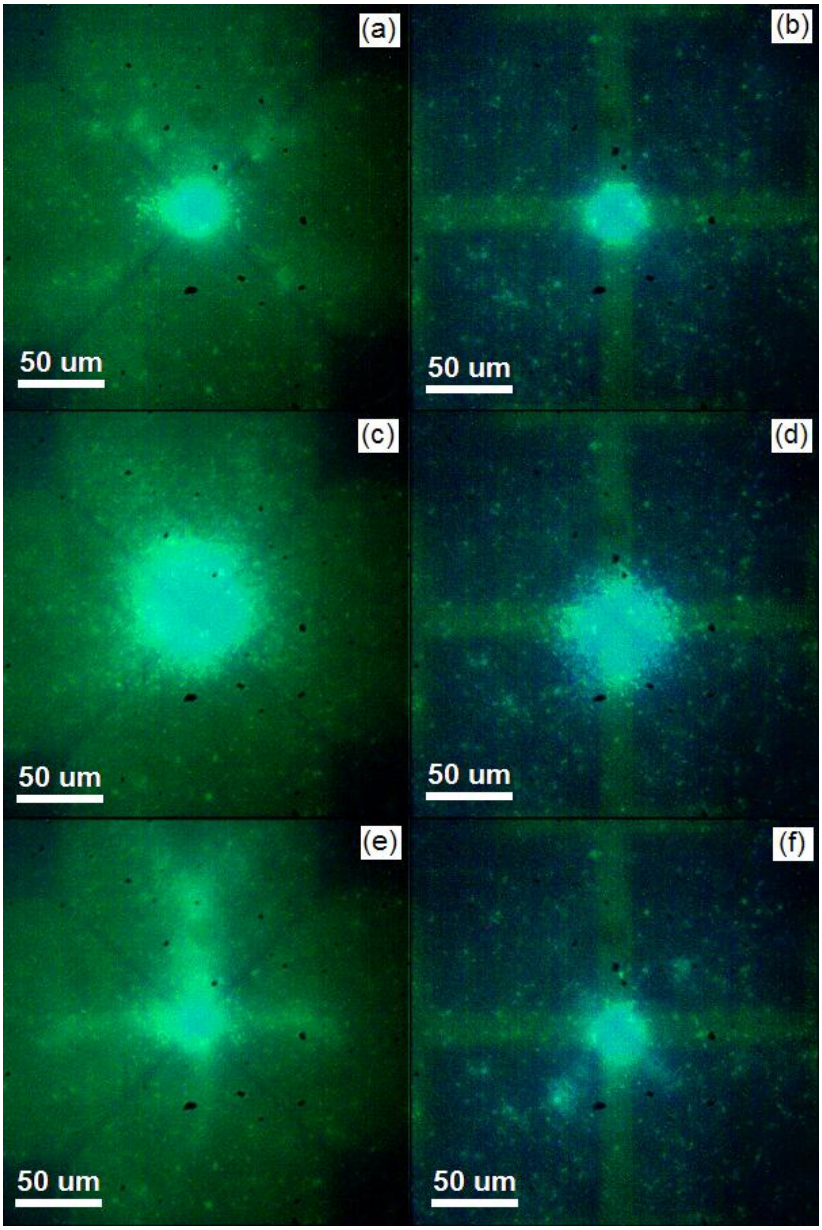

Figure 20: Experimental evidence of particle trapping using 1510TB. Inserts (a) and (b) show the triangular and circular electrodes after a sufficient period of collection, while inserts (c) and (d) represent the electrodes after a brief period of dispersion. Inserts (e) and (f) show the effect of an electric field approximately 2 s after being applied. Experimental conditions: V_{pp} = 8 V, f = 1 MHz, σ_M=880 mS/m, l= 10 μm. Bulk particle concentration: $2.5x10^8$ particles/mL.

The observations collected here using the 1.51 μm particles verify the predictions of the computer simulations. The presence of long inter-electrode channels (triangular electrodes) inhibits movement either towards or away from the electrode gap. As particles pass down from above the electrode gap, if they do not feed directly into the dielectrophoretic trap, they must pass along the electrode surfaces and back out into the bulk. The absence of channels (circular electrodes), as predicted by the simulations and shown in Plane D, Figure 17d, causes fluid flows that point away from the electrode gap, either traveling along the electrode surface or along plane C. Observations suggest that particles deflected along plane C can become re-entrained into the funnel centred above the electrode gap if they reach a sufficient height before the electrokinetic/electrohydrodynamic effects become negligible and the particle can be considered part of the bulk medium.

3.2.6 Functionalized Microelectrodes

In order to combine accelerated sampling with detection of pathogens in surface based biosensors, the surface of the sensor must have a dual functionality, i.e., it should serve both as microelectrode support and a substrate for signal transduction, triggered by the selective capture of target particles. The concept is briefly explored here with a proof-of-principle experiment which illustrates that antibody-functionalized quadrupolar microelectrode surfaces can cause selective and stable capture/concentration amplification of antigen-coated fluorescent latex particles.

3.2.6.1 Selective Surface Based Biosensor

Multiple sets of circular electrodes were functionalized with anti-avidin as described earlier and allowed to collect particles from solution for a period ranging from 15 to 25 minutes. It should be noted that, although the collection of particles was almost instantaneous, the electric field was left on for several minutes in order to keep the particles trapped, thus allowing time for a sufficient amount of antigen-antibody binding to take place. The number of particles collected on the surface while an electric field was applied are comparable to the collection seen with non-functionalized surfaces, as evidenced from Figure 21a and Figure 21b where the collection of COOHR and NAVDY particles are presented, respectively. Once the electric field was terminated, the microelectrodes were repeatedly washed with deionised water and examined using a 14 s exposure time to detect any traces of fluorescence. Fluorescent signals were detected optically with microelectrodes which had collected NAVDY particles while no fluorescent signal was discernable with microelectrodes which had collected COOHR particles. These results were confirmed using scanning electron microscopy (SEM) and presented in Figure 21c (COOHR particles) and Figure 21d (NAVDY particles). No particles were detected anywhere on the microelectrodes having collected COOHR particles either in the electrode gap or in areas away from the center. For microelectrodes having collected NAVDY particles, Figure 20d, the concentration of particles in the electrode gap was found to be 8.4 particles per 10 μm^2. This concentration is higher than that corresponding to the immediately surrounding area, (interelectrode gaps), which was only 3.4 particles per 10 μm^2. Due to the nature of the surface functionalization of microelectrodes, the entire surface has been functionalized with anti-avidin and therefore, the collection of particles can occur for all non-electrode covered areas of the substrate.

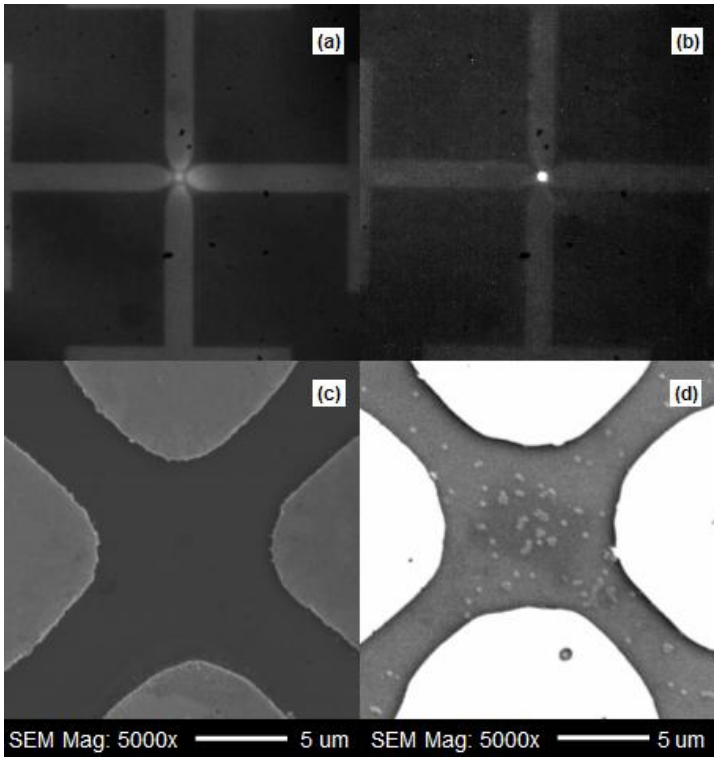

Figure 21: Experimental evidence of collection and retention of 210 nm particles in functionalised microelectrodes. The darkest areas are the substrate, the lighter areas are the electrodes. Locally concentrated fluorescent particles are shown in inserts (a), (b) and (d). Inserts (a) and (b) show collection of non-functionalized (COOHR) particles (control sample) and avidin functionalized (NAVDY) particles, respectively, while the electric field was on. Inserts (c) and (d) are SEM images of the chips presented in (a) and (b), respectively, after being washed with deionised water and dried overnight. Experimental conditions: V_{pp} = 8 V, f = 1 MHz, σ_M=880 mS/m, l= 10 μm. Bulk particle concentration: 10^{10} particles/mL.

Several randomly selected regions away from the electrode gap, where convective transport to the surface is expected to be minimal, were also examined. It was found that the concentration of particles in those areas was 2.8±1.1 particles per 10 μm^2 (error given as one standard deviation with a sample population of N=17). According to these results, the synergism

of a focused convective electrothermal flow and dielectrophoretic trapping can enhance the concentration of particles on a surface by a factor of three.

3.2.6.2 Improving Collection Efficiency

Based on the observations from a variety of experiments at various concentrations, the number of particles present after washing on a functionalized surface (Figure 21d), appeared to represent only a small fraction of the number of particles collected. Even taking into account that particle collections observed could potentially consist of multiple layers of particles that would not necessarily be in contact with the sensor surface, the degree of collection suggested that further examination was necessary.

The literature suggests that opinion is divided on the optimum reaction temperature for the functionalization of silicon when using short chain bifunctional molecules. In some analyses, the reports of higher temperatures suggest that packing is improved (Pasternack *et al.*, 2008). For others, a higher temperature causes unfavourable side reactions by oxidizing the thiol group (Senkevich *et al.*, 2002). In order to examine the effect of temperature several samples were prepared and analyzed via XPS at multiple stages in the surface functionalization procedure. Figure 22 presents the XPS scan of two silicon substrates, one of which was functionalized with MTS at a temperature of 25 ℃, while the other was functionalized with MTS at 80 ℃. For both samples, a peak is present at the 163.5 eV which is characteristic for sulphur containing samples and represents the $2p_{3/2}$ energy level. For the silicon samples prepared at 80 ℃, a band is also present at 169 eV, indicative of the presence of a sulphate. Both samples appear to have a shoulder at 162 eV which may be indicative of the mercaptan, which are normally found in the 162-163 eV range (Moulder *et al.*, 1995). Based on the proposed reaction scheme in Figure 23,

any MTS whose thiol functional group which has been converted to sulphate would be unable to bind the GMBS crosslinking agent and therefore unable to bind the target antibody.

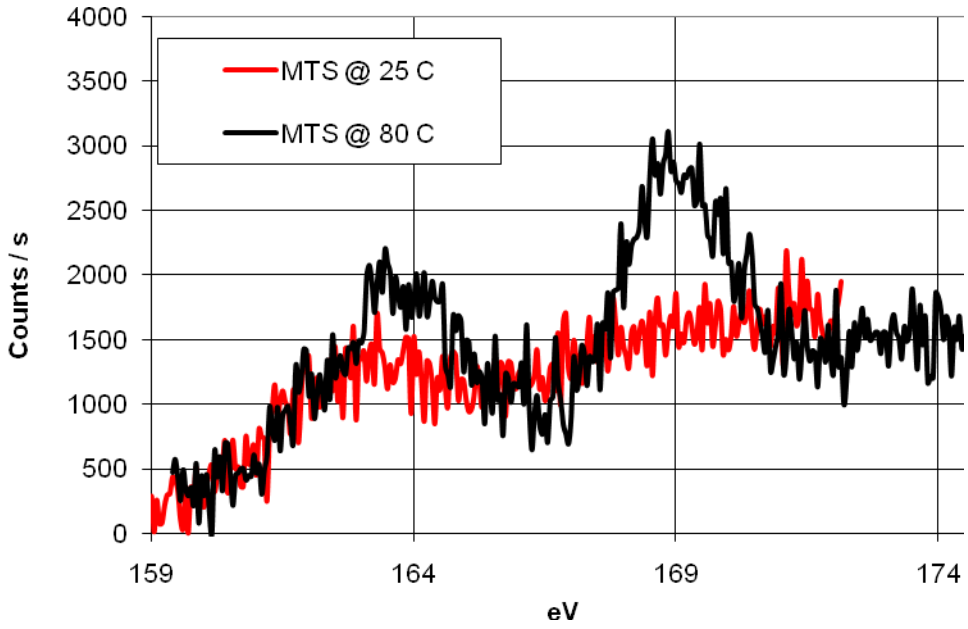

Figure 22: XPS scans in the range of the sulphur 2p peak for silicon functionalized with 3-mercaptopropyltrimethoxysilane. The red line shows silicon functionalized with MTS at 25 ℃ while the black line shows silicon functionalized with MTS at 80 ℃.

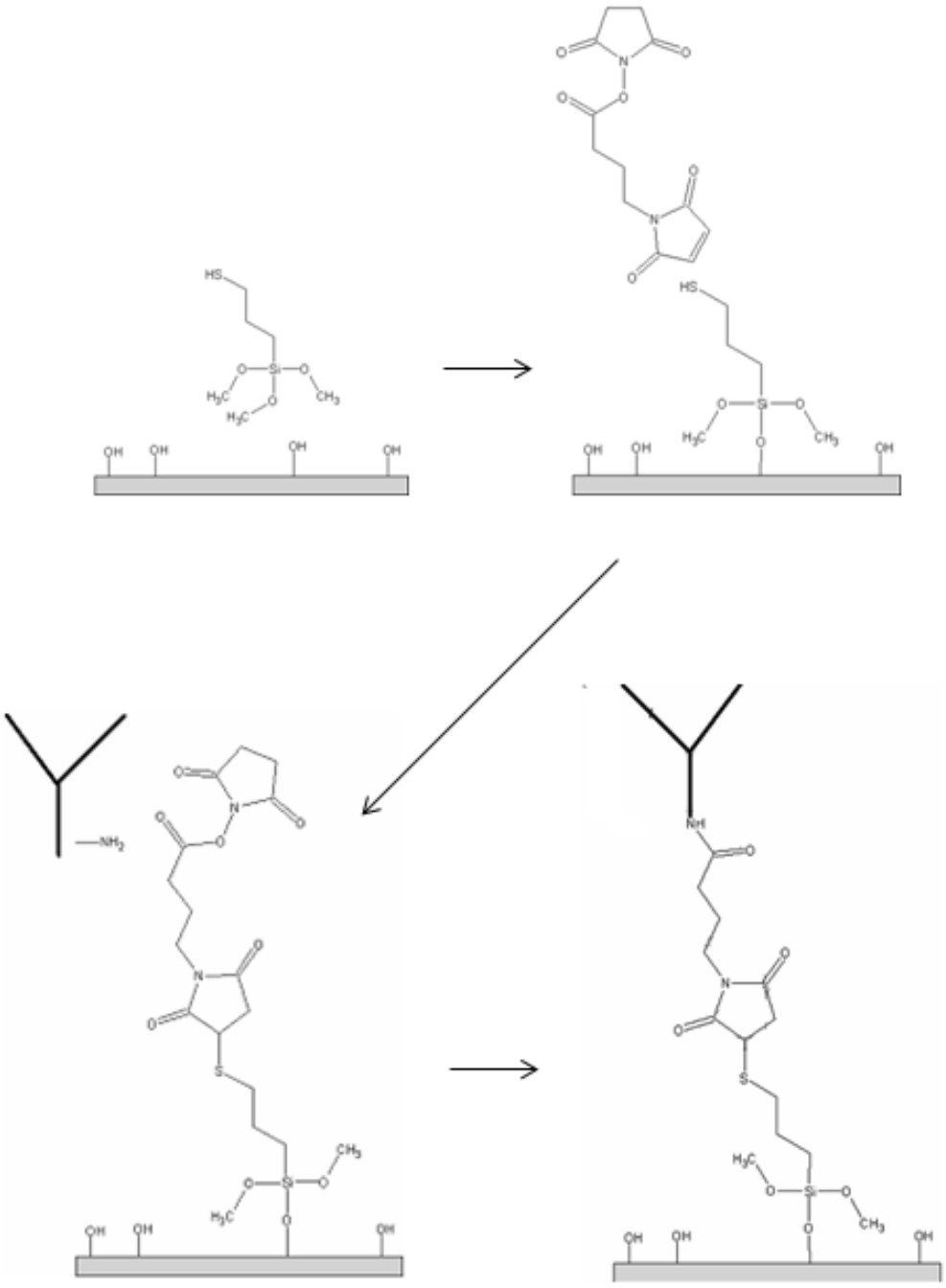

Figure 23: Proposed reaction scheme of surface functionalization. From left to right is the introduction of: 1) 3-mercaptopropyltrimethoxysilane; 2) N-γ-maleimidobutyryloxy succinimide; 3) an amine terminated antibody; and 4) a silicon substrate with a covalently bound antibody

The XPS scans for chips functionalized at 80 ℃ are presented in Figure 24. After functionalization with GMBS, the sulphate peak as well as the sulphur peak is reduced. Subsequent reaction with the antibody reduces the intensity of the sulphate peak. This can be explained by the nature of XPS which can typically only scan several nanometers into the surface of a sample. The fact that the intensity of the peak decreases with subsequent functionalization steps suggests that the MTS layer at the bottom of the sample is being successfully reacted and covered by the layers closer to the surface.

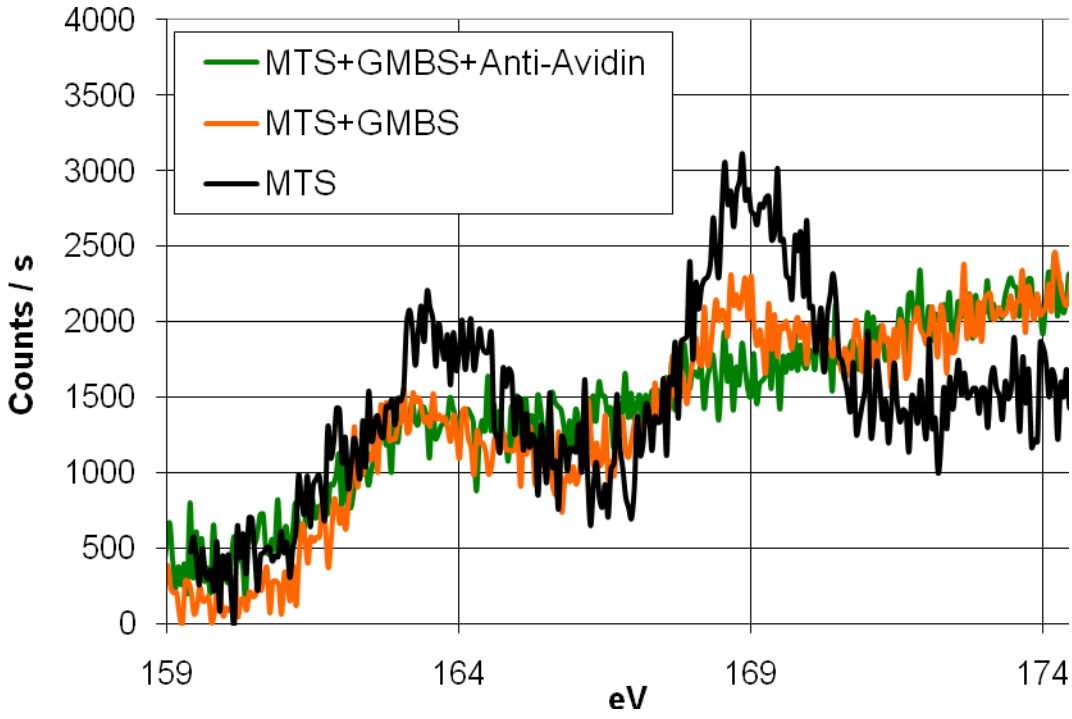

Figure 24: XPS scans in the range of the sulphur 2p peak for silicon functionalized with 3-mercaptopropyltrimethoxysilane at 80 ℃. The black line is silicon functionalized with MTS. The orange line is silicon functionalized with MTS and then GMBS. silicon functionalized with MTS. The green line is silicon functionalized with MTS, then GMBS and then anti-avidin.

Despite the issues with sulphate production during functionalization, in comparison with Figure 21d which shows the collection of NAVDY particles with a microelectrode functionalized at 25 ℃, Figure 25 is collection of NAVCY particles under the same conditions and concentrations with a microelectrode functionalized at 80 ℃. Given the improvement of capture efficiency, functionalization at 80 ℃ outweighs any potential negatives with the conversion of some of MTS`s thiol groups to sulphate.

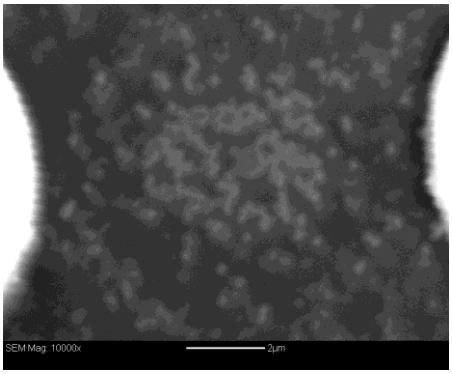

Figure 25: Collection and retention of NAVDY particles after being washed with phosphate buffered saline. The darkest areas are the substrate, the white areas are the electrodes and the light coloured circular particles in the center are the 210 nm PS particles. Experimental conditions: V_{pp} = 8 V, f = 1 MHz, σ_M=880 mS/m, l= 10 µm. Bulk particle concentration: 10^{10} particles/mL.

3.2.6.3 Chip Regeneration

While most biosensors are intended for single use to limit cross contamination and false positives, the potential for a re-usable biosensor would be both environmentally friendly and cost effective. In Figure 26, a methodology is presented whereby a freshly functionalized microelectrode employing AC electrokinetics is re-used for the detection of protein coated particles. In the top left, NAVDY particles are collected for a period of 30 minutes. After

collection, the microelectrode is cleaned using a mild acid of HCl with a pH of 3.0. Changing the pH for a protein in solution can cause denaturation, although too much acid can cause irreversible denaturation. An acid was used because most proteins have an isoelectric point of less than 7 (Thommes and Gottschalk, 2009) and HCl was readily available. A high exposure low intensity visible light image bathed in UV light of the chip after washing with HCl is presented in the top right. The chip was then re-used under the same conditions as before to once again collect NAVDY particles although the intensity of the fluorescent signal is reduced. This suggests that there may be a loss in efficiency with repeated regeneration. After subsequent washing, a similar high exposure low intensity visible light image bathed in UV light is presented in the bottom right where the NAVDY particles are visible as the green collection in the centre.

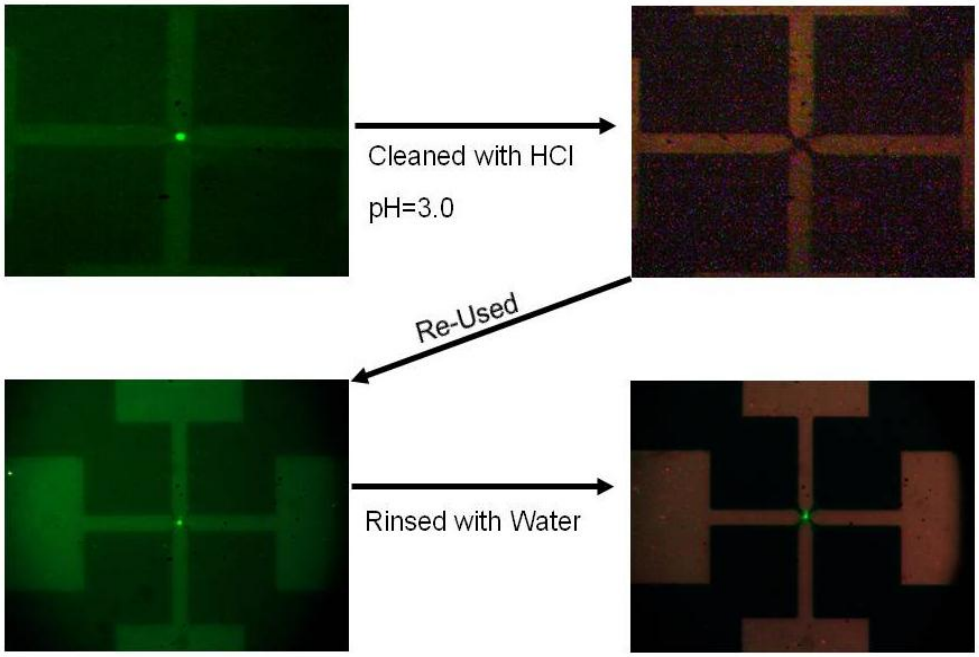

Figure 26: NAVDY particles collected on an anti-avidin functionalized circular electrode, rinsed with HCl, and then collected once again and rinsed again. Experimental conditions: V_{pp} = 8 V, f = 1 MHz, σ_M = 880 mS/m, l= 10 μm. Bulk particle concentration: 10^{10} particles/mL.

3.3 Conclusions

Three-dimensional numerical simulations have been combined with *in situ* fluorescence microscopy in order to illustrate how AC electrokinetic effects created by energized microfabricated quadrupolar electrodes can cause accelerated particle transport and capture onto a surface inside media of high ionic strength sealed in a confined geometry. The experimental observations involving micrometer and sub-micrometer fluorescent latex particles were in qualitative agreement with the simulation results, which indicate that the particles are transported by electrothermally induced fluid flow to the microelectrode vicinity where retention in the centre of the electrode array (flow stagnation area) is accomplished by dielectrophoresis.

The numerical and experimental results also show that the microelectrode design can influence the trapping mechanism. The triangular electrodes presented, having a higher electrode edge length and a larger temperature gradient than the circular electrodes, generated flows up to four times faster and resulted in greater fluid circulation. The existence of parallel channels in this electrode design led to the formation of rolling patterns which did not directly assist in particle collection. Both, triangular and circular electrodes were found to generate electrothermal fluid flows directed from above the electrodes' centre, causing dielectrophoretic particle entrapment. An important finding, resulting from the comparison between the two electrode designs, is that the absence of an electrode channel in the circular electrode design allows for particles to be drawn into the dielectrophoretic trap through the interelectrode gaps, an advantage over the triangular electrode design. Regardless of electrode design, when creating an antigen specific surface covered in antibodies, it was found that using a temperature of 80 ℃ during the MTS functionalization stage allowed for more target antigen particles to be captured during sampling. Finally, using a silicon microelectrode surface functionalized with antibodies, the potential for

regeneration was explored. These results present a first step towards the development of fully integrated *in situ* biosensors, where the time efficient sampling and concentration amplification of the detection agent is achieved using microelectrodes embedded on a sensor's surface.

Chapter 4 Coupled Cantilever-Microelectrode biosensor for the enhanced detection of pathogenic particles

Cantilever based biosensors have the capability to act as label free detectors of bioparticles since they rely on changes in mass for detection. Pathogenic bioparticles that are the size of bacteria are more easily detected than viruses since they have more mass. The bacterium *Escherichia coli* can contaminate low conductivity (<30 mS/m) water samples, like drinking water, and a need exists for their rapid detection. Applying the techniques explored in Chapter 3, the accelerated collection and detection of *E. coli* captured on the surface of a cantilever with the aid of AC electrokinetic effects (dielectrophoresis) is presented as a novel coupled biosensor. Of particular interest in the development of this prototype is how the placement of the electrodes in relation to the cantilever will influence the nature and direction of the fluid flows and forces on the suspended particles. In order to investigate these effects, two cantilever/microelectrode configurations are simulated numerically. Based on the simulations the detection of *E. coli* without the need for cultivation is investigated by employing a prototype device that combines microelectrodes embedded directly onto the surface of a cantilever beam.

4.1 Materials and Methods

Unless otherwise specified, all chemicals were supplied by Sigma-Aldrich (MO).

4.1.1 Numerical Simulation

Simulations were conducted on a Dell Precision 690 dual-core xeon processor with a speed of 3.73 GHz and 16GB of SDRAM. The model equations, along with the appropriate initial and boundary conditions, were solved using the finite element method with the software package

Comsol Multiphysics, version 3.4 (Burlington, MA). Due to lack of internal symmetry, the equations were solved for the total system. The resulting model was meshed with decreasing fineness, with the meshes consisting of approximately 100 thousand elements (~740 thousand degrees of freedom). The solution time was less than 1 hour for all mesh resolutions considered. The isometric projection of the wire-frame models used in the simulations is shown Figure 27a and Figure 27b. The substrate was modeled as borosilicate while the cantilever beams were modeled as single-crystal silicon. In each design, a 20 μm deep well of borosilicate was present which was modeled to have a droplet of purified water. The medium conductivity was modeled as a function of temperature using a least squares quadratic fit with data from the CRC Handbook (Marshall, 2012) for filtered water with a conductivity of $5.5 \cdot 10^{-6}$ S/m at 25 ℃. Each droplet was modeled with a radius of 500 μm, extended 500 μm above the surface of the cantilever beam and was considered to be in a sealed geometry. The equation framework used was the same as that presented in section 3.1.1. For the simulated particles, the diameter of the particle used in predicting net forces was 1145 nm, the diameter of an equivalent volume sphere representing an *E. coli* bacterium. The simulations were modeled with a real part of the Clausius-Mossotti factor of 0.95 to evaluate the flows under positive DEP.

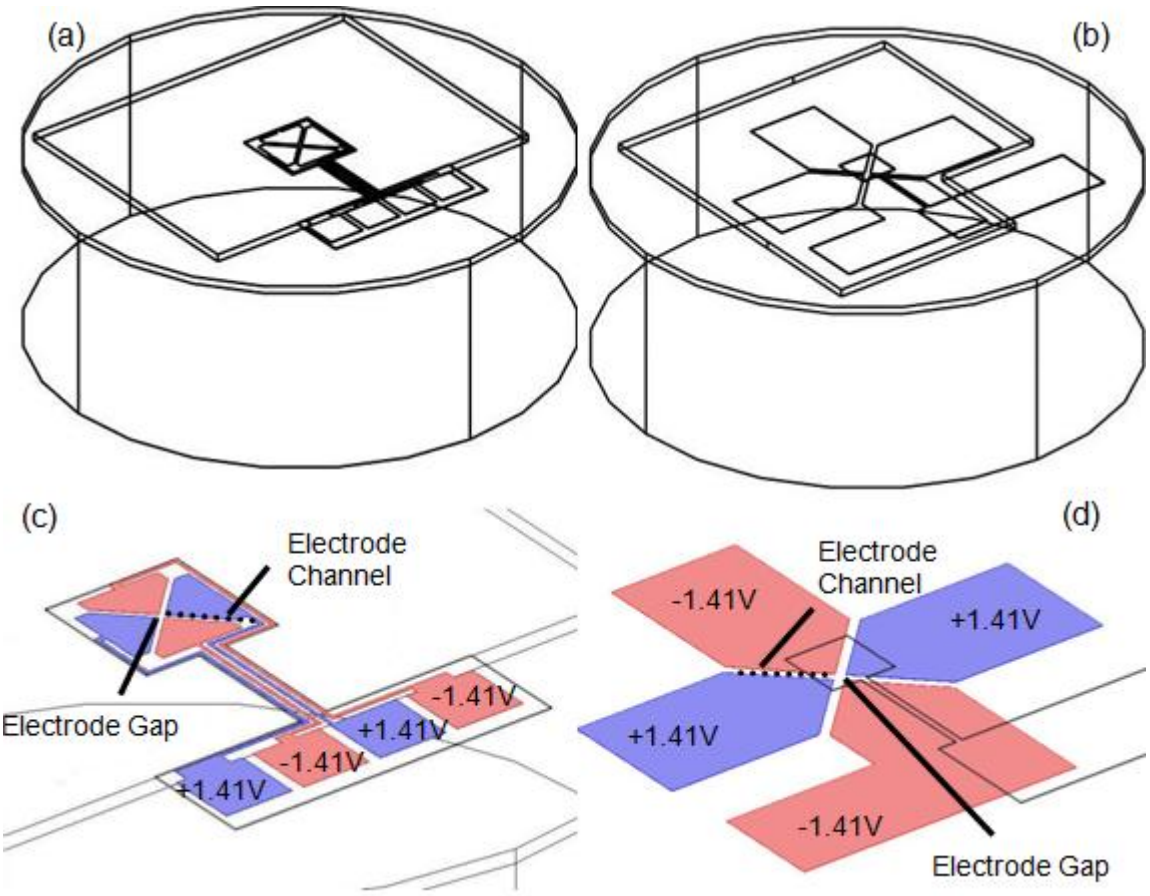

Figure 27: Wireframe models of the designs used in the COMSOL simulations. In both cases, a cantilever is suspended over a trench. (a) models the E/C configuration with the contact pads located at the fixed end of the cantilever beam. A close up of the cantilever and the electrodes is shown in (c) (b) models the C/E configuration. A close up of the cantilever beam and the electrodes is shown in (d). The V_{RMS} voltage is indicated and colour coded for both (c) and (d).

The design of the electrodes is similar to the triangular electrodes presented in the previous chapter which consists of long interelectrode gaps. Each electrode had an applied voltage of ±1.41 V_{RMS} (4 V_{PP}) to represent a sinusoidal wavelength 180 º out of phase to the adjacent electrode and in phase with opposite electrodes, as shown in Figure 27c and Figure 27d.

The design of the cantilever beams having electrodes on the cantilever surface (E/C) and electrodes underneath the cantilever (C/E) were generously provided by Dr. Y. J. Lai of Queen's University. Cantilever beams were 2 μm thick while electrodes were modeled as having a thickness of 200 nm. The cantilever in the E/C configuration, Figure 27a and Figure 27c, has a narrow section with a width of 40 μm and a length of 200 μm and a head 200 μm x 200 μm. The electrodes have a gap of 10 μm and are connected to contact plates along the cantilever. The cantilever in the C/E configuration, Figure 27b and Figure 27d, has a narrow section with a width of 10 μm and a length of 300 μm and a head 100 μm x 100 μm. The electrodes have a gap of 20 μm and are placed on the surface of the trench below the cantilever with contact pads located adjacent to each electrode.

4.1.2 Chip Fabrication

The cantilever devices were provided by Dr. Yongjun Lai of mechanical and material engineering department of Queen's University. The devices were fabricated using the user-customizable MicraGEM process (Micralyne, Canada) that is generically described in (Sigurdson *et al.*, 2005). The fabricated electromechanical devices in this study are 10 μm thick high electrical resistivity single-crystal silicon cantilevers with 200 nm thick gold electrodes deposited on its surface. The devices rest on a Pyrex substrate with 10 μm deep substrate etched channels over the free-standing regions of the microstructures.

4.1.3 Poly-L-Lysine Functionalization

The procedure of poly-l-lysine functionalization was adapted from literature to create a positively charged surface to electrostatically retain the target particles (Hoettges et al., 2003a).

4.1.4 Escherichia coli Preparation and Collection

The strain of *E. coli* (EMG 31) used in this research was donated by Dorothy Agnew from the department of Microbiology and Immunology at Queen's University. The *E. coli* was kept alive on Luria Bertani agar plates until needed. *E. coli* was killed via UV exposure over an 8 hour period and stained using a final concentration of 0.05 g/L of methylene blue. Samples were placed in a centrifuge at 5800 x g for 10 minutes, decanted, refilled with Millipore® filtered water and shaken vigorously; this process was repeated three times. The final concentrations were prepared by dilution with Millipore® water. Suspensions containing 10^8 *E. coli* particles/mL were used immediately after preparation. A 40 µL droplet of was placed on the cantilever chip. For all experiments collection times were 30 minutes after which the chips were thoroughly rinsed with Millipore® water and allowed to dry overnight.

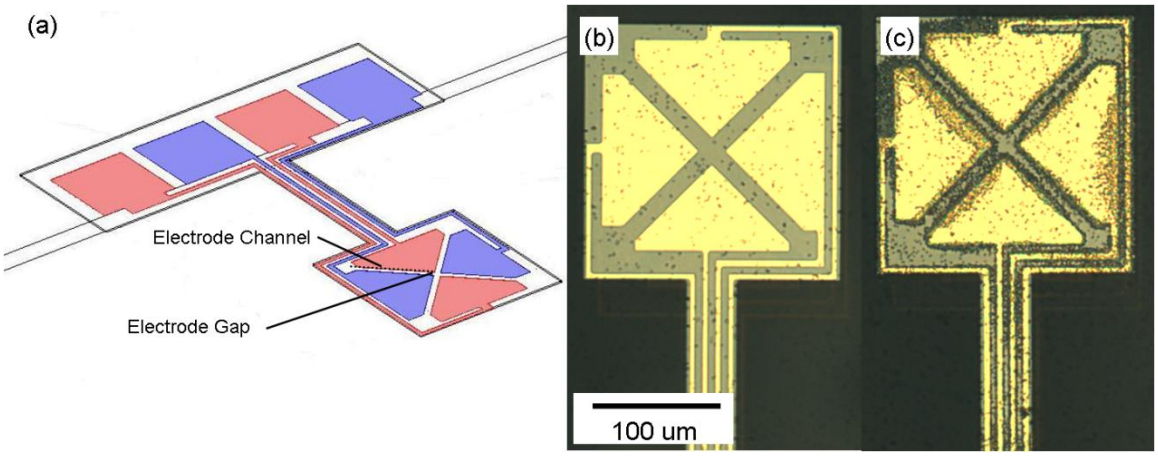

Figure 28: (a) Wireframe model of a cantilever where the microelectrodes having the same phase are colour coded for easier identification. Optical images of dried poly-L-lysine functionalized cantilevers after 30 minutes of exposure to 10^8 particles / mL of UV killed, MB stained *E. coli* with (b) unassisted capture and (c) dielectrophoretic capture (8 V_{pp}, 1 MHz).

4.1.4.1 Live Bacteria Preparation

Live *E. coli* was generously prepared to known concentrations by Dr. Stephen Brown's research group from Microbiology and Immunology at Queen's University. The bacteria were then centrifuged for 10 minutes at 7200 x g and the media was replaced with phosphate buffered water. This step was repeated once more. Suspensions containing 10^7 cfu/mL *E. coli* were used within 6 hours of preparation. A sample volume of 30 μL was used for each test. For all experiments, collection times were 30 minutes, after which, the chips were thoroughly rinsed with Millipore® water and allowed to dry overnight.

4.1.5 Dynamic Measurements

Dynamic measurements were performed by Jacky Chow of the mechanical and materials engineering department of Queen's University. Electrical potential (50 V_{pp}, 25 VDC) was applied between the cantilevers and a sharp tungsten probe in close proximity to electrostatically excite the microstructures, while the resonant frequencies of the structures were measured using a commercial MSA-400 vibrometer (Polytec, Germany). Resonant frequencies of the functionalized cantilevers were recorded before and after *E. coli* particle collection.

4.2 Numerical Analysis of the Effect of Electrode Placement

Work presented in the previous chapter analyzed how AC electrokinetics increased the flow rate from the bulk and fed towards the center gap of quadrupolar electrode designs. While the circular electrodes provided more paths for the particles to reach the electrode gap, the triangular electrodes had more intense fluid flows. In order to provide versatility in application, the triangular electrode designs were chosen since they allow for both negative dielectrophoresis (with the electric field gradient minima present in the gap) and positive dielectrophoresis due to

the longer microelectrode edge length. Furthermore, it was observed that the fluid flows from the bulk originated from directly above the electrode gap with both designs. In order to take advantage of this, two cantilever designs were proposed. The first design incorporated the electrode on the surface of the cantilever (E/C), as shown in Figure 27a and c. This design required the patterning of gold electrodes on the cantilever with long, thin gold contact wires connecting the contact pads to the electrodes. This design is more susceptible to damage since even a small scratch on one of the wires would sever the connection. The presence of gold on the surface of the cantilever also reduces the surface area of the silicon which is necessary for the surface functionalization described in section 3.1.3.

4.2.1 Electrode on Cantilever (E/C)

Figure 29 depicts plane A, the plane parallel to the length of the cantilever beam. From this viewing angle, in the center of Figure 29a the net force experienced by particles in the fluid is directed towards the edges of the electrode at three locations: the centre (location of the electrode gap), the edge of the cantilever (near a wire) and near the arm of the cantilever on the far right hand side (where the wires approach before diverging). These locations act as areas where particles are expected to concentrate since the force due to DEP is greater than that of Brownian motion or the Stokes drag force (Morgan and Green, 2003; Grom *et al.*, 2006). Outside of the immediate area, particles from the bulk are conveyed to the cantilever surface from both above and below the cantilever. Particles are able to collect from below the cantilever as well since the force due to buoyancy is negligible when compared to the dielectrophoretic force (Ramos *et al.*, 1998). Figure 29a indicates that the flow rates are high and result in a strong downward force felt by particles near the cantilever beam's arm. This occurs because the connecting wires run along the cantilever arm resulting in high electric gradients. It is also where the highest fluid velocity

occurs in this plane with a maximum predicted speed of 35.9 μm/s. In Figure 30a, the E/C electrode similarly has three expected concentration areas points, the tips of the electrodes located at either side of the electrode gap and two points the corners of the cantilever beam. Once again, these areas exist because of the necessity of the wire connections between the electrodes and the contact pads. Figure 30 also presents the strongest fluid flows in the entire system with the maximum velocity of E/C being 49.6 μm/s.

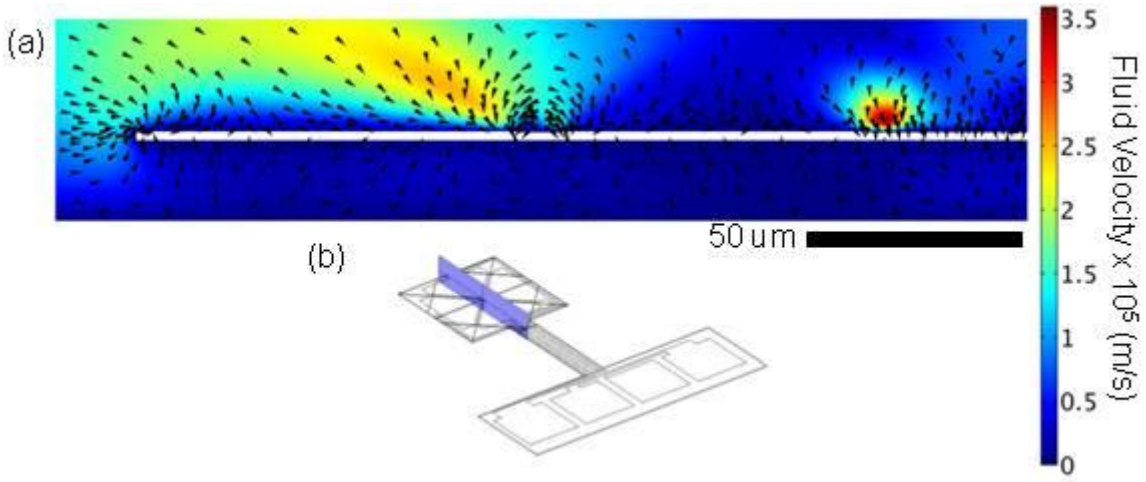

Figure 29: Normalized arrow plots of plane A for the E/C design indicating the direction of the net forces for a suspended particle. For all areas outside of the electrode gap, the dominant force is the fluid drag force. Background colour indicates the magnitude of the fluid velocity and blank areas indicate the location of the cantilever beam. (a) Visualization plane A, as indicated in (b).

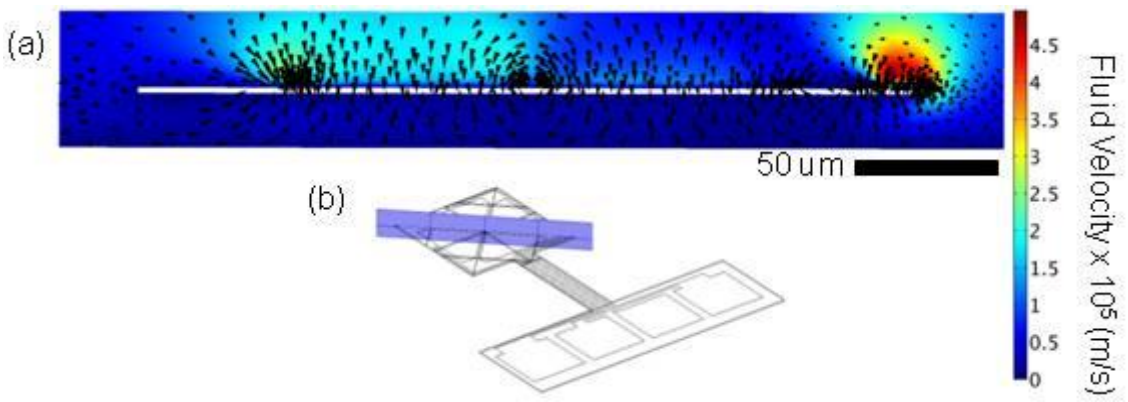

Figure 30: Normalized arrow plots of plane B for the E/C design indicating the direction of the net forces for a suspended particle. For all areas outside of the electrode gap, the dominant force is the fluid drag force. Background colour indicates the magnitude of the fluid velocity and blank areas indicate the location of the cantilever beam. (a) Visualization of plane B, as indicated in (b).

The final plane investigated for the electrode on the cantilever (E/C) design is plane C. As shown in Figure 31, plane C is an area perpendicular to the electrode channel, similar to Figure 13a from section 3.1.2. In contrast to the previous section, the fluid medium undergoing positive DEP does not present as a rolling pattern on either side of the electrode. In Figure 31 the area above the cantilever is more chaotic due to the close proximity of the wires which join the electrodes to the contact pads and produces flows directing particles towards the electrode edges. Once again, the wires along the edge of the cantilever would be areas where particles could accumulate, in addition to the centre of the electrode design. These areas may be beneficial since a cantilever uses a mass based method of detection. As long as the particles are collected away from a node in the characteristic vibration being tested, they would increase the sensitivity of the system. For the E/C design, the maximum velocity calculated in plane C is 40.5 μm/s.

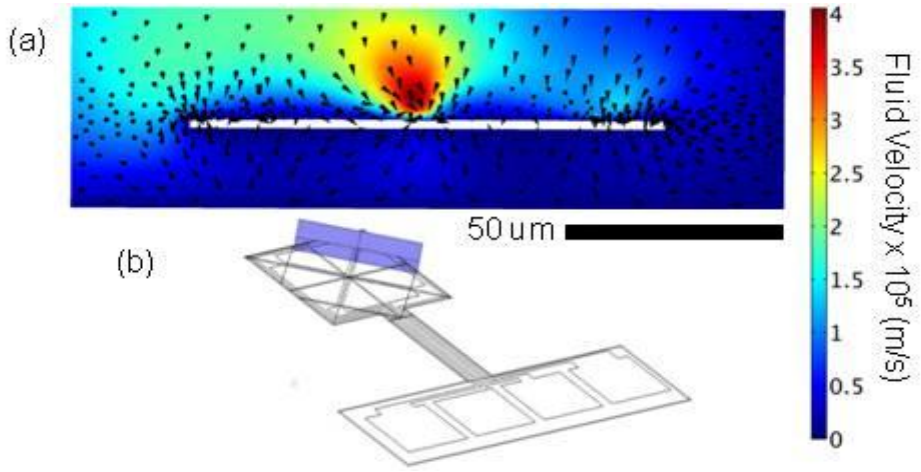

Figure 31: Normalized arrow plots of plane C for the E/C design indicating the direction of the net forces for a suspended particle. For all areas outside of the electrode gap, the dominant force is the fluid drag force. Background colour indicates the magnitude of the fluid velocity and blank areas indicate the location of the cantilever beam. (a) Visualization plane C, as indicated in (b).

4.2.2 Cantilever over Electrodes (C/E)

As an alternative to the E/C design, a second design was proposed where the cantilever was placed above a set of triangular electrodes (C/E), Figure 27d. This design is more robust and would attempt to take advantage of the flow from the bulk that was observed in Chapter 3. It was postulated that since the fluid flow from the bulk originates from directly above the electrode gap, a cantilever placed above the electrode gap would intercept any entrained particles travelling towards the electrode. Furthermore, the absence of any gold on the cantilever would maximize the functionalized surface area for collection.

Figure 32a, representing the C/E design, shows fluid velocity as indicated by the intensity of the colour plot. These fluid velocities are not as intense as the previous design and reach a maximum predicted velocity of 8.6 μm/s. The most intense velocities do not occur above the

cantilever as was expected and tend to be directed along or around the edge of the cantilever surfaces which suggest that the presence of the cantilever causes enough of a disruption that the fluid flow from the bulk would not encourage the deposition of particles on the cantilever.

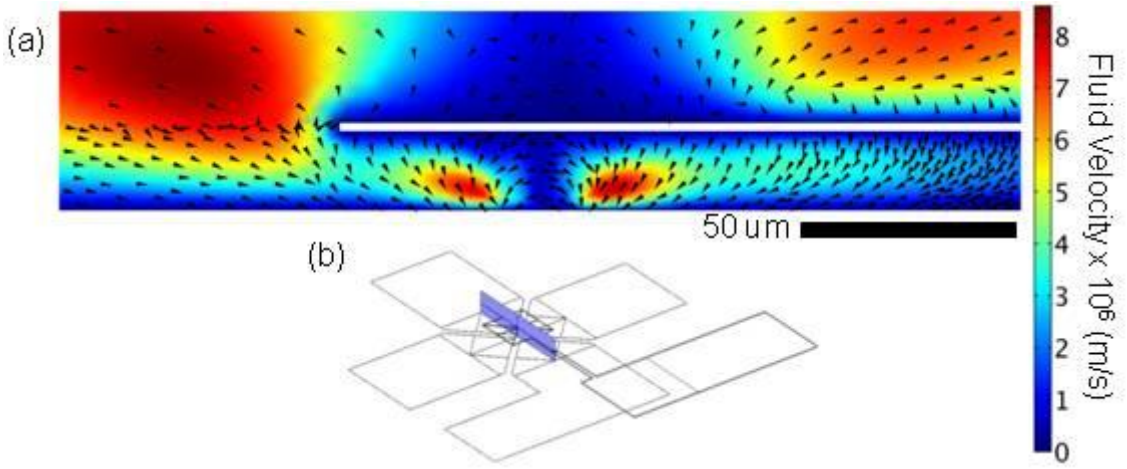

Figure 32: Normalized arrow plots of plane A for the C/E design indicating the direction of the net forces for a suspended particle. For all areas outside of the electrode gap, the dominant force is the fluid drag force. Background colour indicates the magnitude of the fluid velocity and blank areas indicate the location of the cantilever beam. (a) Visualization plane A, as indicated in (b), showing collection in the center of the electrode gap.

The lack of flows directed to the surface of the C/E design is further illustrated in Figure 33 which depicts Plane B, which is parallel to the electrode channel. The direction of the net forces on a suspended particle from the bulk would travel around the cantilever beam to be fed towards the electrode edges. The direction of the force arrows close to the cantilever suggests that any particles approaching the edge would be pushed away, thus resulting in limited or a complete lack of collection of particles anywhere on the cantilever surface.

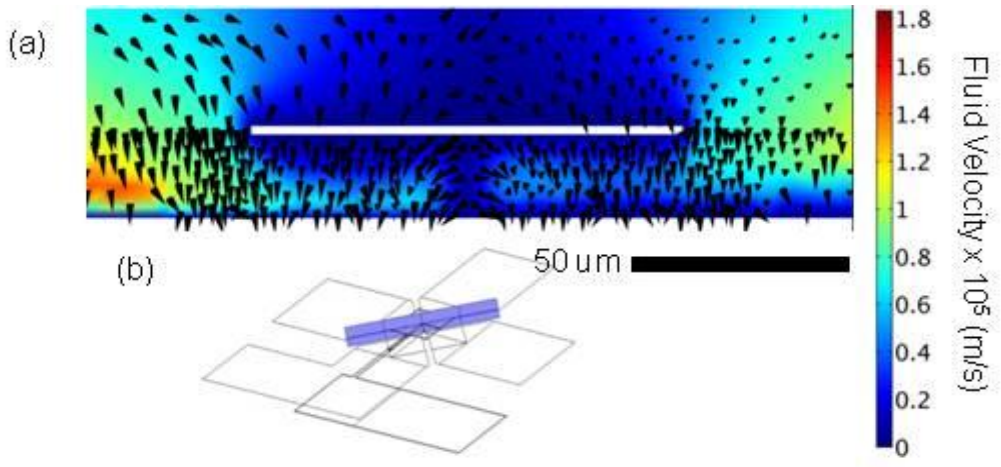

Figure 33: Normalized arrow plots of plane B for the C/E design indicating the direction of the net forces for a suspended particle. For all areas outside of the electrode gap, the dominant force is the fluid drag force. Background colour indicates the magnitude of the fluid velocity having a scale bar in $\log_{10}$(m/s). Blank areas indicate the location of the cantilever beam. (a) Visualization plane B, as indicated in (b).

Figure 34 provides a view for the C/E design which is perpendicular to the electrode channel yet, away from the cantilever. This area away from the cantilever would collect particles at the electrode edges (centre of the image) from the bulk and thus prevent them from being collected on the cantilever surface. Furthermore, the maximum velocities observed for the C/E design occur in this plane. The maximum fluid velocity observed for the C/E design is 20.6 μm/s. This suggests that the cantilever may hinder the electrothermal flows and reduce the volume throughput of the device.

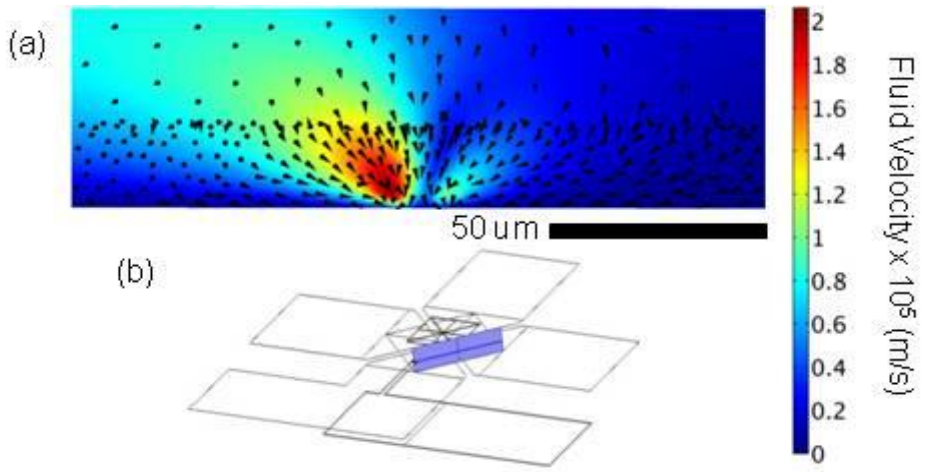

Figure 34: Normalized arrow plots of plane C for the C/E design indicating the direction of the net forces for a suspended particle. For all areas outside of the electrode gap, the dominant force is the fluid drag force. Background colour indicates the magnitude of the fluid velocity and blank areas indicate the location of the cantilever beam. (a) Visualization plane C, as indicated in (b).

4.2.3 Temperature Profiles

Figure 35 presents the temperature profiles of each cantilever design. Numerical simulations predict a temperature increase of 11.7 K for E/C and 5.5 K for C/E due to Joule heating. Coulombic forces act on the resulting conductivity gradients driving the fluid from low to high areas of conductivity (low to high temperature areas) (Ramos *et al.*, 1998). Both temperature increases are greater than the reported results in Chapter 3. In comparison with Chapter 3 one key difference is that a more insulating material, borosilicate, is being used as the substrate instead of the silicon that was previously modeled and, therefore, more of the heat generated is dissipating into the liquid. Secondly, the E/C designs are suspended over a thin cantilever beam rather than being in direct contact with the substrate, resulting in the heat being almost entirely dissipated to the surrounding fluid and higher realized temperatures. Despite these

increases, the maximum temperature reached for both designs is well within the range for biological particles which are viable between 20-40 ℃.

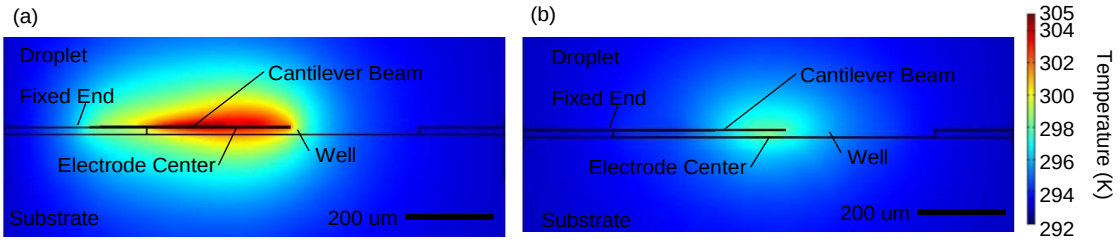

Figure 35: Cross-sectional temperature profile plots of the wireframe models in the same direction as Plane A in Figure 29 and Figure 32. The locales of various areas of interest are identified (a) presents the E/C configuration reaching a maximum temperature of 304.7 K centered on the electrode center and having a decreasing temperature extending outwards in a deformed teardrop shape. (b) presents the C/E configuration reaching a maximum temperature of 298.5 K at the electrode center with decreasing temperature extending outwards in a roughly spherical shape.

The maximum velocities observed in this model are smaller than those presented in the previous chapter, despite the similar electrode designs. The maximum velocity of a fluid undergoing electrothermal flow is proportional to ΔT, which is a function of solution conductivity, and the inverse of the characteristic length (Ramos *et al.,* 1998). Furthermore, for electrothermal flows where $\omega\varepsilon/\sigma << 1$ (angular frequency – ω, medium permittivity – ε, medium conductivity – σ), as in the case of Chapter 2, the velocity is approximately ten times faster than electrothermal flows where $\omega\varepsilon/\sigma >> 1$, as in the case of these cantilever simulations (Castellanos *et al.*, 2003). Using these factors, it would be expected that the maximum fluid velocities observed for the E/C design should be approximately 50 times smaller than those from the previous chapter. When comparing the E/C and C/E designs, the maximum fluid velocity

generated from electrothermal flow is proportional to the change in temperature (the rise in temperature for E/C is twice that of C/E), and inversely proportional to the characteristic length of the electrode (the characteristic length for E/C is half that of C/E), as shown in equation 19 (maximum fluid velocity - u_{max}, fluid permittivity – ε, fluid conductivity – σ, Voltage – V, thermal conductivity – k. fluid viscosity – η, characteristic electrode length – l).

$$u_{max} \cong 2.5 \cdot 10^{-4} \frac{\epsilon \sigma V^4}{k \eta l} \left| \frac{1}{\varepsilon} \frac{\delta \varepsilon}{\delta T} \right| \quad (19)$$

Therefore, the observed velocities for the E/C designs are expected to be approximately 4 times larger than those of the C/E designs. (Castellanos *et al.*, 2003). Based on the planes examined, the simulations found that the E/C designs are on average 3 times larger than the C/E designs.

4.2.4 Sensitivity and Resonant Frequency Analysis

The increased complexity of a model with a moving boundary to simulate the movement of the cantilever beam proved to be too computationally intensive and, hence, calculations of resonant frequency in solution and steady state deflection of the cantilever during the application of an AC electric field were not performed in COMSOL. Due to the symmetry of the results in the previous section, the electrode geometries investigated can be simplified into one-half model representations reducing the model complexity. Once these models are realized they can be compared to work previously explored. In order to provide a rationale for the feasibility of these cantilevers as potential biosensors, the large tip of the E/C cantilever beam can be modeled as an equivalent volume cantilever having the same thickness and length as one with a simple rectangular geometry with dimensions of 400 μm x 120 μm x 2 μm (LxWxD) (equivalent volume to 96,000 μm^3). The resonant frequency of such a cantilever beam in water should be approximately 39 kHz (Sader, 1998). Furthermore, with this predicted resonant frequency, Illic *et*

al. (2004) illustrated how equation 20 can be used to determine the minimum measurable change in mass from a change in resonant frequency (mass – m, spring constant – k, frequency – *f*).

$$\Delta m = k_s \left[\frac{1}{(f-\Delta f)^2} - \frac{1}{f^2} \right] \tag{20}$$

Assuming a detectable change in resonant frequency of 1% (~400 Hz), the minimum mass that must be deposited on the cantilever beam is on the order of 68 pg. Using an *E. coli* bacterium as an example with an approximate weight of 0.7 pg (Ilic *et al.*, 2004), positive detection could occur with the collection of 98 bacteria particles. In the previous chapter, it was shown that using negative dielectrophoresis, particle densities up to 8.4 particles per μm^2 within the electrode gap (maximum 840 particles in a 100 um^2 electrode gap seen in E/C configuration) were achievable in 20 minutes. However, in order to provide proof of principle, experimental work will take advantage of positive dielectrophoresis. Due to the possible ranges of the Clausius-Mossotti factor, the maximum magnitude of the realizable DEP force with positive DEP can be twice that of negative DEP. Furthermore, based on the simulations presented earlier in the chapter, particle should collect along the electrode edges, which because of the presence of connecting wires for the E/C design, provides an increased collection area.

4.3 Cantilever Based Collection and Detection

To test the ability of quadrupolar microelectrodes to cause enhanced bioparticle collection in solution, two scenarios were investigated: unassisted collection and collection in the presence of an electric field. For unassisted collection, suspensions of 10^8 *E. coli* particles/mL were allowed to settle over a 30 minute period on a poly-L-lysine functionalized cantilever design. Any particles present on the surface after that time would be due to stochastic movement

and gravitational effects. The resulting sedimentation pattern is presented in Figure 28b. The location of *E. coli* on the surface of the cantilever appear to be random, as expected with relatively few particles being retained when compared to the collection in the presence of an applied electric potential (8 Vpp, 1 MHz) with the same concentrations and length of time for collection, as shown in Figure 28c. Experimental observation during and after collection validate the numerical simulations from section 4.2.1. The collection patterns in Figure 28c can be identified using the numerical simulation planes. From Figure 29, collection is observed both around the electrode centre, at the top end of the cantilever and along the cantilever arm. From Figure 30, significant collection is observed at both the top left and bottom right corners of the cantilever head. Finally, from Figure 31, particles are observed to collect along the electrode channel and along the wires that pass around the edge of the cantilever. These collection patterns are characteristic of particles undergoing "positive" dielectrophoresis (Hoettges et al., 2003a). The densest observed layer of *E. coli* collection occurs at the top left of the cantilever, an area devoid of wires. Since the highest fluid velocities occur near the electrode edges, the absence of wires in this region would allow particles more time to adhere to the surface of the cantilever and remain after washing. The bacteria on the surface of the cantilever remain attached due to the electrostatic forces between the former and the (positively charged) poly-L-lysine layer, thus resulting in a net mass increase of the cantilever system.

The effects of poly-L-lysine functionalization on the resonant frequency of the cantilevers were examined in over 100 cases for a variety of different cantilever paddle designs for all 5 resonant modes (results not shown). A typical sample of the resonance frequency data is presented in Figure 36 with each resonant mode identified. A resonant mode is identified as an oscillation of the cantilever beam with amplitude that is much greater than the baseline.

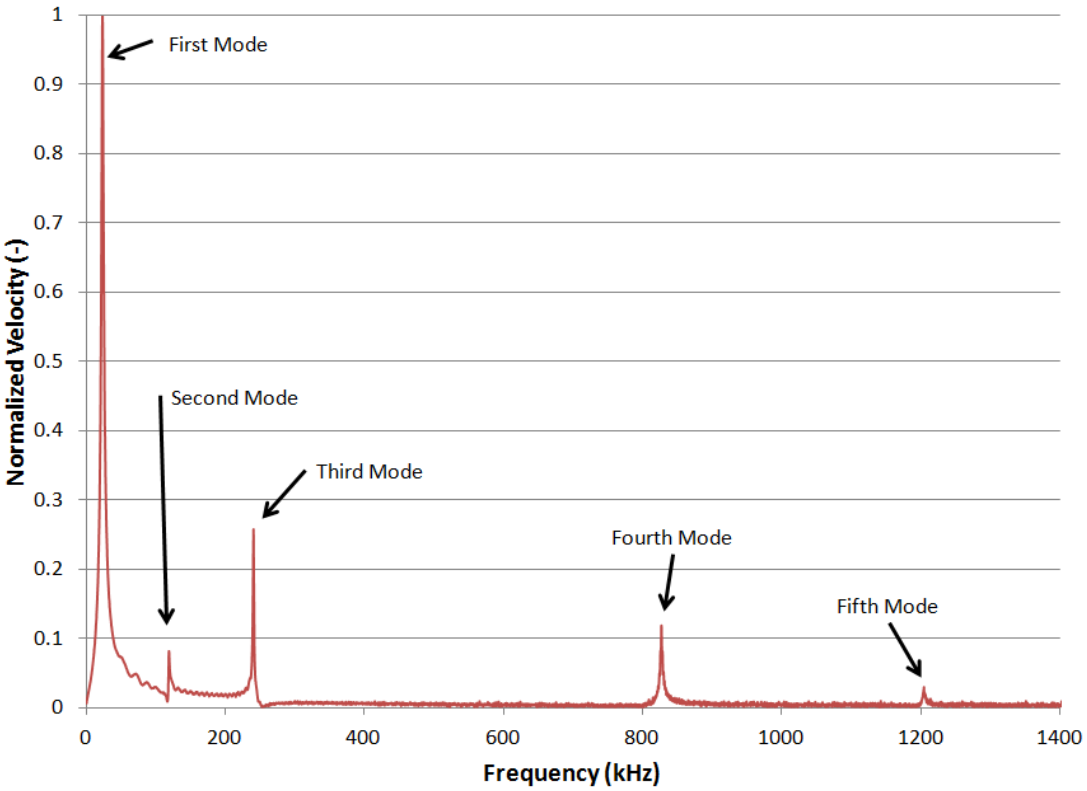

Figure 36: Identifying resonant modes of a typical cantilever beam. Data is presented as the normalized velocity of the beam as a function of the frequency of the applied voltage for a single point on the beam's surface. The data shown is prior to the collection of bacteria. Due to the magnitude of the shift after particle collection the shifted data would appear to overlap the original at this scale.

Cantilevers were observed to have experienced negligible changes in the resonant frequency due to functionalization and it was hypothesized that functionalization had a negligible effect on the resonant frequency of a cantilever. Furthermore, cantilevers coated with poly-L-lysine and exposed to an electric field for 30 minutes in Millipore® filtered water did not show a change in their resonant frequency.

Presented in Figure 37 are the resonant frequency shift results of the cantilever shown in Figure 28b and c. The cantilever from Figure 28b, having particles on its surface due to unassisted deposition, experienced no measurable resonant frequency shift for the first four flexural modes. For the fifth flexural mode, a negative shift of over 600 Hz was recorded. Similarly, the cantilever from Figure 28c, with dielectrophoretically captured particles on its surface, had no measurable resonant frequency shift for the first flexural mode. However, AC electrokinetically assisted capture resulted in the second, third and fourth flexural modes recording a negative frequency shift of over 300 Hz. In the fifth flexural mode, the recorded frequency shift was nearly three times that of the cantilever which relied on passive particle deposition methods.

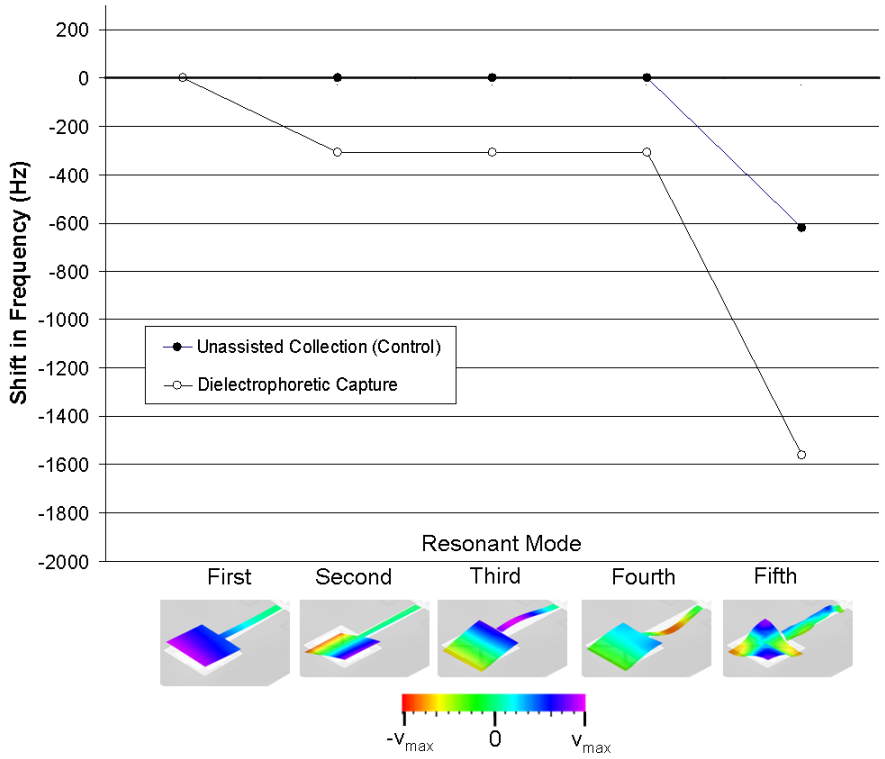

Figure 37: Frequency shift (frequency after particle collection minus frequency prior to particle collection) vs. resonant mode after 30 minutes of collecting 10^8 particles / mL of UV killed, MB stained *E. coli* for a single cantilever design. Dielectrophoretic capture (8 Vpp, 1 MHz) and unassisted collection are presented from a scan with a bandwidth of 2 MHz. For the first resonant mode the shift is 0 Hz for both data series. The inserts show the five measured resonant modes from an isometric view with colour intensity indicating velocity.

The collective results for the changes in resonant frequency in the five measurable modes over 6 tests are presented in Figure 38. The cantilevers used have similar geometry, although their beam length varies from 100 to 300 μm. In order to examine the effects of using an applied electric potential, Figure 38 compares the change in resonant frequency for cantilevers which dielectrophoretically captured bacteria versus the unassisted capture of the control group. For

cantilevers relying on unassisted deposition, a 0 Hz shift lies within one standard deviation of the mean shift measured for the first four modes and the fifth mode having a mean shift of 450 Hz. In comparison, cantilevers which had a voltage applied across the microelectrodes did not include a 0 Hz shift within one standard deviation for the third, fourth and fifth modes. The fifth resonant mode shows a threefold increase in the magnitude of the mean shift in comparison to relying on unassisted deposition. The presence of large standard deviations is attributed to the limited number of runs and would improve with subsequent testing. However, the use of quadrupolar microelectrodes on cantilevers to enhance the collection of particles is proven to be a promising detection scheme. For all modes measured, the use of an electric field to enhance the collection of particles resulted in a greater negative resonant frequency shifts than when relying on unassisted collection. A gradual increase in the resonant frequency shift is observed for the five vibration modes for dielectrophoretically captured bacteria. This suggests that the detection of particles at lower resonant modes may be possible and that the higher modes are more sensitive to changes in mass. For the fifth resonant mode, both collection methods were observed to have an increase in the magnitude of the shift, the largest belonging to the cantilever using dielectrophoretic capture. As contrasted in Figure 28b and c, the number of particles captured through the use of an electric field is substantial. The sensitivity of a cantilever is subject to the location of the random deposition or particles and may be unresponsive if particles accumulate in a node, or may be particularly sensitive if particles accumulate in an area of maximum displacement. This variability in sensing can be minimized with the use of properly placed microelectrodes that can attract particles to locations where one would expect to have displacement maxima and avoiding resonant nodes.

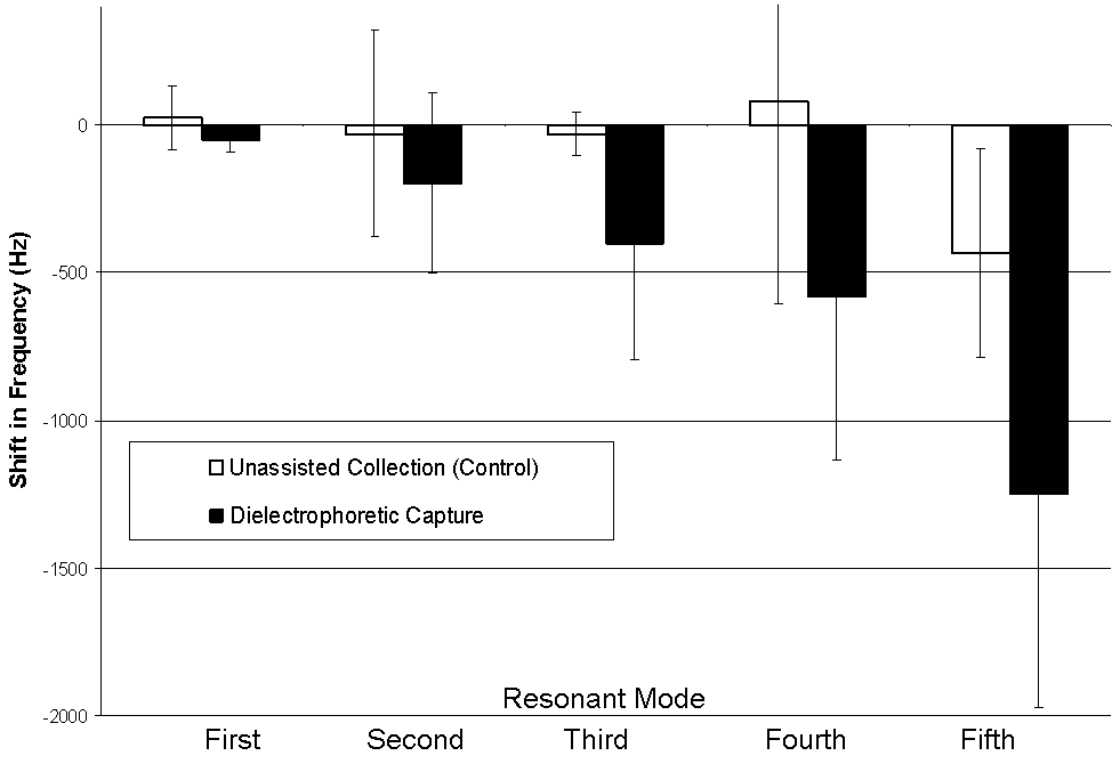

Figure 38: Frequency shift (frequency after particle collection minus frequency prior to particle collection) vs. resonant mode after capture of 10^8 particles / mL of UV killed, MB stained *E. coli* after 30 minutes with an AC applied voltage of 8 Vpp with a frequency of 1 MHz. Shifts are presented using the smallest scanning range able to capture the mode being investigated. Error bars indicate one standard deviation.

4.3.1 Antibody Functionalized Cantilevers

Initial attempts to create a selective surface with antibodies involved the electrode on cantilever (E/C) designs presented in this chapter. The functionalization method used was the same as that shown in section 3.1.3 with the antibody anti-*E. coli*, used as received from Cedarlane (Ontario, product code #1001). During functionalization, it was observed that the cantilever structures are fragile and can be easily damaged or destroyed by the chemicals

employed. The gold wires and contact pads present on the cantilever are particularly sensitive. Multiple steps in the functionalization procedure resulted in the partial or total destruction of the contact wires. It was further observed that certain cantilevers were able to withstand the functionalization procedure to a greater degree than others, suggesting variability in the Micralyne process. Specifically, if the contact pads were easily scratched by a probe, the wires would be more likely to fail during functionalization. Given the high attrition rate of antibody functionalization with these designs, the results presented in this section have not yet been repeated.

In the previous section, UV light killed bacteria were used in order that experiments could be conducted in non-biohazardous laboratory conditions. The detection of a pathogen, *i.e.* live *E. coli* bacteria, through the use of an antibody functionalized cantilever would permit for the selective detection of pathogens in heterogeneous solutions and more closely mimic real world conditions. Figure 39 shows the collection of *E. coli* bacteria with a functionalized cantilever. The right hand side of Figure 39 shows collection after 30 minutes using positive dielectrophoresis. The left hand side of Figure 39 is a similarly functionalized cantilever without an applied electric field. The shaded nature of the cantilever on the right hand side is due to the volume around the beam being almost completely filled with *E. coli* bacteria. Areas with lower concentrations of *E. coli* are visible above the centre of the electrodes as evidenced by the lighter areas. This is consistent with collection using positive dielectrophoresis since bacteria would tend to accumulate starting at the electrode edges extending outward.

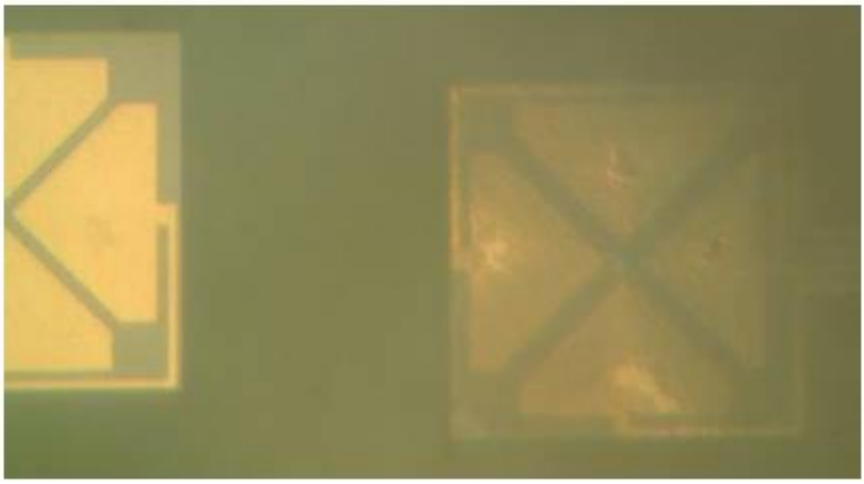

Figure 39: Anti-*E. coli* functionalized cantilever collecting live *E. coli* bacteria from a 10^7 cfu/mL sample after 30 minutes with an AC electric field of 8 V_{pp} and 1 MHz (right) adjacent to another cantilever in the same suspension without an AC electric field (left).

After washing, an example of the amount of collected *E. coli* is presented in Figure 40. In comparison with Figure 28c, the observed surface covered by *E. coli* appears to be less. Based on the typical coverage observed with positive DEP, such as in Figure 39, an anti-body active surface should be retaining more bacteria. The anti-body used for functionalization was an antibody for a range of *E. coli* strains and may be exhibiting reduced specificity for the *E. coli* specific strain used here. With the degree of coverage shown in Figure 39 there remains potential to improve the collection and enhance the performance of these cantilevers for use as selective biosensors.

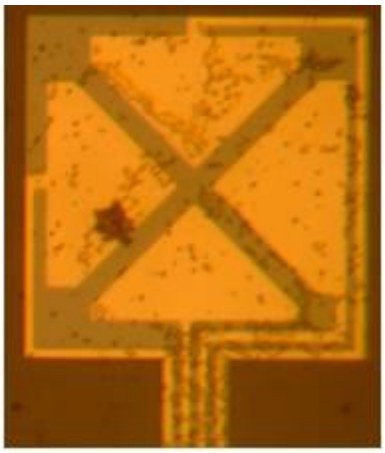

Figure 40: Anti-*E. coli* functionalized cantilever after having collecting live *E. coli* bacteria and washed in phosphate buffered saline and filtered water.

4.4 Conclusions

3-D COMSOL simulations of potential biosensor designs containing a sensing cantilever beam coupled with a quadrupolar electrode designed to enhance bioparticles collection via dielectrophoresis (DEP) were successfully realized. It was determined that placing the cantilever above the electrodes (C/E) resulted in impeding flow from the bulk. With the electrodes on the surface of the cantilever (E/C) the presence of the connecting wires provided multiple locations for secondary collections.

Experimental results of the coupled electro-mechanical biosensor featuring a quadrupolar microelectrode array embedded into a cantilever beam have provided evidence that such a biosensor prototype can successfully integrate accelerated bioparticle capture from solution with signal transduction. Cantilevers with embedded microelectrodes have been tested and shown to enhance the collection of *E. coli* from solution by means of AC dielectrophoresis. Within 30

minutes, dielectrophoretically assisted bioparticle deposition resulted in a doubling of the shift in resonant frequency for the highest resonant mode measured with respect to unassisted collection. This is a significant difference in identification time as the system detailed in section 2.3.2.2 by Park *et al.* (2008) required several days for cells to grow prior to their successful detection. Finally, these designs have demonstrated that they can be functionalized with antibodies in order to provide a selective surface for bacteria detection. While poly-L-lysine is often used to provide a functional surface capable of retaining bioparticles (Park *et al.*, 2008, Tomkins *et al.*, 2011) or drying the device to retain captured particles (Gupta *et al.*, 2004), these methods do not have the potential for identification of target bioparticles from heterogeneous mixtures. However, due to the sensitivity of the wires and the effects of the functionalization procedure, the degree of bacteria collection with the current method has not yet reached the point where it produces a shift in the resonant frequency.

In light of the fact that these measurements were performed under not-yet-optimised experimental conditions, the results are encouraging. In conjunction with Dr. Yongjun Lai and Jacky Chow, the present effort of our groups is directed towards the optimization of a selective functionalized layer and the improvement of beam and wire geometry.

Chapter 5 AC electrokinetically enhanced collection of viruses integrated with Raman based detection

Raman spectroscopy has the potential to act as a "fingerprinting" technique for the identification of pathogens (Cheng *et al.*, 2007). The resulting spectrograph can be used to identify a target pathogen based on its unique chemical bonds without the need of further reagents. Depending on the needed resolution and size of the area to be scanned, the timeframe for Raman spectroscopy can increase exponentially. However, if the target pathogen is concentrated at a specific location, Raman spectroscopy can render a high resolution scan over a small area in a short time frame. Raman systems currently have the capability to provide detection of samples both *in situ* and *ex situ* as well as the ability to perform confocal microscopy without the need for a labeling molecule ("label free"). The envisioned experimental scheme is presented in Figure 41. A miniaturized sensor employing AC electrokinetics will force the target pathogen, in this case a phage, to a specific location on the substrate surface. The surface will be functionalized with a selective antibody allowing for the retention of the phage after the electric field is turned off. This sensor will then be scanned with a Raman spectroscope with the laser targeting the expected collection point. The resulting shift will then enable the fingerprinting of the pathogen. Once the proof of principle has been demonstrated, this setup could then be modified to incorporate continuous flow systems or heterogeneous samples.

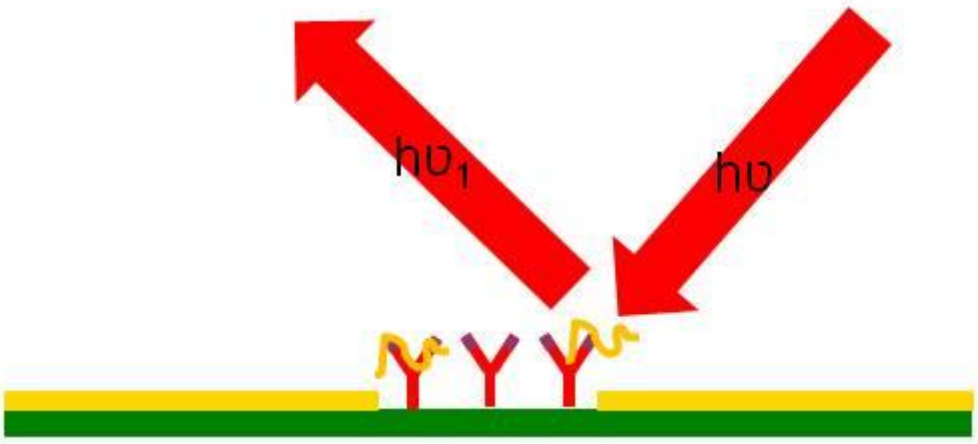

Figure 41: Proposed scheme for Raman spectroscopy coupled with an AC electrokinetically enhanced surface based biosensor. Gold microelectrodes (yellow) on an antibody (red "Y" shaped molecules) functionalized silicon substrate (green) with positive dielectrophoretically attracted viruses (orange wavy lines). A laser with a known energy (hυ) is directed towards an area containing viruses and the resulting Raman spectrum of the shifted light ($h\upsilon_1$) is recorded.

5.1 Materials and Methods

Unless otherwise specified, all chemicals were supplied by Sigma-Aldrich (MO).

5.1.1 Microelectrode Fabrication and Functionalization

The functionalization procedure was the same as described in section 3.1.3 except that the antibody used was anti-fd bacteriophage, used as provided (Cedarlane, Ontario, product number #1001).

Microelectrodes were fabricated in Queen's Micro- and Nano-fabrication facility in Jackson Hall (QFAB). Polished silicon waters with a diameter of 4 inches and a SiO_2 layer 0.5 μm thick were purchased from University Wafer (Massachusetts, USA). Wafers were cleaned with, in order, filtered water, acetone, propanol, filtered water, blown dry with nitrogen and then

heated to 120℃ for 10 minutes. It is necessary to clean acetone with propanol afterwards; otherwise the acetone leaves a residue that will not dissolve in water. The negative photoresist, ma-N 1405 (Microresist Technologies, Germany), was applied during a 6 second 600 rpm spin and then spun for 3000 rpm for 30 seconds. Excess photoresist was cleaned and the wafer was placed on a mask aligner. A chrome plated borosilicate plate containing the negative image of the microelectrode design was placed on the wafer in order to perform contact photolithography. The photoresist was exposed to 12 seconds of UV light and developed in ma-D 533S (Microresist Technologies, Germany). A typical pattern is presented in Figure 42. The presence of crazes in the photoresist indicated that the exposure time was too long and the wafer had to be cleaned with remover mr-Rem 660 (Microresist Technologies, Germany) and re-patterned. In Figure 42, the tips of the electrode are not well resolved. Close examination of the tips indicate that any resulting electrodes formed from these patterns would exhibit an irregular shape. Rather than having a single point at the tip of the electrode, ("u" shaped), at notch is formed at the very tip creating a double tip ("w" shaped). This creates significant difficulties when attempting to realize features on the order of less than 5 μm. However, the careful monitoring of UV exposure time and development time can assist in mitigating this effect.

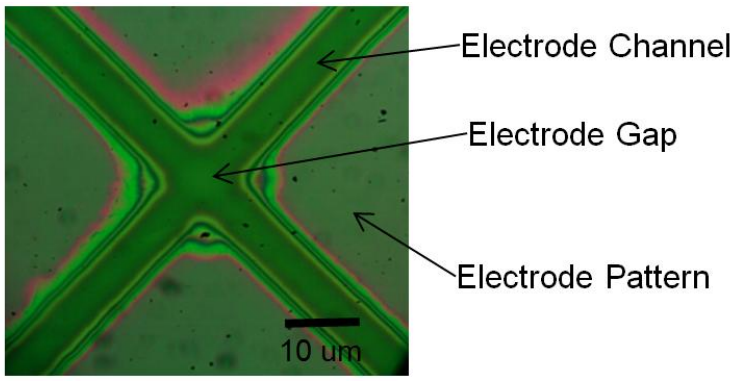

Figure 42: Light microscope image of a ma-N 1405 photoresist pattern of a triangular electrode with a gap spacing of 10 μm produced in the QFAB facility at Queen's University.

After patterning, wafers were transferred to a thermal evaporation unit which deposited 5 nm of chrome to improve bonding to the SiO_2 layer followed by 100 nm of gold. Gold lift off was accomplished by submerging the wafer in acetone in an evaporation dish and sonicating gently for ~45 seconds. A sacrificial layer of photoresist was applied to the wafer surface prior to dicing in order to more easily remove any silicon dust. The individual microelectrodes were diced using DAD 321 disco automatic dicing saw. The wafer was stuck to a glass substrate using wax. Cuts were made 440 μm deep in to the wafer at a cutting speed of 3 mm/s and a lowering speed of 0.03 mm/s. Water flow was kept at 0.1-0.2 L/min to prevent the overheating of the saw. Once the wafer was removed from the glass substrate, microelectrodes were snapped apart by hand and cleaned in acetone to remove the sacrificial layer of photoresist. The tip-to-tip separation of the electrodes used in this section is approximately 4 μm with the triangular electrode design.

5.1.2 M13 Phage

Dried samples of M13 phage particles (ATCC# 15669-B1) were purchased from Cedarlane (Ontario).

5.1.2.1 M13 Phage Preparation

Samples with known concentrations of M13 phage studied in this work were generously grown by Mrs. Dorothy Agnew of the Microbiology and Immunology department of Queen's University. The following is a brief summary of the procedure adopted by Mrs. Agnew. The M13 phage was re-suspended with 1 mL of Yeast-Tryptone broth. Yeast-Tryptone broth contains: 3 L water, 24 g tryptone, 15 g yeast extract, 15 g NaCl and has its pH adjusted to 7.5. In order to propagate the M13 phage, *Escherichia coli* EMG31 was prepared on nutrient deficient M9 plates. M9 plates are prepared with 800 mL of water, 18 g of agar, 10 mL of 10 mM $CaCl_2$, 1 mL 1 M $MgS0_4 \cdot 7H_20$, 10 mL 20% glucose, 1 mL 1% Thiamine HCl and 200mL of M9 salt solution (1 L water, 5.0 g NH_4Cl, 2.5 g NaCl, 15 g KH_2PO_3, 64 g $Na_2HPO_4 \cdot 7H_2O$). The *E. coli* EMG31 is then transferred to 26 mL of Yeast-Tryptone broth and allowed to reach the log growth phase. 200 μL of log growth *E. coli* EMG31 is then transferred into 20 mL of yeast tryptone broth with 10 μL of the re-suspended M13 phage. After 1.5 hours, the 20 mL was separated into centrifuge safe sample holders each containing 2 mL of the solution. After a further 6 hours, the samples are centrifuged and decanted. The resulting samples have an approximate concentration of 10^{12} pfu/mL and were stored at 4 ℃ until needed.

5.1.2.2 M13 Phage Identification

In order to visually identify the presence or absence of M13 phage on a silicon surface, the following procedure was used. After the application of the electric field, the microelectrodes were washed in phosphate buffered saline (PBS) for 30 minutes. The microelectrodes were then rinsed in PBS and allowed to react overnight in a 5 mL solution of PBS with 25 μL of biotinylated anti-fd, used as received (product number B2661). The microelectrodes were then rinsed with PBS and washed in PBS for 30 minutes while being gently shaken. The

microelectrodes were then placed in a 5 mL solution of PBS with 25 μL of ExtrAvidin-Cy3, used as received. Finally, the microelectrodes were rinsed with PBS, then washed in PBS for 30 minutes, rinsed in millipore filtered water and then washed in millipore filtered water for 30 minutes. Observations and Raman spectra were obtained after allowing the sample to air dry in a loosely closed container with a low-lint tissue.

5.1.3 Raman Spectroscope

Raman signals were acquired using a LabRAM (Horiba / Jobin Yvon) with an Olympus BX41 microscope and a HeNe laser source (632 nm). The data were collected and processed using the accompanying software, Labspec v. 4.14-01 (Horiba / Jobin Yvon). Individual scans were taken using exposure times of 15-120 s, between 15-30 repeats, pinhole sizes of 300 μm, slit widths of 400 μm and a 100x magnification lens.

5.2 Polystyrene Sphere Mapping

Proof of principle studies were first conducted with NAVDY spheres on an anti-avidin functionalized microelectrode with collection and capture performed the same as detailed in Chapter 3. In order to provide some baseline scans for comparison, Raman spectra were recorded for an anti-avidin functionalized silicon surface and from a confluent layer of NAVDY particles dried on a glass slide. The scans for these two substances are presented in Figure 43.

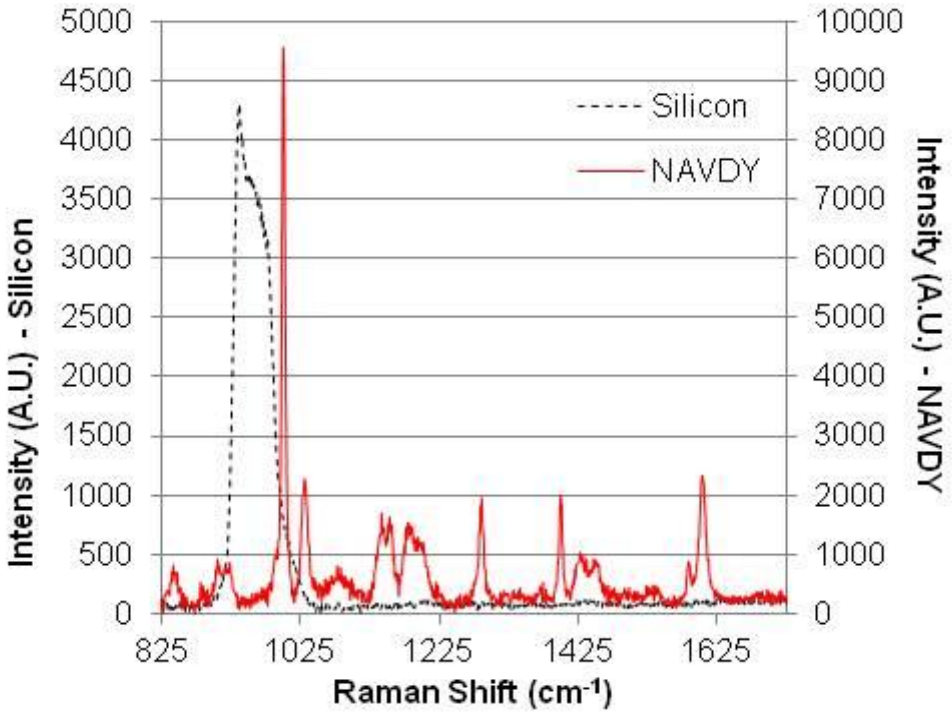

Figure 43: Raman Spectra of a cleaned silicon surface (black line, left y-axis) and a dried, densely packed, photobleached layer NAVDY particles on a glass slide (red line, right y-axis)

The Raman spectrum for the functionalized silicon substrate for the range between 825 and 1675 cm^{-1} is a relatively flat line with a distinct peak at 938 cm^{-1} and a shoulder in the range of 950 to 1040 cm^{-1}. Within the same range analyzed for the functionalized silicon, the NAVDY particles contain several identifiable peaks. A summary of the peaks are presented in Table 2. Seven of the peaks found for the NAVDY particles can be attributed to the in plane vibration modes of the styrene molecule found in the polystyrene polymer of which the particle is composed. The numerical associations (*e.g.* 12 A1), presented in Table 2 designate the various vibrational modes identified to occur in the styrene molecule. Appendix A illustrates the types of ring breathing indentified in the range studied.

Table 2: Summary of identified peaks for NAVDY particles presented in Figure 43

Wavenumber (cm^{-1})	Attributed to	Reference
840	Polystyrene	2
885	-	
908	-	
915	Polystyrene	2
999	12 A1 – Ring Breathing	1,2
1028	18a A1 – Ring Breathing	1,2
1141	Polystyrene	2
1150	15 B2 – Ring Breathing	1,2
1182	9a A1 – Ring Breathing	1,2
1200	Polystyrene	2
1284	-	
1397	-	
1429	-	
1447	19b B2 – Ring Breathing and δCH_2	1,2
1585	8b B2 – Ring Breathing	1,2
1603	8a A1 – Ring Breathing	1,2

Ref 1 – (Jasse *et al.*, 1978); Ref 2 – (Lin-Vien *et al.*, 1991)

Figure 44 presents the Raman scans for a functionalized microelectrode with collected NAVDY particles on the surface (same collection procedure as that applied in Chapter 3) and how the Raman scans would appear for a typical collection. The distinct peaks of the NAVDY particles present in Figure 43 becomes overwhelmed by the surrounding silicon and are more difficult to distinguish. However, peaks specific to polystyrene at 1603, 1430, 1180 and 999 cm^{-1}

are still visible and become easier to identify when the spectrum's magnitude is increased. Since this collection uses negative dielectrophoresis, the absence of any polystyrene peaks in the gold scan is expected and polystyrene is only present when the identifiable silicon peaks are also present (938 and 950 to 1040 cm^{-1}). As the peak at 999 cm^{-1} is the peak with the highest intensity mapping of the surface will be conducted in reference to this peak.

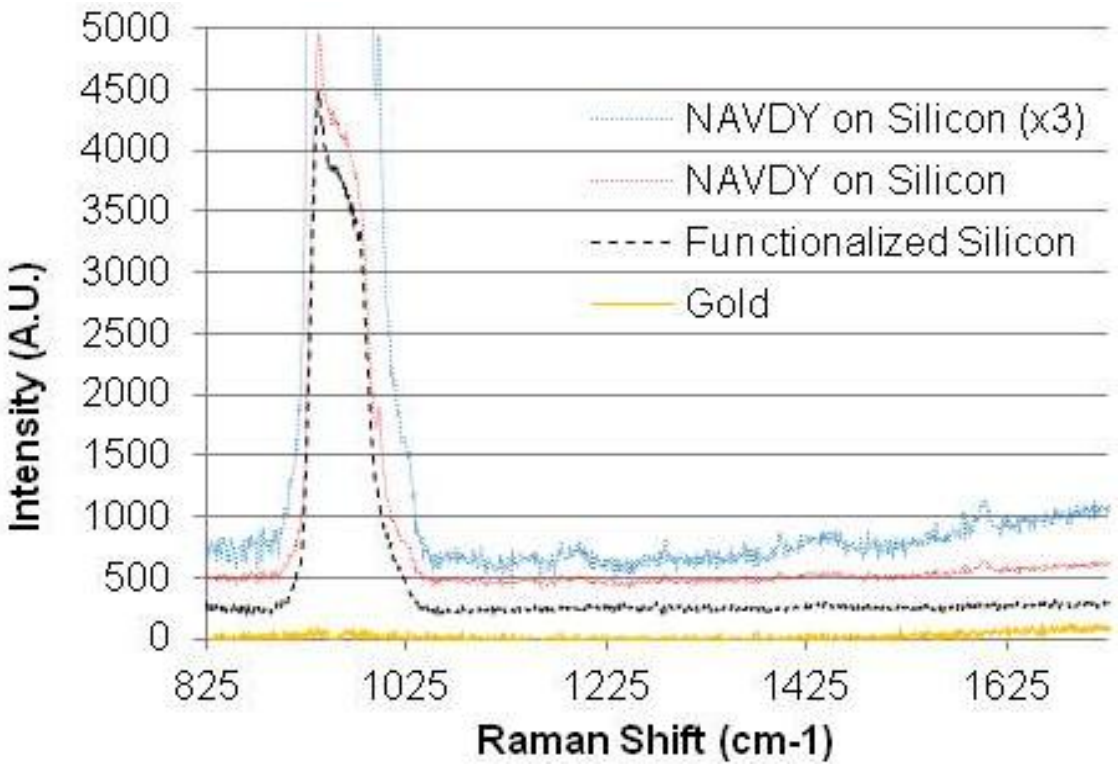

Figure 44: Raman Spectra collected from an anti-avidin functionalized microelectrode chip: a gold surface (yellow / bottom most line); functionalized silicon (black line, positive shifted by 250 A.U.); NAVDY captured particles on Silicon (red line, positive shifted by 500 A.U.); and the captured NAVDY particles on Silicon spectra multiplied by a factor of 3 (blue line, positive shifted by 750 A.U.)

A typical collection of NAVDY particles is shown in Figure 45a where the presence of the particles is confirmed using UV light and shows as the bright green dot in the centre. The area in the white box is magnified and shown in Figure 45b where NAVDY particles are visible in the centre. The white box represents a 20 μm^2 area where Raman mapping occurred. The ratio of the intensity of the peak at 999 cm^{-1} divided by the intensity of the peak at 1015 cm^{-1} is shown in Figure 45c. This mapping is an example of how the Raman spectroscope detection principle could be integrated with negative dielectrophoresis in a surface based biosensor for the detection of pathogens. The edges of the electrodes, represented by the dark blue areas, outline the area for Raman scanning and provide alignment. As shown in Figure 45c, because of the unique peak at 999 cm^{-1}, the NAVDY particles show up as red on the mapped surface. Areas of high concentration appear red while areas of low concentration show up as turquoise. The green areas represent the bare silicon surface without any NAVDY particles. The collection pattern is consistent with what is expected for the negative DEP collection of particles. The highest concentration of particles occurs in the centre of the electrode and diminishes closer to the electrode edge.

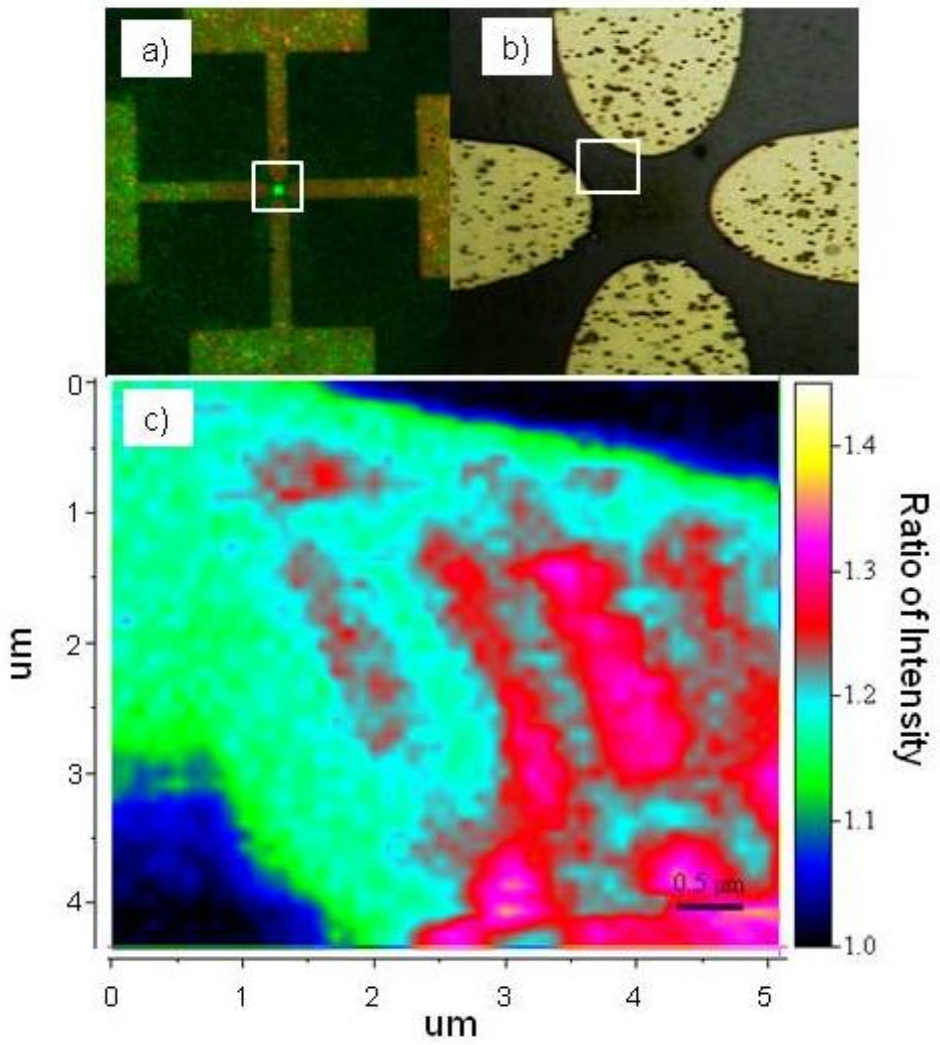

Figure 45: Raman mapping for the identification of NAVDY particles. a) UV-light image of NAVDY particles captured with a circular electrode having a 10 um gap. The white box indicates the area that is magnified in the following inset. b) Magnified area from inset a) under visible light. The white box indicated the area that is magnified in the following inset. c) Raman mapping image of the area indicated in inset b). The x and y- axes represent the area scanned while the colour intensity plot is the ratio of the intensity of a shift at 999 cm^{-1} divided by the intensity at a shift of 1015 cm^{-1}. The dark blue areas are the gold electrodes, the green areas are the silicon surface and the red areas indicate the presence of polystyrene.

A similar collection mapping scheme is presented in Figure 46 side by side with a scanning electron micrograph. NAVDY particles were collected under negative dielectrophoretic conditions onto an anti-avidin functionalized surface. After the sample was dried, it was placed in a vacuum for scanning electron microscope (SEM) imaging. Unlike the mapped image in Figure 45, the Raman mapping of Figure 46 has the color intensity inverted where the red/white areas in the map indicate the location of the gold electrodes while the dark blue areas are the silicon background and the green clusters indicate the NAVDY spheres. Figure 46 presents how closely the Raman system approximates the location of the NAVDY spheres on the surface of microelectrode surface and its consistency with the expected negative DEP collection pattern. In the bottom right, the density of the spheres are the highest. At the electrode edges, the force of negative DEP pushes particles away and a band of silicon is present. Closer to the electrode channel, the particle density drops and the silicon substrate becomes more prominent.

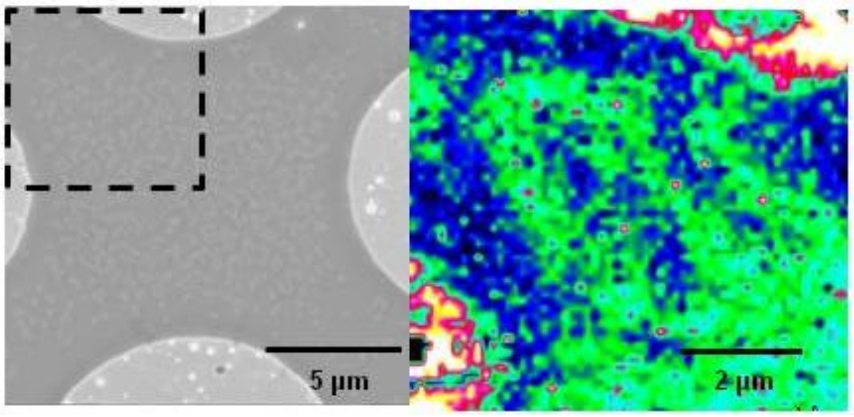

Figure 46: Left - SEM image with a magnification of 5500x of NAVDY particles captured on an anti-avidin functionalized surface. Right –Raman mapping of a portion of the SEM image as indicated by the dashed lines. Raman mapping taken with a 100x magnification lens with a point acquisition time of 5s with a 100 nm step.

5.3 M13 Phage Detection

With the proof of principle established in the previous section, a suitable pathogenic particle was required for the next stage of research. M13 phage was chosen because it is a biohazard level 1 pathogenic particle that infects *E. coli* and has commercially available antibodies. M13 phages are filamentous and are generally 7 nm in diameter and 900 nm in length (Stopar *et al.*, 2003). Figure 47 is a schematic representation of a M13 phage which outlines the various proteins on the surface. The majority of the coat proteins on the M13 phage consist of approximately 2800 GP8 proteins and the GP8 protein is the complimentary antigen to the anti-fd antibody used in this research.

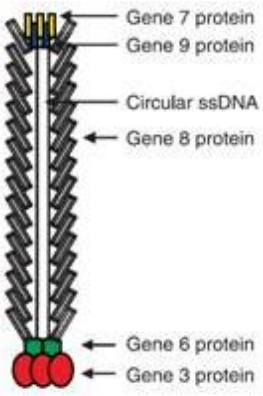

Figure 47: A graphical representation of the M13 phage (Stopar *et al.*, 2003)

Literature has reported on the Raman spectra of the fd phage, a phage from the Ff class which share structural similarities with the M13 phage like the size and structure of the DNA loop and the 2800 GP8 coat proteins which make up the majority of its surface (Aubrey and Thomas, 1991). 10 μL samples with concentrations ranging from 50-80 mg / mL were used to identify the Raman spectra of the fd phage with the resulting spectra presented in Figure 48. (Aubrey and

Thomas, 1991). With an average molecular weight of $1.64 \cdot 10^7$ Da, this corresponds to a concentration of approximately $2 \cdot 10^{15}$ particles / ml (Li *et al.*, 2010).

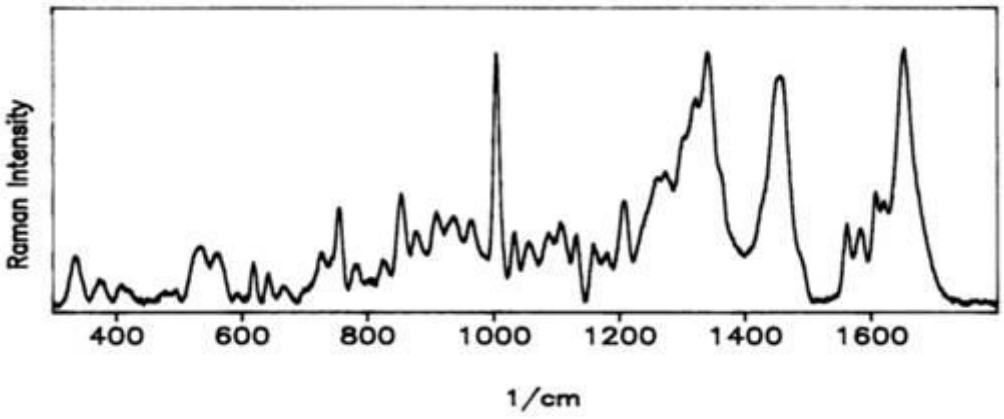

Figure 48: Raman spectra of the fd phage (300-1,800 cm^{-1}). From Aubrey and Thomas (1991).

Prior to any experiments using AC electrokinetics, attempts were made to obtain a scan of the freeze dried M13 phage pellet received from the supplier. Under a microscope, the surface of the solid was irregular and the Raman laser could not be focused sufficiently to provide a reasonable spectrum. A portion of the sample was dissolved in water and dried on a silicon surface. The spectrum is presented in Figure 49 and only peaks consistent with a silicon surface were observed. Initial experiments, involving both positive and negative dielectrophoretic collection, could not detect M13 phage particles using Raman spectroscopy, even after 3 hours of collection.

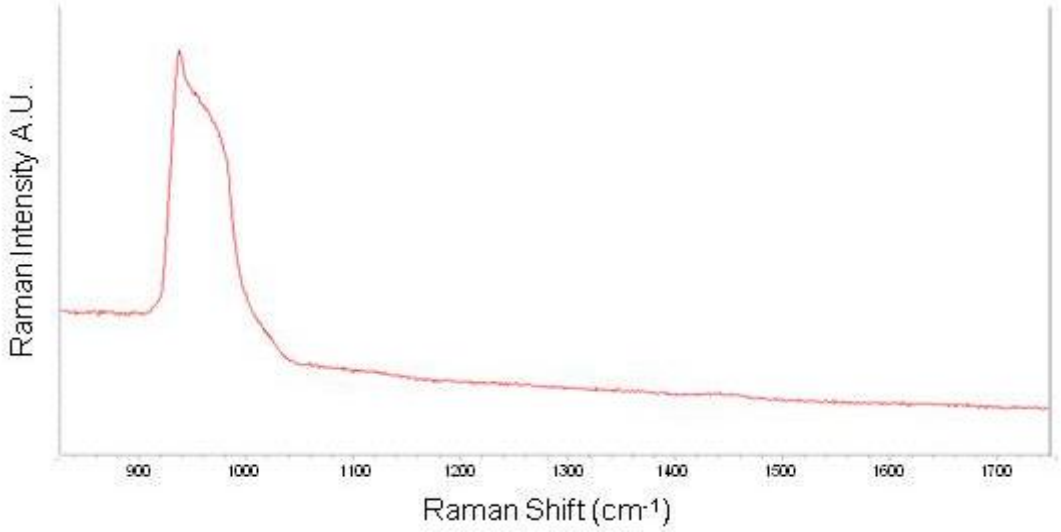

Figure 49: Raman spectrum of the M13 phage pellet placed on a silicon wafer.

Surface enhanced Raman spectroscopy has been shown to enhance the Raman signal for biological molecules (Schultz *et al.*, 2009). M13 phages were collected via positive DEP onto an anti-fd functionalized surface. Colloidal gold with a diameter of 100 nm was then allowed to dry on the surface. Figure 50 compares the Raman scans before (top) and after (bottom) collection of the M13 phage. The presence of the colloidal gold enabled some peaks to become easier to identify, however, no new peaks were identified after collection.

Based on the experimental conditions, the expected dielectrophoretic force on the M13 phage, when modeled as a prolate ellipsoid, would be approximately 7.61 fN. In comparison, the force due to nDEP on the *vesicular stomatitis* virus from Docoslis *et al.* (2007) was on the order of 220 fN. However, results from Morgan and Green (1997) suggested that the threshold force required to overcome Brownian for a virus of comparable size and aspect ratio to that of the M13 phage, is 3.16 fN. Due to the magnitude of the forces involved, a method for confirming the presence or absence of M13 phage was necessary.

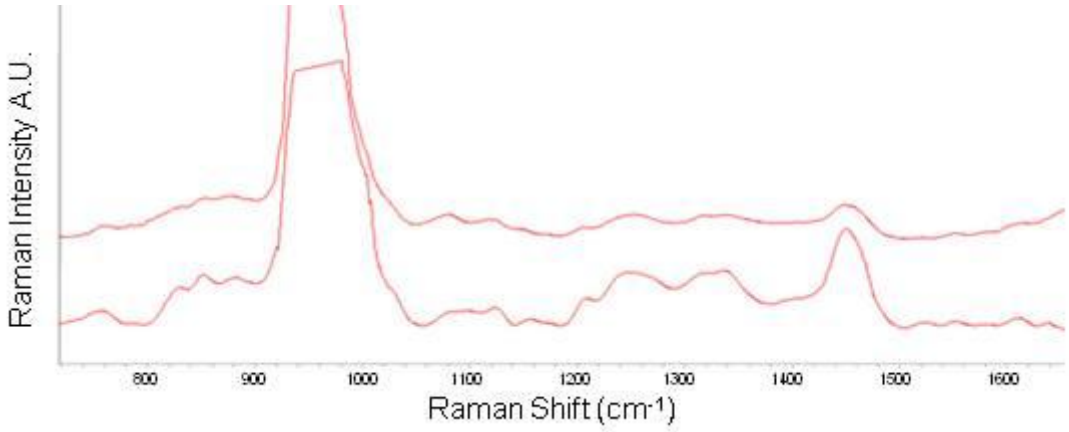

Figure 50: Raman spectra for an anti-fd functionalized silicon surface (top) and positive dielectrophoretically captured M13 phage with 100 nm gold colloidal particles (bottom).

In order to confirm the presence of the M13 phage particles a tagging strategy was used with the details outlined in section 5.1.2.2. A comparison is presented in Figure 51 between the collection of M13 phage (right) and a control sample without M13 phage (left). The control demonstrates that any potential degradation of the electrodes does not cause a false positive indicating collection. The positive DEP collection of M13 phage is shown by the red shaped "x". As the M13 phage does not naturally fluoresce, both the control and the captured M13 phage microelectrodes were allowed to react with the M13 phage with biotinylated anti-fd which was then reacted with the fluorescent compound, NeutrAvdin-Cy3.

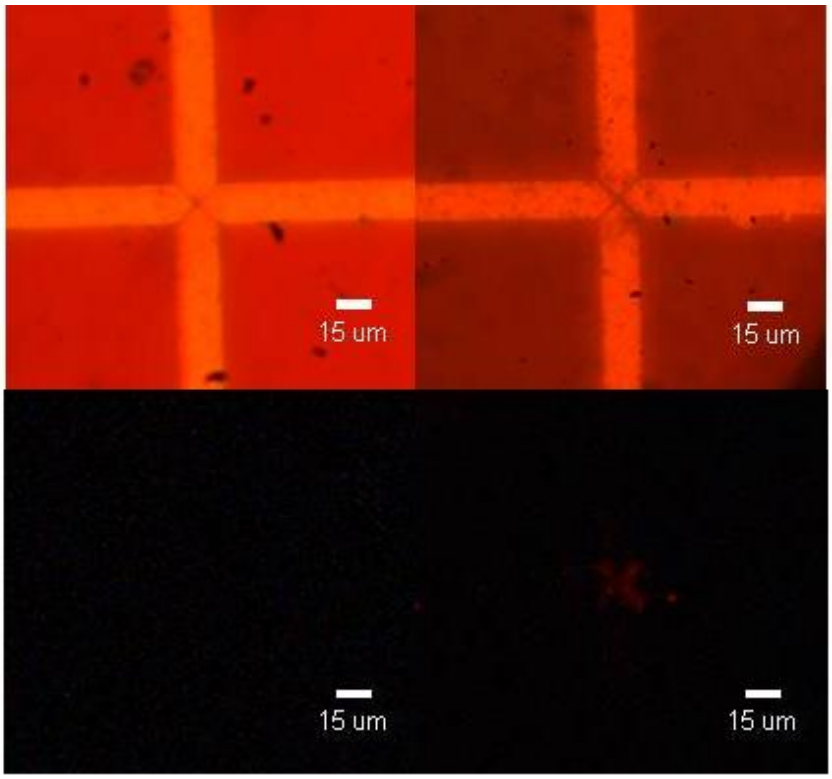

Figure 51: Demonstration of M13 capture using triangular electrodes with a gap spacing of 4 µm. Left: White light (top) and UV light (bottom) images of anti-fd functionalized electrodes. Right: White light (top) and UV light (bottom) images of anti-fd functionalized electrodes with M13 phage. Both electrodes had an applied electric field of 15 V_{pp}, 1 MHz for 1 hour and underwent the same washing procedure described in section 5.1.2.

A Raman scan of the NeutrAvidin-Cy3 compound is shown in Figure 52 offset by 1000 A.U. The most distinct peaks occur from 2830 to 3024 cm^{-1} with maxima at 2885 and 2940 cm^{-1} and a shoulder at 2983 and 3010 cm^{-1}. A wide peak is also present from 2700 to 2765 cm^{-1} and a narrower one present at 3070 cm^{-1}. The inset in Figure 52 indicates three different locations where Raman scans were done. Three locations are highlighted: a purple location in the upper left of the "X", a yellow location closer to the centre of the "X" from the bottom left and a green

location away from the centre of the microelectrode. As expected with positive DEP, the location away from the electrode tips shows no indication of any NeutrAvidin-Cy3 being detected by the Raman scans. The two other scans present in the figure are offset by 200 and 800 A.U and differ in their relative intensity. Both sets of scans have peaks at 2940 cm^{-1}, 2880 cm^{-1} and at 2860 cm^{-1} which are attributed to methyl stretching. These bands are also present on the NeutrAvidin-Cy3 scan, although the relative intensities may be different. These differences in intensities may be attributed to molecular orientation (Maher *et al.*, 2002). Furthermore, the yellow scan shares the same wide peak from 2700 to 2765 cm^{-1} and the narrower one present at 3070 cm^{-1} that are exhibited by the NeutrAvidin-Cy3 scan. The similarities of these scans indicate the successful detection of labeled M13 phage on a Raman coupled AC electrokinetically enhanced surface-based biosensor.

The difference in the intensity of the purple and yellow scans in Figure 52 highlights an important consideration when designing microelectrodes for detection with a coupled Raman system. The intensity of a peak is related to the concentration of the analyte in the scanned point. In the case of the M13 phage which has a high aspect ratio, the point being scanned may not encompass the entire volume of the phage. Therefore, if the confirmation is based solely on intensity the data may be misinterpreted. However, the use of relative intensity, as shown in Figure 45 for the NAVDY particles, would allow for the accurate identification of the target pathogen regardless of absolute intensity of a single peak.

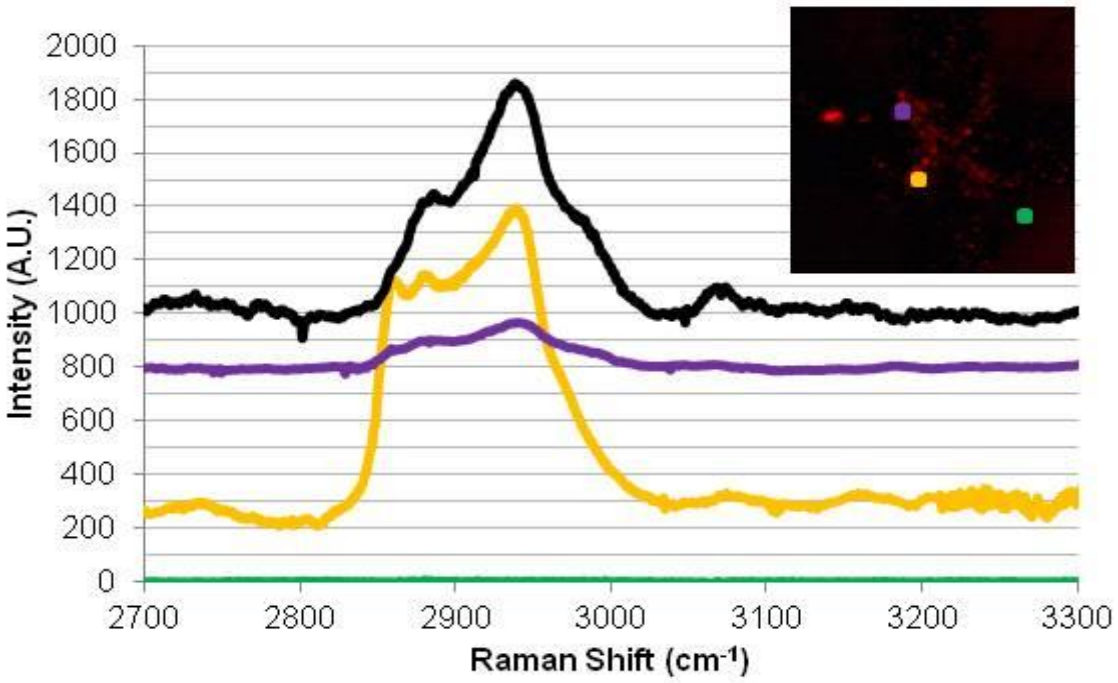

Figure 52: Raman spectra collected from an anti-fd functionalized microelectrode with captured M13 phages bound to biotinylated-anti-fd reacted with ExtrAvidin-Cy3 prior to photobleaching. The inset in the top right is a magnified image of the collection presented in Figure 51. The black line (positive shifted by 1000 A.U.) is a photobleached sample of ExtrAvidin-Cy3 on Silicon. The purple line (positive shifted by 800 A.U.) is the scan from the top left point in the inset (indicated by the purple dot),. The yellow line (positive shifted by 250 A.U.) is the scan from the bottom left point in the inset (indicated by the yellow dot). The green line is the scan from the bottom right point in the inset (indicated by the green dot).

While the M13 phage can be detected via Raman spectroscopy without the need for a labeling agent, as shown in Figure 48, the concentration of the phage at the electrode edges was not sufficient to enable detection. Furthermore, attempts at employing SERS or increasing exposure times did not result in the detection of the phage. The geometry of the M13 phage means that a non-closely packed monolayer may not provide sufficient mass to enable a Raman

signal. It may be possible to enable the label free detection of a monolayer of viruses with Raman spectroscopy if the target viruses are spherical or rod shaped in nature, thus providing a larger volume during the acquisition of the signal.

5.4 Conclusions

Raman spectroscopy has been combined with a surface based biosensor for the detection of labeled virus sized pathogenic particles. AC electrokinetic effects were used in conjunction with Raman spectroscopy to enable the collection of M13 phage. The proof of principle surface mapping using protein coated polystyrene spheres also proposes a methodology for the detection of bioparticles via surface mapping. Furthermore, the use of the NeutrAvidin-Cy3 allowed for the rapid indirect detection of virus particles using Raman spectroscopy on a surface based biosensor for the first time. The information presented provides insights for the design of Raman coupled surface based biosensors, where AC electrokinetic effects can allow the sampling of pathogenic particles that would otherwise be undetectable.

Chapter 6 Summary and Conclusion

Traditional biosensors remain bottlenecked during sampling because they are diffusion limited. This work sought to examine the synergism between the electrothermal flows and dielectrophoresis for a set of microelectrode designs in order to propose a way by which this limitation can be overcome. Numerical simulations were used to identify the effects of microelectrode design features while proof of principle experiments validated the models and examined how specificity could be employed. A microelectrode sharing similar design features to those studied in the numerical simulations was incorporated into a cantilever biosensor to evaluate the influence that the cantilever beam would have on the nature and direction of the fluid flows and forces on the suspended particles. Numerical simulations compared the cantilever design setups and proof of principle experiments demonstrated how the cantilever based detection of bacteria could be enhanced with AC electrokinetics. An AC electrokinetically enhanced biosensor coupled with a detection method could also potentially allow for the one step concentration and detection of viruses. A Raman spectroscopy coupled surface based biosensor indirectly detected a phage where microelectrodes used AC electrokinetics to accelerate the sampling and overcome the diffusion limitation.

AC electrokinetic effects have been employed to accelerate the transport of both model bioparticles and pathogens from the bulk to target locations on microfabricated quadrupolar electrodes. Numerical simulations, verified by experimental observations, have demonstrated that for high conductivity solutions, the presence of electrode channels would reduce the number of paths available for bioparticles to reach the negative dielectrophoretic trap in the centre of the

design. The electrode channels were also found to create secondary collection areas which did not directly assist in particle collection. Specificity for the AC electrokinetically enhanced collection of target bioparticles was demonstrated using the circular microelectrodes while sampling a heterogeneous population of polystyrene spheres. The collection pattern was consistent with the negative dielectrophoretic collection predicted by the numerical simulations.

Prototype cantilever beams with embedded microelectrodes were analyzed in the context of the capture of bacteria in low conductivity solutions. Numerical simulations identified that placing electrodes below the cantilever would impede flow from the bulk. Placing the electrodes on the surface of the cantilever provided multiple locations for secondary collections due to the presence of the connecting wires. Experimental results of the coupled electro-mechanical biosensor were shown to enhance the collection of *E. coli* from solution by means of AC electrokinetics. Bacteria captured within 30 minutes doubled the shift in resonant frequency for the highest resonant mode measured with respect to unassisted collection.

A potential method for the detection of pathogens was proposed which combines the enhanced sampling of AC electrokinetics with the optical "fingerprinting" of Raman spectroscopy. The proof of principle surface mapping of model bioparticles was presented with a methodology for analyzing the resulting spectra. When the same technique was applied to the electrokinetic capture of M13 phage particles they were indirectly confirmed with Raman spectroscopy using a labeling molecule, NeutrAvidin-Cy3. The combination of AC electrokinetic enhanced sampling with Raman based detection provides a framework for the real time or online detection of viruses *in situ*.

6.1 Recommendations for Future Work

The circular electrode design is a promising starting point for the capture of pathogenic particles using negative DEP. However, there remains the need for a study to identify the best electrode designs and features via numerical simulations. Smaller electrode gaps would provide stronger AC electrokinetic effects that could potentially allow for the negative DEP collection of pathogens which would not normally be able to be collected, like the M13 phage. Furthermore, a parametric study that explores the effects of voltage, frequency and medium conductivity as a function of particle size would enable for the optimized collection of bioparticles from heterogeneous samples. By limiting collection to a specific point via negative dielectrophoresis, that area for detection is then minimized. A coupled detection method, like Raman, could scan these concentrated target areas for the rapid testing of multiple samples. Alternatively, the reduced foot print would allow for the placement of multiple arrays on a single substrate. If each portion of the array could be made to be specific to a target bioparticle, the high throughput screening of a sample could be achieved. Additionally, by focusing collection on the substrate, the properties of different substrates can be exploited. For example, a glass substrate would allow for optical detection from beneath the sample.

For the microelectrode integrated cantilevers, the design of the cantilever and the electrodes must be re-examined. While the current design of microelectrodes on the surface of the cantilever is versatile, a thinner beam, both in terms of thickness and width, would allow for a more sensitive detection platform. Furthermore, for samples with low conductivity, the efficiency of positive dielectrophoresis collection can be enhanced by increasing the length of the microelectrode edges. The method for functionalization also needs to be explored in the context of the cantilever beam as the single crystal silicon material may inhibit the antibody

functionalization method used. Alternative silinization agents, such as those with longer alkyl chains, should be explored to enhance the formation of the monolayer prior to functionalization. Finally, each step in the functionalization needs to be examined for optimization.

The Raman spectroscopic detection of viruses has significant potential for identifying viruses from heterogeneous populations based on their unique "fingerprints". The M13 phage used in this work has a radius of only 7 nm and may be too small for detection using the current setup. The quadrupolar microelectrodes can be used to collect viruses of larger radii, for example, the *Vesicular Stomatitis* virus (rod shaped; ~170 nm long and ~70nm diameter), to determine the minimum radius required for the label free detection of viruses.

Further studies should expand the proof of principles explored here to include samples of heterogeneous populations or viruses. The culmination of this work would enable AC electrokinetic applications in commercially available biosensors which could be applied to improve sampling time or enable detection at lower concentrations. The proposed cantilever prototype can be developed into such a biosensor with AC electrokinetic enhanced sampling. The device has the capability for high-throughput testing since it can be integrated into a flow through assembly. Similarly, an automated setup for the scanning and analysis of AC electrokinetically enhanced biosensors coupled with Raman spectroscopy would enable the timely detection of target pathogens on the electrode surface.

References

Akin, D., Li, H., and Bashir, R. (2004). Real-Time Virus Trapping and Fluorescent Imaging in Microfluidic Devices. *Nano Lett.,* Vol. 4, pp. (257-259)

Allsopp, D.W.E., Milner, K.R., Brown, A.P., and Betts, W.B. (1999). Impedance technique for measuring dielectrophoretic collection of microbiological particles. *J. Phys. D: Appl. Phys.*, Vol. 32, pp. (1066-1074)

Asbury, C.L., Diercks, A.H., and Engh, G.V.D. (2002). Trapping of DNA by dielectrophoresis. *Electrophoresis,* Vol. 23, pp. (2658-2666)

Alvarez, M. and Lechuga, L.M. (2010) Microcantilever-based platforms as biosensing tools, *Analyst*, Vol. 135, pp. 827-836

Aubrey, K.L. and Thomas, G.J.Jr. (1991) Raman Spectroscopy of filamentous bacteriophage Ff (fd, M13, f1) incorporating specifically-deuterated alanine and tryptophan side chains Assignment and structural interpretation. *Biophysical Journal*, Vol. 60, pp. 1337-1349

Asbury, C.L. and van den Engh, G. (1998) Trapping of DNA in nonuniform oscillating electric fields. *Biophysical Journal*, Vol. 74, pp. 1024-1030

Beck, J.D., Shang, L., Marcus, M.S., and Hamers, R.J. (2005). Manipulation and Real-Time Electrical Detection of Individual Bacterial Cells at Electrode Junctions: A Model for Assembly of Nanoscale Biosystems*Nano Lett.,* Vol. 5, pp. (777-781)

Becker, F.F., Wang, X-B., Huang, Y., Pethig, R., Vykoukal, J., and Gascoyne, P. R. (1995). Separation of human breast cancer cells from blood by differential dielectric affinity. *Proc. Natl. Acad. Sci. USA, Cell Biology*, Vol. 92, pp. (860-864)

Betts, W. B. (1995). The potential of dielectrophoresis for the real-time detection of microorganisms in foods. *Trends in Food Sci. Technol*., Vol. 6, pp. (51-58)

Bhatia, S.K., Shriver-Lake, L.C., Prior, K.J., Georger, J.H., Calvert, J.M., Bredehorst, R., and Ligler, F.S. (1989). Use of Thiol-terminated silanes and heterobifunctional crosslinkers for immobilization of antibodies on silica surfaces. *Anal. Biochem.,* Vol. 178, pp. (408-413)

Burt, J.P. H., Al-Ameen, T.A.K, and Pethig, R. (1989). An optical dielectrophoresis spectrometer for low –frequency measurements on colloidal suspensions. *J. Phys. E: Sci. Instrum.*, Vol. 22, pp. (952-957)

Castellanos, A., Ramos, A., Gonzalez, A., Green, N.G., and Morgan, H. (2003). Electrohydrodynamics and dielectrophoresis in Microsystems: scaling laws. *J. Phys. D: Appl. Phys.*, Vol. 36, pp. (2584-2597)

Chen, D.F., Du, H., Li, W.H., (2006) A 3D paired microelectrode array for accumulation and separation of microparticles. *J. Micromech Microeng.*Vol. 16, pp. (1162-1169)

Cheng, I.-F., Lin, C.-C., Lin, D.-Y., Chang, H.-C. (2010) A dielectrophoretic chip with a roughened metal surface for on-chip surface-enhanced Raman scattering analysis of bacteria. *Biomicrofluidics*, Vol. 4, pp. (034104,1-11)

Cheng, J., Sheldon, E.L., Wu, L., Uribe, A., Gerrue, L.O., Carrino, J., Heller, M.J., and O'Connell, J.P. (1998a). Preparation and hybridization analysis of DNA/RNA from E. coli on microfabricated bioelectronic chips. *Nature Biotechnology*, *Vol.* 16, *pp. (*541-546)

Cheng, J., Sheldon, E.L., Wu, L., Heller, M.J., and O'Connell, J.P. (1998b). Isolation of Cultured Cervical Carcinoma Cells Mixed with Peripheral Blood Cells on a Bioelectronic Chip. *Anal. Chem.*, Vol. 70, pp. (2321-2326)

Cheng, I–F., Chang, H–C., Hou, D., and Chang, H–C. (2007). An integrated dielectrophoretic chip for continuous bioparticle filtering, focusing, sorting, trapping, and detecting. *Biomicrofluidics*, Vol. 1, pp. (021503:1-15)

Chon, J.W.M., Mulvaney, P., and Sader, J.E., (2000). Experimental validation of theoretical models for the frequency response of atomic force microscope cantilever beams immersed in fluids. *J. Appl. Phys.*, Vol. 87, No. 8, pp. (3979-3988).

Chou, C-F., Tegenfeldt, J. O., Bakajin, O., Chan, S. S., Cox, E. C., Darnton, N., Duke, T. and Austin, R. H. (2002). Electrodeless Dielectrophoresis of Single- and Double-Stranded DNA. *Biophysical Journal*, Vol. 83, pp. (2170-2179)

Costanzo, P. J., Liang, E., Patten, T. E., Collins, S. D., and Smith., R. L. (2005). Biomolecule detection via target mediated nanoparticle aggregation and dielectrophoretic impedance measurement. *Lab Chip*, Vol. 5, pp. (606-610)

Cui, L., Zhang, T., and Morgan, H. (2002). Optical particle detection integrated in a dielectrophoretic lab-on-a-chip. *J. Micromech. Microeng.*, Vol. 12, pp. (7-12)

Dewarrat, F., Calame, M., and Schönenberger, C. (2002). Orientation and Positioning of DNA Molecules with an Electric Field Technique. *Single Mol.*, Vol. 3, pp. (189-193)

Dimitrov, D.S., and Zhelev, D.V. (1987). Dielectrophoresis of individual Cells: experimental Methods and results, *Bioelectrochemistry and Bioenergetics,* Vol. 17, pp. (549-557)

Docoslis, A., and Alexandridis, P. (2002). One-, two-, and three-dimensional organization of colloidal particles using nonuniform alternating current electric fields. *Electrophoresis,* Vol. 23(14), pp. 2174-2183

Docoslis, A., Espinoza, L.A.T., Zhang, B., Cheng, L-L., Israel, B.A., Alexandridis, P., and Abbott, N.L. (2007) Using Nonuniform Electric Fields To Accelerate the Transport of Viruses to Surfaces from Media of Physiological Ionic Strength. *Langmuir*, Vol. 23,, pp. (3840-3848)

Fatoyinbo, H.O., Hoettges, K.F., Reddy, S.M., and Hughes, M.P. (2007). An integrated dielectrophoretic quartz crystal microbalance (DEP-QCM) device for rapid biosensing applications. *Biosensors and Bioelectronics,* Vol. 23, pp. (225-232)

Feng, J.J., Krishnamoorthy, S., and Sundaram, S. (2007). Numerical analysis of mixing by electrothermal induced flow in microfluidic systems. *Biomicrofluidics*, Vol. 1, pp. (024102:1-8)

Frenea, M., Faure, S.P., Le Pioufle, B., Coquet, Ph., and Fujita, H. (2003). Positioning living cells on a high-density electrode array by negative dielectrophoresis. *Materials Science and Engineering C*, Vol. 23, pp. (597-603)

Gagnon, Z., and Chang, H-C. (2005). Aligning Fast Alternating Current Electroosmotic Flow Fields and Characteristic Frequencies with dielectrophoretic Traps to Achieve Rapid Bacteria detection. *Electrophoresis*, Vol. 26, pp. (3725-3737)

Gagnon, Z., Senapati, S., Gordon, J., and Chang, H–C. (2008). Dielectrophoretic detection and quantification of hybridized DNA molecules on nano-genetic particles. *Electrophoresis*, Vol. 29, pp. (4808-4812)

Gascoyne, P.R.C., Huang, Y., Pethig, R., Vykoukal, J., and Becker, F. F. (1992). Dielectrophoretic separation of mammalian cells studied by computerized image analysis. *Meas. Sci. Technol*., Vol. 3, pp. (439-445)

Gascoyne, P., Satayavivad, J., and Ruchirawat, M. (2004). Microfluidic approaches to malaria detection. *Acta Tropica*, Vol. 89, pp. (357-369)

Gray, D.S., Tan, J.L., Voldman, J., and Chen, C.S. (2004) Dielectrophoretic registration of living cells to a microelectrode array. *Biosens. Bioelec*, Vol. 19, pp. (771-780)

Green, N.G., and Morgan, H. (1997). Dielectrophoretic investigations of sub-micrometre latex spheres. *J. Phys. D: Appl. Phys.*, Vol. 30, pp. (2626-2633)

Green, N.G., Morgan, H., and Milner, J.J., (1997). Manipulation and trapping of sub-micron bioparticles using dielectrophoresis. *J. Biochem. Biophys. Methods*, Vol. 35, pp. 89–102.

Green, N.G., and Morgan, H. (1998). Separation of submicrometre particles using a combination of dielectrophoretic and electrohydrodynamic forces. *J. Phys. D: Appl. Phys*., Vol. 31, pp. (L25-L30)

Green, N.G., Ramos, A., Gonzalez, A., Morgan, H., and Castellanos, A. (2000). Fluid flow induced by nonuniform ac electric fields in electrolytes on microelectrodes. I. Experimental Measurements. *Physical Review E*, Vol. 61, No. 4, pp. (4011-4018)

Green, N.G., Ramos, A., and Morgan, H. (2000a). AC Electrokinetics: a survey of submicrometer particle dynamics. *Journal of Physics D: Applied Physics*. Vol. 33, pp. (632-641)

Green, N.G., Ramos, A., Gonzalez, A., Morgan, H., and Castellanos, A. (2002). Fluid flow induced by nonuniform ac electric fields in electrolytes on microelectrodes. III. Observation of streamlines and numerical simulation. *Physical Review E*, Vol. 66, pp. (026305:1-11)

Grom, F., Kentsch, J., Müller, T., Schnelle, T., and Stelzle, M. (2006). Accumulation and trapping of hepatitis A virus particles by electrohydrodynamic flow and dielectrophoresis. *Electrophoresis*, Vol. 27, pp. (1386-1393)

Guan, J.G., Miao, Y.Q., and Zhang, Q.J. (2004). Impedimetric Biosensors. *Biosci. Bioeng*., Vol. 97, pp. (219-226)

Gunter, R.L., Delinger, W.G., Manygoats, K., Kooser, A., and Porter, T. L., (2003). Viral detection using an embedded piezoresistive microcantilever sensor. *Sens. Actuators A*, Vol. 107, pp. (219-224)

Gupta A., Akin, D., and Bashir R. (2004) Single virus particle mass detection using microresonators with nanoscale thickness, *Appl. Phys. Lett.* Vol. 84, pp. 1976

Hamblin, M.N., Xuan, J., Maynes, D., Tolley, H. D., Belnap, D. M., Woolley, A. T., Leeb, M. L., and Hawkins, A. R. (2010). Selective trapping and concentration of nanoparticles and viruses in dual-height nanofluidic channels. *Lab Chip*, Vol. 10, pp. (173-178)

Henning, A., Henkel, J., Bier, F.F., and Hölzel, R. (2008). Label-free electrical quantification of the dielectrophoretic response of DNA. *PMC Biophysics* Vol. 1, No. 4

Hoettges, K.F., Hughes, M.P., Cotton, A., Hopkins, N.A.E., and McDonnell, M.B. (2003a). Optimizing particle collection for enhanced surface based biosensors. *IEEE Eng. Med. Biol. Mag.*,Vol. 22, No. 6, pp. (68–74)

Hoettges, K.F., McDonnell, M.B., and Hughes, M.P. (2003). Use of combined dielectrophoretic/electrohydrodynamic forces for biosensor enhancement. *J. Phys. D: Appl. Phys.*, Vol. 36, pp. (L101-L104)

Hölzel, R., and Bier, F.F. (2003). Dielectrophoretic manipulation of DNA. *IEE Proc-Nanobiotechnol.*, Vol. 150, pp. (47-53)

Hölzel, R., and Bier, F.F. (2004). Monitoring Dielectrophoretic Collection of DNA by Impedance Measurement. *AIP Conference Proceedings*, Vol. 725, pp. (77-83)

Hou, D., Maheshwari, S., and Chang, H.C. (2007). Rapid bioparticle concentration and detection by combining a discharge driven vortex with surface enhanced Raman scattering. *Biomicrofluidics*, Vol. 1, pp. (014106:1-13)

Huang, Y., and Pethlg, R. (1991). Electrode design for negative dielectrophoresis. *Meas. Sci. Technol.*, Vol. 2, pp. (1142-1146)

Hübner, Y., Hoettges, K.F., McDonnell, M.B., Carter, M.J., and Hughes, M.P. (2007). Applications of dielectrophoretic/electro-hydrodynamic "zipper" electrodes for detection of biological nanoparticles. *Int J Nanomedicine.*, Vol. 2, No. 3, pp. (427-431)

Hughes, M. P., Morgan, H., Rixon, F. J., Burt, J. P. H., and Pethig, R. (1998). Manipulation of herpes simplex virus type 1 by dielectrophoresis, *Biochim. Biophys. Acta.*, Vol. 1425, pp. (119-126)

Hughes, M. P., Morgan, H., and Rixon, F. J. (2001). Dielectrophoretic manipulation and characterization of herpes simplex virus-1 capsids. *Eur. Biophys. J.*, Vol. 30, pp. (268-272)

Humberto, F., Morales, F., Duarte, J. E., and Mart ́ı J. S. (2008). Non-uniform electric field-induced yeast cell electrokinetic behavior. *Revista Ingenieria E Investigacion,* Vol. 28, pp. (116-121)

Ilic, B., Czaplewski, D., Craighead, H.G., Neuzil, P., Campagnolo, C., and Batt, C., (2000) Mechanical resonant immunospecific biological detector, *Appl. Phys. Lett*. Vol. 77, pp. 450-452

Illic, B., Craighead, H.G., Krylov, S., Senaratne, W., Ober, C., and Neuzil, P. (2004) Attogram detection using nanomechanical oscillators, *J. Appl. Phys.* Vol. 95, Iss. 7, pp. 3694-3703

Islam, N., Lian, M., and Wu, J. (2007). Enhancing microcantilever capability with integrated AC electroosmotic trapping. *Microfluid. Nanofluid.,* Vol. 3, pp. (369-375)

Jasse, B., Chao, R.S., and Koenig, J.L. (1978). Laser Raman scattering in uniaxially orientated atactic polystyrene. *Journal of Polymer Science: Polymer Physics Edition*. Vol. 16. Iss. 12. pp. (2157-2169)

Jen, C–P., and Chen, T–W. (2009). Selective trapping of live and dead mammalian cells using insulator-based dielectrophoresis within open-top microstructures. *Biomed. Microdevices,* Vol. 11, pp. (597-607)

Kawabata, T., and Washizu, M. (2001). Dielectrophoretic Detection of Molecular Bindings. *IEEE Transactions on Industry Applications*, Vol. 37, pp. (1625-1633)

Koo, O.K., Liu, Y., Shuaib, S., Bhattacharya, S., Ladisch, M.R., Bashir, R., and Bhunia, A.K. (2009). Targeted Capture of Pathogenic Bacteria Using a Mammalian Cell Receptor Coupled with dielectrophoresis on a Biochip. *Anal. Chem.*, Vol. 81, pp. (3094-3101)

Kurosawa, O., Okabe, K., and Washizu, M. (2000). DNA analysis based on physical manipulation. *Proceedings of 13th Micro Electro Mechanical Systems.*, pp. (311-316)

Lagally, E.T., Lee, S-H., and Soh, H.T. (2005). Integrated microsystem for dielectrophoretic cell concentration and genetic Detection. *Lab Chip,* Vol. 5, pp. (1053-1058)

Lapizco-Encinas, B. H., and Palomares, M. R. (2007). Dielectrophoresis for the manipulation of Nanobioparticles. *Electrophoresis*, Vol. 28, pp. (4521-4538)

Li, H., and Bashir, R. (2002). Dielectrophoretic separation and manipulation of live and heat-treated cells of *Listeria* on microfabricated devices with interdigitated electrodes. *Sensors and Actuators B: Chemical*, Vol. 86, pp. (215-221)

Li, D. (2004). *Electrokinetics in microfluidics*, Elsevier

Li, K., Chen, Y., Li, S., Nguyen, H.G., Niu, Z., You, S., Mello, C.M., Lu, X. and Wang, Q. (2010) Chemical Modification of M13 Bacteriophage and Its Application in Cancer Cell Imaging. *Bioconjugate Chemistry*, Vol. 21(7), pp. 1369-1377

Li, M., Qu, Y., Dong, Z., Li, W.J., Wang, Y. (2008) Design and simplification of electrodes for 3D dielectrophoretic trapping. *Proceed. 3rd IEEE int. Conf. Nano/Micro Eng. Mol. Sys.* January 6-9, China.

Linko, V., Paasonen, S–T., Kuzyk, A., Torma, P., and Toppari, J.J. (2009). Characterization of the Conductance Mechanisms of DNA Origami by AC Impedance Spectroscopy. *Small,* Vol. 5, pp. (2382-2386)

Lin-Vien, D., Colthup, N.B., Fateley, W.G., and Grasselli, J.G (1991) The Handbook of Infrared and Raman Characteristics Frequencies of Organic Molecules. Academic Press. Toronto.

Livache, T., Bazin, H., Caillat, P., and Roget., A. (1998). Electroconducting polymers for the construction of DNA or peptide arrays on silicon chips. *Biosensors and Bioelectronics*, Vol. 13, pp. (629-634)

Maher, R.C., Cohen, L.F. and Etchegoin, P. (2002) Single molecule photo-bleaching observed by surface enhanced resonant Raman scattering (SERRS). *Chemical Physics Letters*, Vol. 352, Iss. 5-6, pp. 378-384

Markx, G.H., Huang, Y., Zhou, X-F., and Pethig, R. (1994). Dielectrophoretic characterization and separation of micro-organisms. *Microbiology,* Vol. 140, pp. (585-591)

Markx, G.H., and Pethig, R. (1995). Dielectrophoretic Separation of Cells: Continuous Separation. *Biotechnology and Bioengineering*, Vol. 45, pp. (337-343)

Marshall, W.L., CRC Handbook of Chemistry and Physics, 92nd Edition, Internet Version 2012. *Electrical Conductivity of Water*. Eds: Lide, D.R. pp. (5-72)

Medoro, G., Manaresi, N., Leonardi, A., Altomare, L., Tartagni, M., and Guerrieri, R. (2003). A Lab-on-a-Chip for Cell Detection and Manipulation. *IEEE Sensors Journal,* Vol. 3, No. 3, pp. (317-325)

Menachery, A., and Pethig, R. (2005). Controlling cell destruction using dielectrophoretic Forces. *IEE Proc. Nanobiotechnol*., Vol. 152, pp. (145-149).

Milner, K.R., Brown, A.P., Allsopp, D.W.E., and Betts, W.B. (1998). Dielectrophoretic classification of bacteria using differential impedance measurements. *Electronics Letters,* Vol. 3, pp. (66-68)

Miller, E.M., Ng, A.H.C., Uddayasankar, U., and Wheeler, A.R. (2011) A Digital microfluidic approach to heterogeneous immunoassays. *Analytical and Bioanalytical Chemistry*. Vol. 399, pp. (337-345)

Morgan, H., and Green, N.G. (1997). Dielectrophoretic manipulation of rod-shaped viral particles. *Journal of Electrostatics,* Vol. 42, pp. (279-293)

Morgan, H. and Green, N.G. (2003). *AC electrokinetics: colloids and nanoparticles*, Research Studies Press Ltd.

Moulder, J.F., Stickle, W.F., Sobol, P.E., and Bomben, K.D. (1995) *Handbook of X-ray Photoelectron Spectroscopy*, Eds: Chastain, J., and King, R.C.Jr., Physical Electronics, Eden Prairie.

Müller, T., Fiedler, S., Schnelle, T., Ludwig, K., Junga, H., and Fuhr, G. (1996). High frequency electric fields for Trapping viruses. *Biotechnology Techniques,* Vol. 10 pp. (221-226)

Mullery, T., Gerardinoz, A., Schnelley, T., Shirleyy, S. G., Bordoniz, F., Gasperisz, G. D., Leonix, R., and Fuhr, G. (1996). Trapping of micrometre and sub-micrometre particles by high-frequency electric fields and hydrodynamic forces. *J. Phys. D: Appl. Phys.*, Vol. 29, pp. (340-349)

Oblak, J., Krizaj, D., Amon, S., Macek-Lebar, A., and Miklavcic, D. (2007). Separation of electroporated and non-electroporated cells by means of dielectrophoresis. *IFMBE Proceedings*, Vol. 16, pp. (178-181)

Pandey, S., and White, M.H. (2004). Detection of Dielectrophoretic Driven Passage of Single Cells through Micro-Apertures in a Silicon Nitride Membrane. *Conf. Proc. IEEE Eng. Med. Biol. Soc.*, Vol. 3, pp. (1956-1959)

Park, I-S., and Kim, N. (1998). Thiolated *Salmonella* antibody immobilization onto the gold surface of piezoelectric quartz crystal. *Biosensors and Bioelectronics,* Vol. 13, pp. (1091-1097)

Park, K., Akin, D., and Bashir, R. (2007). Electrical capture and lysis of vaccinia virus particles using silicon nano-scale probe array. *Biomed. Microdevices,* Vol. 9, pp. (877-883)

Park, K., Jang, J., Irmia, D., Sturgis, J., Lee, J., Robinson, P., Tonerd, M., and Bashir, R. (2008). 'Living cantilever arrays' for characterization of mass of single live cells in fluids. *Lab on a Chip*, Vol. 8, pp. (1034-1041)

Pasternack, R.M, Amy, S.R., and Chabal, Y.J. (2008) Attachment of 3-(Aminopropyl)trimethoxysilane on Silicon Oxide Surfaces: Dependance of Temperature. *Langmuir*. Vol. 24 Iss. 22 pp. (12963-12971)

Pejcic, B., de Marco, R., Parkinson, G. (2006) The role of biosensors in the detection of emerging diseases. *Analyst*, Vol. 131, Iss. 10, pp. (1079-1090)

Pethig, R. (1996). Dielectrophoresis: Using In homogeneous AC Electrical Fields to Separate and Manipulate Cells. *Crirical Reviews in Biotechnology,* Vol. 16, pp. (331-348)

Pethig, R., and Markx, G.H. (1997). Applications of dielectrophoresis in biotechnology. *Trends Biotechnol.*, Vol. 15, pp. (426-432)

Pethig, R., Huang, Y., Wang, X-B., and Burt, J.P. H. (1992). Positive and negative dielectrophoretic collection of colloidal particles using interdigitated castellated microelectrodes. *J. Phys. D: Appl. Phys.*, Vol. 24, pp. (881-888)

Pohl, H. A. (1951). The motion and precipitation of suspensoids in divergent electric fields. *Journal of Applied Physics*, Vol. 22, pp. (869-871)

Pohl, H.A., and Pethig, R. (1977). Dielectric measurements using non-uniform electric field (dielectrophoretic) effects. *J. Phys. E: Sci. Instrum.*, Vol. 10, pp. (190-193)

Popovtzer, R., Neufeld, T., Ron, E.Z., Rishpon, J., Shachman-Diamand, Y. (2006) Electrochemical detection of biological reactions using a novel nano-bio-chip array. *Sensors and Actuators B.* Vol. 199, pp. 664-672.

Price, J.A.R., Burt, J. P.H., and Pethig, R. (1988). Applications of a new optical technique for measuring the dielectrophoretic behaviour of micro-organisms. *Biochim. Biophys. Acta,* Vol. 964, pp. (221-230)

Radke, S.M., and Alocilja, E.C. (2005). A microfabricated biosensor for detecting foodborne bioterrorism agents. *IEEE Sensors Journal*, Vol. 5, pp. (744-750)

Ramos, A., Morgan, H., Green, N.G., and Castellanos, A. (1998). Ac electrokinetics: a review of forces in microelectrode structures. *J. Phys. D: Appl. Phys*., Vol. 31, pp. (2338-2353)

Ramos, A., Morgan, H., Green, N.G., and Castellanos, A. (1999). AC Electric-Field-Induced Fluid Flow in Microelectrodes. *J.Coll. Int. Sci.*, Vol. 217, pp. (420-422)

de la Rica, R., Mendoza, E., Lechuga, L.M., and Matsui, H. (2008). Label-Free Pathogen Detection with Sensor Chips Assembled from Peptide Nanotubes. *Angew. Chem. Int. Ed.*, Vol. 47, pp. (9752-9755)

Sader, J.E., (1998). Frequency response of cantilever beams immersed in viscous fluids with applications to the atomic force microscope. *J. Appl. Phys.*, Vol. 84, No. 1, pp. (64-76)

Sauli, U.S., Panayiotou, M., Schnydrig, S., Jordan, M., and Renaud, P. (2005). Temperature measurements in microfluidic systems: Heat dissipation of negative dielectrophoresis barriers. *Electrophoresis,* Vol. 26, pp. (2239-2246)

Schnelle, T., Müller, T., Fiedler, S., Shirley, S. G., Ludwig, K., Herrmann, A., Fuhr, G., Wagner B., and Zimmermann, U. (1996). Trapping of viruses in high-frequency electric field cages. *Naturwisswnschaften,* Vol. 83, pp. (172-176)

Schultz, Z.D., Stranick, S.J., and Levin, I.W. (2009) Advantages and artifacts of higher order modes in nanoparticle-enhanced backscattering Raman imaging. *Anal. Chem.*, Vol. 81, pp. (9657-9663)

Senkevich, J.J., Mitchell, C.J., Yang, G.-R., Lu, T.-U. (2002) Surface Chemistry of Mercaptan and Growth of Pyridine Short-Chain Alkoxyl Silane Molecule Layers. *Langmuir*. Vol. 18, Iss. 5, pp. (1587-1594)

Sigurdson, M., Wang, D., and Meinhart, C.D. (2005). Electrothermal stirring for heterogeneous immunoassays. *Lab Chip,* Vol. 5, pp. (1366-1373)

Sjöberg, R. G., Morisette, D. T., and Bashir, R. (2005). Impedance Microbiology-on-a-Chip: Microfluidic Bioprocessor for Rapid Detection of Bacterial Metabolism. *J. Microelectromech. Syst.*, Vol. 14, pp. (829-838)

Sohn, L.L., Saleh, O.A., Facer, G.R., Beavis, A.J., Allan, R.S., and Notterman, D.A. (2000). Capacitance cytometry: Measuring biological cells one by one. *Proc Natl Acad Sci,*, Vol. 97, pp. (10687-10690)

Stopar, D., Spruijt, R.B., Wolfs, Cor J.A.M., and Hemminga, M. (2003). Protein-lipid interactions of the bacteriophage M13 majr coat protein. *Biochimica et Biophysica Acta (BBA),* Vol. 1611, Iss. 1-2, pp. (5-15)

Suehiro, J., Yatsunami, R., Hamada, R., and Hara, M. (1999) Quantitative estimation of biological cell concentration suspended in aqueous medium by using dielectrophoretic impedance measurement method. *J. Phys. D: Appl. Phys.*, Vol. 32, pp. (2814-2820)

Suehiro, J., Noutomi, D., Shutou, M., and Hara, M. (2003a). Selective detection of specific bacteria using dielectrophoretic impedance measurement method combined with an antigen–antibody reaction. *Journal of Electrostatics*, Vol. 58, pp. (229-246)

Suehiro, J., Shutou, M., Hatano, T., and Hara, M. (2003b). High sensitive detection of biological cells using dielectrophoretic impedance measurement method combined with electropermeabilization, *Sensors and Actuators B,* Vol. 96, pp. (144-151)

Suehiro, J., Hamada, R., Noutomi, D., Shutou, M., and Hara, M. (2003c). Selective detection of viable bacteria using dielectrophoretic impedance measurement method. *Journal of Electrostatics,* Vol. 57, pp. (157-168)

Suehiro, J., Hatano, T., Shutou, M., and Hara, M. (2005). Improvement of electric pulse shape for electropermeabilization assisted dielectrophoretic impedance measurement for high sensitive bacteria detection. *Sensors and Actuators B,* Vol. 109, pp. (209-215)

Suehiro, J., Ohtsubo, A., Hatano, T., and Hara, M. (2006). Selective detection of bacteria by a dielectrophoretic impedance measurement method using an antibody-immobilized electrode chip. *Sensors and Actuators B,* Vol. 119, pp. (319-326)

Sungmoon, H., Woonam, Y., Park, J. C., and Jung., H. Y. (2009). Dielectrophoretic Separation of Airborne Microbes and Dust Particles Using a Microfluidic Channel for Real-Time Bioaerosol Monitoring. *Environ. Sci. Technol.*, Vol. 43, pp. (5857-5863)

Talary, M.S., and Pethig, R. (1994). Optical technique for measuring the positive and negative dielectrophoretic behaviour of cells and colloidal suspensions. *IEE Proc. Sci. Meas. Technol.*, Vol. 141, pp. (395-399)

Talary, M.S., Burt, J.P.H., Tame, J.A., and Pethig, R. (1996). Electromanipulation and separation of cells using travelling electric fields. *J. Phys. D: Appl. Phys.*, Vol. 29, pp. (2198-2203)

Thommes, J. and Gottschalk, U. (2009). Alternatives to Packed-Bed Chromatography for Antibody Extraction and Purification. *Process Scale Purification of Antibodies*. Eds. Gottschalk, U. pp. (293–308)

Tomkins, M.R., Wood, J.A., and Docoslis, A. (2008). Observations and Analysis of Electrokinetically Driven Particle Trapping in Planar Microelectrode Arrays. *The Canadian*

Journal of Chemical Engineering, Vol. 86, pp. (609-621)
Triangular Electrodes: www.chemeng.queensu.ca/research/publicationmedia/0002.mov
Circular Electrodes: www.chemeng.queensu.ca/research/publicationmedia/0003.mov

Tomkins, M.T., Chow, J., Lai, Y-J., Docoslis, A., (Accepted pending minor revisions, 2011) A coupled cantilever-microelectrode biosensor for enhanced pathogen detection. *Sensors and Actuators*.

Tuukkanen, S., Toppari, J. J.,Kuzyk, A. Hirviniemi, L., Hytönen, V.P. Ihalainen, T. and Törmä, P. (2006). Carbon Nanotubes as Electrodes for Dielectrophoresis of DNA. *Nano Lett.,* Vol. 6, pp. (1339-1343)

Velev, O.D., and Kaler, E.W. (1999). In Situ Assembly of Colloidal Particles into Miniaturized Biosensors, *Langmuir*, Vol. 15, pp. (3693-3698)

Velusamy, V., Arshak, K., Korostynska, O., Oliwa, K., and Adley, C. (2010). An overview of foodborne pathogen detection: In the perspective of biosensors. *Biotechnology Advances,* Vol. 28, pp. (232-254) 0734-9750

Voldman, J., Gray, M.L., Toner, M., Schmidt, M.A. (2002) A microfabrication-based dynamic array cytometer. *Anal. Chem.*, Vol. 74, pp. (3984-3990)

Walti, C. W¨; Germishuizen, W. A., Tosch, P., Kaminski, C. F., and Davies, A. G. (2007). AC electrokinetic manipulation of DNA. *J. Phys. D: Appl. Phys.*, Vol. 40, pp. (114-118)

Wana, Y., Zhanga, D., and Hou, B. (2009). Monitoring microbial populations of sulfate-reducing bacteria using an impedimetric immunosensor based on agglutination assay. *Talanta*, Vol. 80, pp. (218-223)

Wang, T–H., Peng, Y., Zhang, C., Wong, P. K., and Ho, C–M. (2005). Single-Molecule Tracing on a Fluidic Microchip for Quantitative Detection of Low-Abundance Nucleic Acids. *J Am Chem Soc.,* Vol. 127, pp. (5354-2365)

Washizu, M., and Kurosawa, O. (1990). Electrostatic Manipulation of DNA in Microfabricated Structures. *IEEE Transactions on Industry Applications*, Vol. 26, pp. (1165-1172)

Washizu, M., Kurosawa, O., Arai, I., Suzuki, S., and Shimamoto, N. (1995). Applications of electrostatic stretch and-positioning of DNA *IEEE Trans. Ind. Appl.,* Vol. 31, No. 3, pp. (447-456)

Washizu, M., Kimura, Y., Kobayashi, T., Kurosawa, O., Matsumoto, S., and Mamine, T. (2004). Stretching DNA as a template for molecular construction. *AIP Conference Proceedings Series,* Vol. 725, pp. (67-77)

Washizu., M. (2005). Biological applications of electrostatic surface field effects. *Journal of Electrostatics*, Vol. 63, pp. (795-802)

Weigl, B.H., Bardell, R.L., Cabrera, C.R. (2003). Lab-on-a-chip for drug development. *Adv. Drug Delivery Rev.* Vol. 55, pp. (349-377)

Wong, P.K., Chen, C.Y., Wang, T.H., and Ho, C.M. (2004b). Electrokinetic bioprocessor for concentrating cells and molecules. *Anal. Chem.*, Vol. 76, pp. (6908-6914)

Wood, J. A., Zhang, B., Tomkins, M. R., and Docoslis, A. (2007). Numerical investigation of AC electrokinetic virus trapping inside high ionic strength media. *Microfluid Nanofluid,* Vol. 3, pp. (547-560)

Wu, J., Ben, Y., Battigelli, D., and Chang, H–C. (2005a). Long-Range AC Electroosmotic Trapping and Detection of Bioparticles. *Ind. Eng. Chem. Res.*, Vol. 44, pp. (2815-2822)

Wu, J., Ben, Y., and Chang, H.C. (2005b). Particle detection by electrical impedance spectroscopy with asymmetric-polarization AC electroosmotic trapping. *Microfluid Nanofluid,* Vol. 1, pp. (161-167)

Yamamoto, T., Kurosawa, O., Kabata, H., Shimamoto, N., and Washizu, M. (2000). Molecular Surgery of DNA Based on Electrostatic Micromanipulation. *IEEE Transactions on Industry Applications,* Vol. 36, pp. (1010-1017)

Yang, L. (2009). Dielectrophoresis assisted immuno-capture and detection of foodborne pathogenic bacteria in biochips. *Talanta,* Vol. 80, pp. (551-558)

Yang, L., Banada, P.P., Bhunia, A.K., and Bashir, R. (2008). Effects of Dielectrophoresis on Growth, Viability and Immuno-reactivity of *Listeria monocytogenes*. *J Biol Eng* Vol. 2, No. 1, Record (6)

Yang, L., Banada, P.P., Chatni, M.R., Lim, K.S., Bhunia, A.K., Ladischde, M., and Bashir, R. (2006). A multifunctional micro-fluidic system for dielectrophoretic concentration coupled with immuno-capture of low numbers of *Listeria monocytogenes*. *Lab Chip*, Vol. 6, pp. (896-905)

Yang, L. and Bashir, R. (2008). Electrical / electrochemical impedance for the rapid detection of foodborne pathogenic bacteria. *Biotechnology Advances*. Vol. 26, pp. (135-150).

Zheng, X., Silber-Li, Z. (2009) The influence of Saffman lift force on nanoparticle concentration distribution near a wall. *Appl. Phys. Lett.*, Vol. 95, Iss. 12, pp. (124105).

Zhou, R., Wang, P., and Chang, H-C. (2006). Bacteria Capture, concentration and detection by alternating current dielectrophoresis and self-assembly of dispersed single-wall carbon nanotubes. *Electrophoresis,* Vol. 27, pp. (1376-1385)

Appendix A

Numerical Simulation Details

The numerical simulations presented in Chapter 3 consist of one quarter of the microelectrode being investigated while submerged in fluid. A simplified schematic of the full system is presented below. For visualization purposes, each domain is coloured for ease of identification. The numerical simulation can be subdivided into 4 domains. The first two domains model the substrate which consists of a (1) 499.5 μm thick layer of silicon with a (2) 500 nm thick layer of silicon dioxide on top. The third domain is a (3) 200 nm thick gold microelectrode which partially covers the silicon dioxide. The fourth domain represents a (4) 499.8 μm high water droplet with a fixed shape in contact with both the gold microelectrodes and the exposed silicon substrate. A summary of the assumptions, boundary conditions and expressions used are shown in table A1.

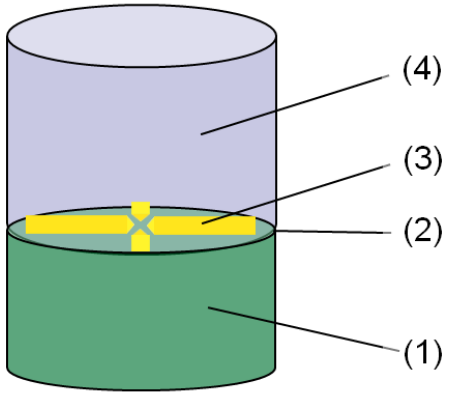

Table A1: Numerical Simulation Details

Domain	Subdomain Expressions
(1), (2), (3), (4)	$\varepsilon \nabla E = 0$ $\nabla \cdot (k_i \nabla T) + \sigma \lvert E \rvert^2 = 0$
(4)	Fluid > $\nabla \cdot \left(-pI + \mu(\nabla \vec{u} + (\nabla \vec{u})^t) \right) + f_e = 0$ Net Forces on Particles > $u_p = u_m + \frac{\vec{F}_{DEP}}{f}$

Domain	Boundary Conditions
(1), (2)	External surfaces have a fixed temperature (T = 293 K)
(3)	Exterior surfaces have no net charge Electrode surfaces have a constant Voltage (V = 1.41 V)
(4)	No slip conditions at the wall (u=0) External surfaces have a fixed temperature (T = 293 K)

Domain	Assumptions
(1), (2), (3), (4)	Steady State ($\frac{\delta T}{\delta t} = 0$) Advection is negligible (Peclet number <1)
(3)	Electrostatic approximation (V ≅ constant)
(4)	Charge density ≅ 0 (Gauss's Law simplifies to $\varepsilon \nabla^2 V \cong 0$) Large κa limit (κa >> 1) and therefore E is independent of the electrical double layer Isotropic (allows for using $\mu \nabla^2 \vec{u} = \mu(\nabla \vec{u} + (\nabla \vec{u})^t)$ in the Navier-Stokes Equation

	Buoyancy is negligible (Grashof number < 1)
	Particle Inertia is negligible (Reynolds number <1)
	Convection is negligible (Prandlt number <1)

Appendix B

Raman Vibrational Modes

A1 - Styrene Vibrational In-Plane and Symmetrical

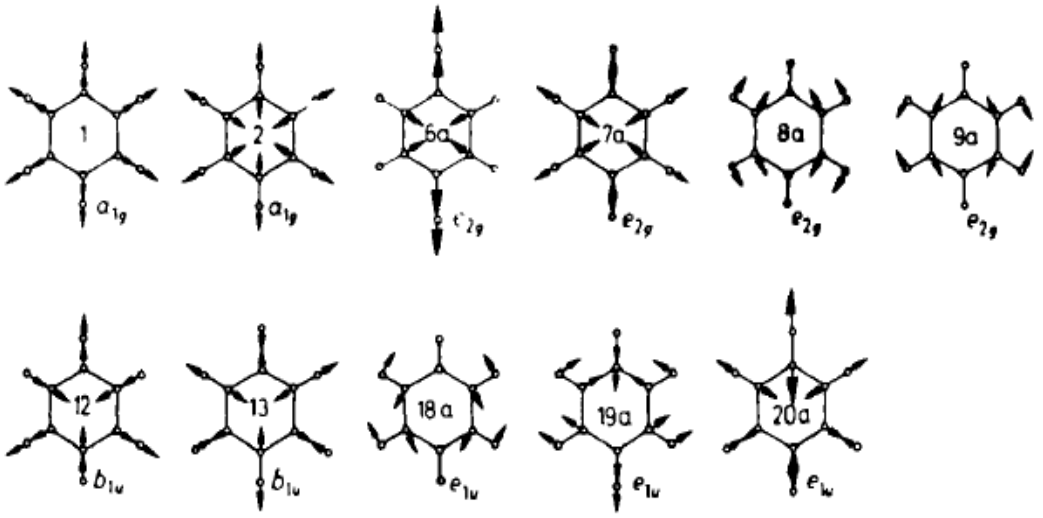

(Jesse et al., 1978)

B2 - Styrene Vibrational In-Plane and Non-Symmetrical

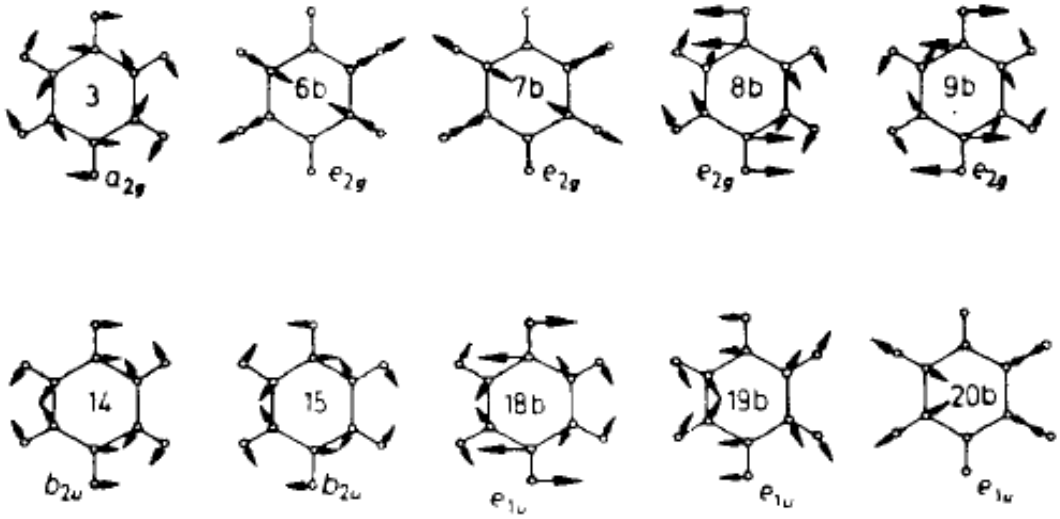

(Jesse *et al.*, 1978)